Doctoral theses at NTNU, 2025:112

Kamaljeet Singh

Nickel–Iron–Copper-Based Oxygen Evolving Anode for Low Temperature Aluminum Electrolysis

Doctoral thesis

NTNU
Norwegian University of Science and Technology
Thesis for the Degree of
Philosophiae Doctor
Faculty of Natural Sciences
Department of Materials Science and Engineering
REYKJAVIK UNIVERSITY
Department of Engineering

NTNU
Norwegian University of
Science and Technology

Kamaljeet Singh

Nickel–Iron–Copper-Based Oxygen Evolving Anode for Low Temperature Aluminum Electrolysis

Thesis for the Degree of Philosophiae Doctor

Trondheim, June 2025

Norwegian University of Science and Technology
Faculty of Natural Sciences
Department of Materials Science and Engineering

Reykjavik University
Department of Engineering

NTNU
Norwegian University of
Science and Technology

NTNU
Norwegian University of Science and Technology

Thesis for the Degree of Philosophiae Doctor

Faculty of Natural Sciences
Department of Materials Science and Engineering

REYKJAVIK UNIVERSITY
Department of Engineering

ORCID iD: 0000-0003-3557-3944

NTNU:
ISBN 978-82-326-9084-8 (printed ver.)
ISBN 978-82-326-9083-1 (electronic ver.)
ISSN 1503-8181 (printed ver.)
ISSN 2703-8084 (online ver.)

Reykjavik University:
ISBN 978-9935-539-70-0 (printed ver.)
ISBN 978-9935-539-71-7 (electronic ver.)

Doctoral theses at NTNU, 2025:112

Printed by NTNU Grafisk senter

Preface

This thesis is the result of my research conducted as part of a double degree PhD program at Reykjavik University, Iceland, and NTNU Trondheim, Norway, from January 2021 to November 2024. The work was carried out in close collaboration with Taeknisetur IceTec and Arctus Aluminium, both based in Iceland. The project was generously funded by the Icelandic Centre for Research (Rannis) under the PhD project grant number 207242051.

The thesis is structured as a collection of three papers, presented in Chapters 3 to 5. Two papers (Chapters 3 and 4) have been published, while the third (Chapter 5) is intended for future publication. My main supervisor, Gudrun Saevarsdottir (Professor, Reykjavik University and NTNU), and co-supervisors, Gudmundur Gunnarsson (Group Leader, Taeknisetur IceTec) and Geir Martin Haarberg (Professor, NTNU), along with the co-authors listed for each paper, contributed to the corresponding discussions in Chapters 3 to 5.

The majority of the work was conducted at the joint electrolysis laboratory of Reykjavik University and Taeknisetur IceTec, located at Taeknisetur IceTec. Additional electrochemical measurements were performed at the Electrolysis Group, Department of Materials Science and Engineering, NTNU Trondheim.

All experimental work presented in this thesis was conducted by the author, with the following exceptions: Inductively Coupled Plasma (ICP)-Optical Emission Spectroscopy (OES), and Spark-OES analyses were performed at Trimet Aluminium, Germany (Chapter 3, and Chapter 5). Two anode alloy compositions were produced by Thomas Luke Jamieson, a PhD student at Saarland University, Saarbrücken, Germany (Chapter 4). Additionally, the casting of all anode alloy compositions and dry oxidation experiments using a Thermogravimetric Analyzer (TGA) were also conducted by Thomas Luke Jamieson (Chapter 5, Fig. 3, Table 1). ICP-Mass Spectroscopy (MS) analysis was performed by Chemist Joe Seattle Jephson at Hafrannsoknastofnun, Iceland (Chapter 5).

All data processing obtained by experimental work was performed by the author, except for MATLAB simulations, which were performed by Postdoctoral Fellow Abdul Rahman Mallah at Reykjavik University (Chapter 4, Fig. 3).

Kamaljeet Singh
Reykjavik
November 30, 2024

This page is intentionally left blank.

Acknowledgements

First and foremost, I extend my gratitude to my main supervisor, Professor Gudrun Saevarsdottir, for her support, helpful discussions, and genuine interest in my work. Her guidance has been invaluable throughout this journey.

I wish to express my appreciation to my co-supervisor, Professor Geir Martin Haarberg, for his valuable guidance and for making conference trips both productive and enjoyable. I greatly benefited from his course lectures and discussions.

I am sincerely thankful to my co-supervisor, Dr. Gudmundur Gunnarsson, for his exceptional mentorship, open office policy, and practical guidance. His support has been instrumental in shaping this research.

I am grateful to Jon Hjaltalin Magnusson of Arctus Aluminium for his expert advice and active interest in this work.

I am thankful to all my colleagues and friends at Reykjavik University, NTNU Trondheim, and Taeknisetur IceTec. In particular, I would like to mention Vijay Chauhan for introducing me to this exciting opportunity, Daniel Thor Gunnarsson for our coffee break discussions, Sai Krishna Padamata, Abdul Rahman Mallah, Shalini Chakraborty, Dagur Ingi Olafsson, Gudbjorg Hronn Oskarsdottir, Yukihiro Takahashi, Bo Qin, Anita Storsve, and Thordur Magnusson for their companionship and support.

A special thanks to my friend and fellow PhD student, Hakon Valur Haraldsson, whose engaging conversations, though often unrelated to research, provided much needed perspective beyond academia.

My appreciation also extends to the staff at SINTEF Trondheim, especially Henrik Gudbrandsen for his supportive attitude and Karen Osen for her assistance with lab equipment. I am further grateful for the workshop support provided by Aksel Alstad, Øystein Gjervan Hagemo, and Gisli Freyr Thorsteinsson.

I would like to thank the Icelandic Centre for Research for the financial support.

Finally, I wish to express my gratitude to my wife, Priyanka, for her love, support and care during these years. Her understanding made it easier for me to dedicate myself to time consuming experiments and long working hours. I also extend my thanks to little Reyansh, whose smile upon my return home brought immense joy.

This work is dedicated to my family and friends,
whose support has been a foundation of my journey.

Abstract

The Hall–Héroult process is, currently, the only industrial method for primary aluminum production. However, the process suffers from many inefficiencies, mainly because the carbon anodes are continuously consumed during electrolysis, producing greenhouse gas emissions—primarily CO_2 and, intermittently, perfluorocarbons. Another inefficiency in the process is its high energy demand, essentially caused by a significant ohmic voltage drop resulting from the large anode-cathode distance created by the molten aluminum pool, and a high anodic overpotential due to the slow kinetics of the anodic process. Therefore, to eliminate greenhouse gas emissions and improve energy utilization in aluminum electrolysis a non-consumable, cost effective, and efficient oxygen evolving anode (OEA) is essential.

Recent research has shown that the use of nickel–iron–copper-based alloys for the OEA offers promising performance in low temperature electrolytes. This performance advantage is attributed to their ability to form a protective nickel-ferrite ($NiFe_2O_4$) oxide scale during anodic reactions, coupled with their reduced wear rates under these operating conditions. Unfortunately, systematic studies on the effects of alloy composition and low temperature electrolyte composition on the formation and stability of the protective scale are lacking. The present work explored the use of various earth-abundant Ni–Fe–Cu-based alloys for the OEA in a range of low temperature $KF\text{-}NaF\text{-}AlF_3\text{-}Al_2O_{3(sat.)}$-based electrolyte compositions for aluminum electrolysis at 800 ^{0}C. Additionally, a TiB_2 wettable aluminum cathode and a vertical electrode configuration were employed to develop a compact and energy efficient cell.

To identify the optimal compositions and conditions for aluminum electrolysis in a 40 A laboratory cell, two electrolyte compositions, K-rich and Na-rich, were investigated using Ni–Fe–Cu alloys as anodes. It was found that the K-rich electrolyte composition in combination with $Ni_{42}\text{-}Fe_{38}\text{-}Cu_{20}$ anode offered a low anode wear rate and stable electrolysis. This performance was attributed to the better alumina solubility of the electrolyte and the formation of a dense and protective $NiFe_2O_4$ oxide on the anode surface. The oxidation treatment of the $Ni_{42}\text{-}Fe_{38}\text{-}Cu_{20}$ alloy, to pre-form an oxide scale, demonstrated its ability to form a multi-layered oxide scale of CuO, Fe_2O_3 and protective $NiFe_2O_4$. This indicated the effectiveness of the treatment in developing a protective oxide scale ex-situ, which was found satisfactory for meeting the requirements of the OEA.

The use of the OEA leads to higher energy demands compared to the Hall–Héroult process with carbon anodes, primarily due to the increased reaction voltage. Therefore, to assess the energy efficiency in terms of overpotential on OEA, steady state anodic polarization curves were obtained on platinum and a series of Ni–Fe–Cu-based alloys. The polarization curve on the platinum anode exhibited two linear regions, showing good consistency with the proposed theoretical mechanism of oxygen evolution reaction. The polarization curve on alloys, both in oxidized and untreated conditions, however, exhibited a single Tafel region. At a normal current density of 0.8 Acm^{-2}, the oxidized anodes $Ni_{42}\text{-}Fe_{38}\text{-}Cu_{20}$ and $Ni_{48}\text{-}Fe_{47}\text{-}Cu_5$ showed lower overpotentials after electrolysis compared to untreated anodes

of same composition, respectively. This resulted from the fact that oxidized anodes exhibited better electrocatalytic activity with lower Tafel slopes, mainly due to the pre-formed conductive oxide scale through oxidation treatment.

To determine the optimal Ni/Fe ratio in the alloy, a series of $Ni_{90-x}Fe_xCu_{10}$ alloys, Ni/Fe ratios (wt.%) varying between 0.5 and 8, was tested for OEA. The study optimized the OEA alloy composition through a three-step approach: conducting thermodynamic analysis, evaluating oxidation kinetics, and performing long-duration electrolysis tests in fluoride melts. These combined investigations were aimed at elucidating the mechanism governing the formation of a stable oxide scale. The results showed that decreasing the Ni/Fe ratio from 8 to 0.5 positively influenced anode performance. The mechanism of oxide scale growth in Ni-rich alloys, Ni/Fe ratio of 3.5 to 8, revealed the formation of NiO as the primary oxide, followed by its conversion to an insulating $NiAl_2O_4$, resulting in severe corrosion. In contrast, Fe-rich alloys with an Ni/Fe ratio of 0.5 to 0.8 exhibited a dense and well-adherent oxide scale with a dual-layered structure. This structure consisted of an outer stoichiometric $NiFe_2O_4$ layer at the oxide/electrolyte interface and an inner, non-stoichiometric $Ni_xFe_{3-x}O_4$ layers layer enriched in Fe at the oxide/alloy interface. Notably, an optimized Ni/Fe ratio found between 0.5 and 0.8, as in the $Ni_{40}Fe_{50}Cu_{10}$ alloy, resulted in a stable anode potential and high metal purity during 24 h of electrolysis. This performance was ascribed to the formation of a kinetically slow growing and stable oxide scale, optimized by the Ni/Fe ratio to produce the protective $NiFe_2O_4$, which improved corrosion resistance and maintained electrochemical stability.

Table of contents

Preface iii

Acknowledgements v

Abstract vii

Table of contents ix

Nomenclature xi

Chapter 1. Introduction **1**

1.1 Background and motivation 1

1.2 Aim of work 4

1.3 Structure of the thesis 5

References 5

Chapter 2. Literature review **7**

2.1 Historical overview 7

2.2 Ni–Fe–Cu-based anode 9

2.3 TiB_2 ceramic cathode 11

2.4 Low temperature electrolyte 11

References 12

Chapter 3. Performance Evaluation of Low-Temperature KF-NaF-AlF_3 Electrolytes for Aluminum Electrolysis Using Vertical Inert Cu-Ni-Fe Alloy Anodes **17**

Chapter 4. Overpotential on Oxygen Evolving Platinum and Ni–Fe–Cu Anode for Low Temperature Molten Fluoride Electrolytes **43**

Chapter 5. Ni–Fe-based Alloy as Oxygen Evolving Anode for Sustainable Aluminum Production **63**

Chapter 6. Conclusions **95**

6.1 Performance evaluation of low temperature electrolyte 95

6.2 Overpotential on oxygen evolving Pt and Ni–Fe–Cu anodes 96

6.3 Influence of Ni/Fe ratio on oxide growth mechanism 97

Chapter 7. Future work **99**

This page is intentionally left blank.

Nomenclature

Roman Letters

a_x	Activity of species x	—
A	Area of anode	cm^2
b	Tafel slope	V dec^{-1}
CR	Cryolite ratio	mol mol^{-1}
E	Voltage	V
$\mathrm{E}^{\mathrm{rev}}$	Reversible voltage	V
F	Faraday's constant	C mol^{-1}
G	Gibbs free energy	J
I, i	Current	A
I	Current density	A cm^{-2}
k_c	Cubic rate constant	g^3 cm^{-6} s^{-1}
KR	Potassium ratio	mol mol^{-1}
n, z	Number of total electrons transfer	—
R	Gas constant	J K^{-1} mol^{-1}
r	Cryolite ratio	mol mol^{-1}
R_a	Surface roughness	µm
T	Absolute temperature	K
T	Temperature	^{o}C
t	Time	h

Greek Letters

α	Symmetry coefficient	—
γ	Crystalline structure	—
η	Anodic overpotential	V
ρ	Density	g cm^{-3}
θ	Surface coverage	—

Abbreviations

AC	Alternating current
ACD	Anode-cathode distance
CO$_2$e	Carbon dioxide equivalent
EDS	Energy dispersive spectroscopy
fcc	Face-centered cubic crystalline structure
GHG	Greenhouse gas
H–H	Hall–Héroult process
IAT	Inert anode technology
ICP–OES	Inductively coupled plasma–optical emission spectrometry
ICP–MS	Inductively coupled plasma–mass spectrometry

LSV	Linear sweep voltammetry
OEA	Oxygen evolving anode
OER	Oxygen evolution reaction
PFC	Perfluorocarbon
ppm	Parts per million
RDS	Rate determining step
SEM	Scanning electron microscopy
TGA	Thermogravimetric analyzer
XRD	X–ray diffraction

Chapter 1

Introduction

1.1 Background and motivation

Aluminum is an essential material in modern engineering. In 2023, global production reached 70 million tonnes, driven by its low weight, high corrosion resistance, and full recyclability, making it crucial in the construction, automotive, and packaging industries[1]. However, the aluminum industry remains highly energy- and emission-intensive, with greenhouse gas (GHG) emissions exceeding 1 billion tonnes of carbon dioxide equivalent (CO_2e) in 2023, significantly contributing to climate change.

Although total GHG emissions can be reduced from the current average of ~15 kg CO_2e per kg of aluminum to as low as ~2 kg CO_2e per kg using renewable energy, unfortunately, over 60% of global aluminum production still relies on non-renewable energy due to the limited availability of clean energy sources[1]. While this transition to renewable energy sources in near future would significantly lower indirect (electricity-related) emissions, achieving net-zero emissions by 2050 also requires tackling direct (process-related) emissions from the conventional Hall–Héroult process—a critical challenge for the aluminum industry.

Currently, primary aluminum production continues to depend on the Hall–Héroult process, a method invented in 1886 that has remained fundamentally unchanged ever since (Fig. 1)[2]. This process involves the electrochemical dissociation of alumina (Al_2O_3) in a molten cryolite-based electrolyte bath at around 966 ^{o}C, primarily consisting of Na_3AlF_6, using a consumable carbon anode and liquid aluminum as the cathode, according to Eq. (1)[2].

$$\frac{1}{2}\mathrm{Al_2O_{3(diss.)}} + \frac{3}{4}\mathrm{C_{(s)}} \rightarrow \mathrm{Al_{(l)}} + \frac{3}{4}\mathrm{CO_{2(g)}};\ \mathrm{E^{rev}\,at\,966^{0}C} = 1.19\mathrm{V} \qquad (1)$$

Over time, the Hall–Héroult process has undergone continuous improvements in terms of productivity, energy efficiency and environmental impact. However, the use of consumable carbon anodes in the process results in substantial GHG emissions, direct process emission of CO_2, and intermittent perfluorocarbon emissions (CF_4, and C_2F_6) during 'anode effect', about 1.5–2 kg CO_2e per kg of aluminum produced[2,3].

In addition, the Hall–Héroult process requires a significant amount of electrical energy, ~12–15 kWh per kg of aluminum. This high electrical energy demand is largely attributed to a substantial ohmic voltage drop caused by the large anode-cathode distance imposed by the molten aluminum pool, as well as a high anodic overpotential resulting from the slow kinetics of the anodic process[4].

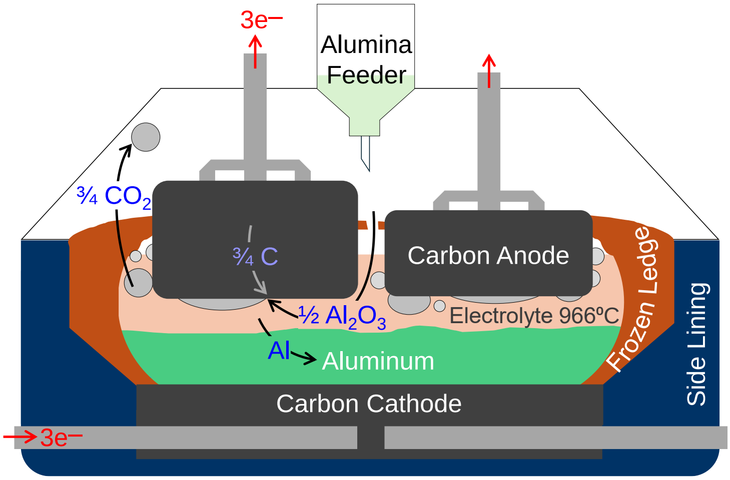

Fig. 1. Simplified schematic illustrating the conventional Hall–Héroult process, featuring a horizontally configured consumable carbon anode that emits CO_2 and a carbon cathode covered by molten aluminum.

To mitigate direct process related emissions from aluminum electrolysis, the development of a non-consumable, cost effective and efficient oxygen evolving anode (OEA) is crucial, offering benefits in environmental impact reduction, energy efficiency, and economic feasibility (Fig. 2)[3,5,6]. The term OEA is commonly used in the literature interchangeably with inert anode, non-consuming anode, and dimensionally stable anode. However, this study prefers the term OEA while other terms are used when appropriate. By using an OEA, the anode reaction would replace CO_2 emissions with the environmentally favorable O_2, as depicted in Eq. (2):

$$\frac{1}{2}\mathrm{Al_2O_{3(diss.)}} \rightarrow \mathrm{Al_{(l)}} + \frac{3}{4}\mathrm{O_{2(g)}};\ \mathrm{E^{rev}\ at\ 800^0C} = 2.31\ \mathrm{V} \qquad (2)$$

Notably, in this alternative technology, the absence of energy contributions from carbon oxidation reactions, combined with an increase in Gibbs free energy due to the low temperature electrolyte bath, raises the reversible voltage ($\mathrm{E^{rev}}$) of the cell by 1.12 V in Eq. (2) compared to Eq. (1)[7]. Nevertheless, cell designs featuring a vertical electrode configuration, minimized interpolar distance (< 2 cm), lower overpotentials, and compact cell could help counterbalance the higher reversible voltage[8–12]. These design enhancements aim to reduce energy losses and optimize the electrochemical efficiency of the electrolysis cell. The key characteristics required for an OEA material are[6]:

- excellent electrochemical stability and low corrosion rate (< 5 $\mathrm{mmyear^{-1}}$),
- high mechanical strength and durability, and
- excellent thermal and electrical conductivity.

Researchers have extensively investigated metals, alloys, ceramics, and mixtures of alloys and ceramics known as cermets, as potential materials for OEAs. Notable examples of these materials include pure metals such as copper and platinum, alloys like nickel-iron-copper, tin-oxide ceramics, and nickel-ferrite cermets[5,6,13]. Despite showing promising properties, these anode materials have encountered challenges such as high corrosion rates and increased level of impurities in the produced aluminum. As a result, after more than a century of research, no material has yet met the long-term viability requirements for commercial application as an inert anode in aluminum production. Meanwhile, titanium-diboride (TiB_2) ceramic as a wettable aluminum cathode is considered as a good inert candidate material[6,13–17].

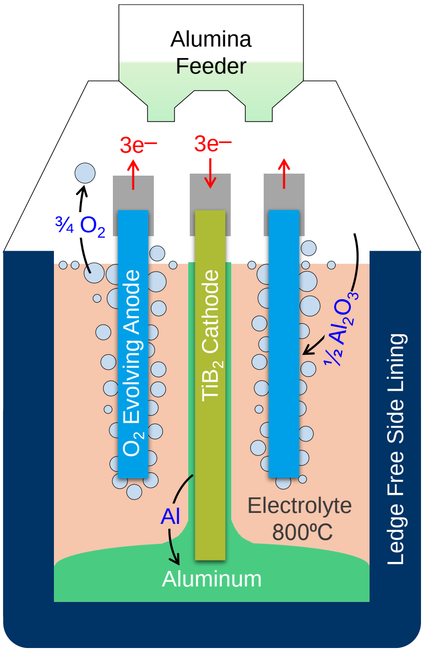

Fig. 2. Schematic of an aluminum electrolysis cell based on the proposed OEA technology, featuring a vertically configured metallic anode that evolves O_2 and a TiB_2 ceramic cathode wetted by molten aluminum.

Building on over a decade of collaborative work with Arctus Aluminium and Taeknisetur IceTec in Iceland, recent efforts have focused on advancing OEA technology, focusing on the following key strategies[12]:

i. Low temperature electrolytes: Employing low temperature electrolytes, with a liquidus range of 700—775 ^{o}C, to reduce high temperature corrosion.
ii. Single-phase Ni–Fe–Cu alloy anode: Using homogenized, single-phase Ni–Fe–Cu-based alloys for OEAs to avoid phase instability during electrolysis at 800 ^{o}C.
iii. Oxidation treatment of anode alloy: Subjecting the anode alloy to high temperature air oxidation to pre-form a dense, protective and desirable oxide scale.

iv. Fine-grained TiB_2 cathode: Utilizing a dense, fine-grained TiB_2 structure to minimize aluminum penetration into the wettable cathode.
v. Keeping electrodes polarized: Maintaining the electrode polarization at about 2.2 V upon introduction into the fluoride bath or when idle, to prevent chemical dissolution.
vi. Cathodically polarized aluminum: Ensuring polarization of the produced liquid aluminum through contact with the cathode for improved current efficiency and anode performance (Fig. 2).
vii. Vertical electrodes cell design: Adopting a vertical cell configuration with flat anodes and cathodes, about 10 mm thick, to enhance energy efficiency through a reduced interpolar distance down to 2 cm.

While the past few years have seen growing research on the use of Ni–Fe–Cu-based alloys for the OEAs in low temperature electrolytes, however, studies specifically addressing this within the context of the newly outlined approach remains relatively limited[5,6]. Furthermore, the systematic effects of alloy and electrolyte compositions on the formation and stability of the oxide scale are not yet well understood.

1.2 Aim of work

The work presented in this thesis focuses on primary aluminum production using KF-NaF-AlF_3-$Al_2O_{3(sat.)}$-based low temperature electrolyte compositions at 800 ^oC, employing various single-phase compositions of Ni–Fe–Cu alloys for the anode and TiB_2 for the cathode. This research is directed toward achieving the following three main goals:

i. To evaluate the optimal compositions of electrolytes and anode alloys.
ii. To study the anodic overpotential to assess energy efficiency.
iii. To understand the influence of Ni/Fe ratio on oxide growth mechanisms in alloys.

For the first goal, two compositions, single-phase and homogenized, of Ni–Fe–Cu alloys, produced through casting, were investigated in a 40 A electrolysis cell featuring vertical electrodes configuration. Two variations of KF-NaF-AlF_3-based electrolyte were investigated. The impact of anode alloys, electrolyte compositions, and electrolysis conditions on the cell voltage, wear rate of alloy, and purity of the produced aluminum were systematically evaluated.

For the second goal, the anodic overpotentials on oxygen evolving platinum and three compositions of Ni–Fe–Cu alloys were evaluated. A mechanism scheme was proposed, and kinetic equations were derived to simulate theoretical Tafel curves. Experimental Tafel curves were analyzed and compared with theoretical curves to elucidate the kinetics and mechanism of the oxygen evolution reaction.

For the third goal, a series of $Ni_{90-x}Fe_xCu_{10}$ alloys, with x (in wt.%) ranging from 10 to 60 in increments of 10, were evaluated for aluminum production to determine the optimal Ni/Fe ratio. The suitability of OEA alloys was assessed through a combination of thermodynamic analysis, oxidation kinetics, and extended electrolysis performance in fluoride melts, with the aim of elucidating the mechanism of stable oxide scale formation. Furthermore, this study demonstrated a reliable and economical method for screening alloys for OEA applications.

1.3 Structure of the thesis

Chapter 1 provides a brief introduction to the thesis, including the motivation for the work and the three main goals.

Chapter 2 presents a literature review on advancements in inert anode technology.

Chapters 3 to 5 present the research outcomes that address the three main goals mentioned above. The first article in Chapter 3, titled ''Performance Evaluation of Low-Temperature KF-NaF-AlF_3 Electrolytes for Aluminum Electrolysis Using Vertical Inert Cu-Ni-Fe Alloy Anodes,'' was published in The Electrochemical Society (ECS) journal[18]. The second article in Chapter 4, titled ''Overpotential on Oxygen Evolving Platinum and Ni–Fe–Cu Anode for Low Temperature Molten Fluoride Electrolytes,'' was published in the Journal of The Minerals, Metals & Materials Society (TMS)[19]. The third article, titled ''Ni–Fe-based Alloy as Oxygen Evolving Anode for Sustainable Aluminum Production,'' is intended for submission to a relevant journal.

Chapter 6 presents the overall conclusions drawn from Chapters 3 to 5.

Chapter 7 offers suggestions and ideas for future work.

References

[1] Primary Aluminium Production - International Aluminium Institute, 2023 database, accessed on October 9, 2024, IAI, UK. (n.d.). https://international-aluminium.org/.

[2] J. Thonstad, P. Fellner, G.M. Haarberg, J. Hives, H. Kvande, A. Sterten, Aluminium Electrolysis: Fundamentals of the Hall-Héroult Process, Beuth Verlag GmbH, 2011.

[3] G. Saevarsdottir, H. Kvande, B.J. Welch, Aluminum Production in the Times of Climate Change: The Global Challenge to Reduce the Carbon Footprint and Prevent Carbon Leakage, JOM. 72 (2020) 1422–1422.

[4] K. Grjotheim, H. Kvande, Introduction to aluminium electrolysis: Understanding the Hall-Hérloult process, Aluminium-Verlag, Düsseldorf, 1993.

[5] S.K. Padamata, K. Singh, G.M. Haarberg, G. Saevarsdottir, Review—Primary Production of Aluminium with Oxygen Evolving Anodes, J. Electrochem. Soc. 170 (2023) 073501.

[6] I. Galasiu, R. Galasiu, J. Thonstad, Inert Anodes for Aluminium Electrolysis, Beuth Verlag GmbH, 2011.

[7] A. Roine, HSC Chemistry Software, Version 9.9.2.3, Metso Outotec, Pori, Finland, (2017). www.mogroup.com/hsc.

[8] T.R. Beck, Production of Aluminum with Low Temperature Fluoride Melts, in: G. Bearne, M. Dupuis, G. Tarcy (Eds.), Essential Readings in Light Metals: Volume 2

Aluminum Reduction Technology, Springer International Publishing, Cham, 2016: pp. 89–95.

[9] T.R. Beck, A Non-Consumable Metal Anode for Production of Aluminum with Low-Temperature Fluoride Melts, Essential Readings in Light Metals: Volume 4 Electrode Technology for Aluminum Production. 4 (2016) 1104–1109.

[10] T.R. Beck, C.M. Macrae, N.C. Wilson, Metal Anode Performance in Low-Temperature Electrolytes for Aluminum Production, Metall Mater Trans B. 42 (2011) 807–813.

[11] T.R. Beck, A New Energy-Efficient and Environmentally Friendly Process to Produce Aluminum, JOM. 65 (2013) 267–271.

[12] G. Gunnarsson, G. Óskarsdóttir, S. Frostason, J.H. Magnússon, Aluminum Electrolysis with Multiple Vertical Non-consumable Electrodes in a Low Temperature Electrolyte, Light Metals 2019. (2019) 803–810.

[13] S.K. Padamata, K. Singh, G.M. Haarberg, G. Saevarsdottir, Wettable TiB2 Cathode for Aluminum Electrolysis: A Review, Journal of Sustainable Metallurgy. 8 (2022).

[14] D.A. Weirauch Jr, W.J. Krafick, G. Ackart, P.D. Ownby, The wettability of titanium diboride by molten aluminum drops, Journal of Materials Science. 40 (2005) 2301–2306.

[15] R.G. Munro, Material Properties of Titanium Diboride, J Res Natl Inst Stand Technol. 105 (2000) 709–720.

[16] E. Kubiňáková, M. Benköová, P. Veteška, Ľ. Bača, J. Híveš, Surface characterisation and wettability of titanium diboride by aluminium at low temperature, Advances in Applied Ceramics. 119 (2020) 22–28.

[17] Y.-H. Koh, S.-Y. Lee, H.-E. Kim, Oxidation Behavior of Titanium Boride at Elevated Temperatures, Journal of the American Ceramic Society. 84 (2001) 239–241.

[18] K. Singh, G. Gunnarsson, J.H. Magnusson, G.M. Haarberg, G. Saevarsdottir, Performance Evaluation of Low-Temperature KF-NaF-AlF3 Electrolytes for Aluminum Electrolysis Using Vertical Inert Cu–Ni–Fe Alloy Anodes, Journal of The Electrochemical Society. 170 (2023) 113507.

[19] K. Singh, G.M. Haarberg, A.R. Mallah, G. Gunnarsson, T.L. Jamieson, I. Gallino, G. Saevarsdottir, Overpotential on Oxygen-Evolving Platinum and Ni-Fe-Cu Anode for Low-Temperature Molten Fluoride Electrolytes, JOM. 76 (2024) 3284–3293.

Chapter 2

Literature review

2.1 Historical overview

Early developments

Developing an oxygen evolving inert anode is a big step forward for primary aluminum production, aiming to solve the environmental problems that come with using carbon anodes in the conventional Hall–Héroult process. Despite the promise, actually making inert anodes to work effectively has been an ongoing struggle for researchers for the past 135 years[1]. The concept was first explored following the invention of the Hall–Héroult process in 1886 by one of its co-inventor, Charles Hall, who went on to file the first patent for an inert anode in 1889[2]. In this patent, he described a metallic anode made of copper[2]. However, the copper-based anode was severely corroded by the oxygen gas generated at the anode, resulting in copper flakes, which prevented the formation of a dense and coherent oxide layer. Ultimately, he did not succeed in implementing the copper-based inert anode and eventually gave up in 1912.

Belyaev and Studentsov, in 1935, were the first to suggest using oxides (SnO_2, NiO, Fe_3O_4, and Co_3O_4) as inert anode materials after examining various metals, including Cu, Ni, Fe, and Ag[3–5]. Their work concluded that none of these metals could be used as anodes because of their tendency to form non-coherent oxides, and in particular, silver tended to melt. Regarding oxides, they found that all of them exhibited low electrical conductivity, and the aluminum produced was highly contaminated. This prompted them to test mixed oxides, such as SnO_2-Fe_2O_3, NiO-Fe_2O_3, and ZnO-Fe_2O_3, which showed better conductivity and lower corrosion rates compared to single oxides. However, these mixed oxides exhibited poor mechanical strength and corrosion, resulting in poor metal quality.

The use of precious metals like platinum as inert anodes was suggested by several authors[3,6,7]. It was found that platinum could function as an inert anode but would corrode rapidly in alumina depleted melts[6]. Thonstad demonstrated that a platinum anode showed no observable signs of corrosion in an alumina saturated bath at current densities up to 4 Acm^{-2}[7]. Although platinum has potential as an inert anode material, its high cost makes it impractical for use in commercial aluminum production.

Tin oxide (SnO_2) has received considerable attention as a potential material for inert anodes due to its low solubility and enhanced conductivity when combined with doping agents. Swiss Aluminium Company investigated SnO_2-doped anodes, particularly with a composition of 2% Sb_2O_3 and 1% CuO, leading to several patents and studies[8–12].

However, two major issues were encountered with the use of SnO_2 as an inert anode. First, tin contamination in aluminum became a concern, as levels beyond 10 ppm in primary metal could lead to the formation of low-melting Sn-Al alloys, which is intolerable. Second, SnO_2 showed a high corrosion rate in bath depleted in alumina. To address this, it was proposed to use an alumina-saturated bath to limit corrosion, but practical challenges like unavoidable sludge formation made this approach difficult. Many authors investigated SnO_2 material for inert anode but could not commercialize[10–14].

Recent progress

Research efforts gained new momentum during the 1980s, largely due to major developments made by Alcoa, T.R. Beck, and the de Nora Group[15–20]. In 1986, Alcoa patented a nickel-oxide and nickel-ferrite (NiO-$NiFe_2O_4$) ceramic phase combined with a metal phase of nickel and copper, commonly known as cermet anodes[15]. Their research concluded that the NiO-$NiFe_2O_4$ ceramic phase with nickel as the metal phase had excellent electrical conductivity but ultimately failed due to selective corrosion of the metal phase[21–24]. To address this, Alcoa proposed replacing nickel with copper, which was found to improve the corrosion resistance of the cermet anode. This work was subsequently evaluated at a pilot cell at Battelle Pacific Northwest Laboratory in the USA, but they were unable to achieve the same quality of metal that Alcoa had achieved, and the project was ultimately terminated[25].

In 1984, Beck and Brooks patented a slurry cell design with a horizontal electrode configuration, where alumina particles were suspended in the electrolyte[16]. Expanding on this concept, Beck and Brooks filed a new patent in 1988, introducing for the first time a vertical electrode configuration for the anode and cathode[17]. Initial laboratory tests were conducted in a slurry cell with a horizontal anode positioned at the bottom of the cell, while a TiB_2 cathode was suspended above[26,27]. The oxygen gas generated at the anode caused agitation in the electrolyte, which helped keep the alumina particles in suspension. Beck proposed using a metallic anode made from a Cu-Ni-Fe alloy and a low temperature eutectic NaF-AlF_3 electrolyte with a high AlF_3 content[26]. Various alloy compositions as anode were tested, with Cu_{40}-Ni_{30}-Fe_{30} (wt.%) being the most extensively evaluated[26,28]. The alloy demonstrated the ability to form a coherent oxide layer on its surface under the condition of using a low temperature electrolyte bath while maintaining alumina saturation. However, the slurry cell resulted in low current efficiency and poor metal quality due to contact between the produced aluminum and the bottom placed anode, which halted further development. Furthermore, from 1998 to 2005, efforts shifted to a cell with multiple vertical electrode configuration, which was evaluated in a pilot cell at Northwest Aluminum Company in the USA[28–33]. The results were encouraging, with current efficiency and aluminum purity exceeding 80% and 99.5%, respectively. It was later suggested to use single-phase homogenized Cu-Ni-Fe alloys, as double-phase alloys suffered from severe corrosion due to a tunneling corrosion mechanism[32,33]. Unfortunately, due to the financial crisis at Northwest Aluminum Company in 2003, the research facility was shut down, halting further development work.

In 2000, Alcoa announced the development of a new inert anode cell technology and projected it would reach commercial viability within three years[34]. However, by 2003, they reported technical challenges related to anode longevity, and commercialization did not take place as anticipated[1].

In 2005, Moltech Invent, under the de Nora Oxygen Evolving Anodes project, patented a –-Al base alloy with a Co-Ni-oxide coating[20]. These anodes were tested at a pilot scale with currents ranging from 100 to 300 A for up to 60 days, and the results demonstrated a low wear rate[35–37]. However, despite these promising results, the Moltech's inert anode project never transitioned to commercial implementation.

In 2018, even with setbacks in the early 2000s, Alcoa continued its work on developing inert anode technology, leading to the formation of Elysis— a joint venture with Rio Tinto, aimed at commercializing this technology[38]. The patents filed by Elysis describe the use of a vertical electrode configuration[39]. The cermet anodes consist of a Ni–Fe–Cu metallic phase and a nickel-ferrite oxide phase, with minor additions of other alloying elements[40]. Recently, on June 28, 2024, Elysis announced that Rio Tinto had been granted the first inert anode smelter technology license for a 100 kA demonstration plant, which is expected to be operational by 2027[38].

Advancing from the foundation laid by T.R. Beck[29,41], Arctus Aluminium in Iceland has continued developing inert anode technology since 2008, focusing on low temperature electrolytic cell with vertical electrodes. Initial research (2009–2010) was conducted in partnership with Vattenfall Sweden, and in 2015, a continuous collaboration began with Taeknisetur IceTec in Iceland. Over the last decade, various single-phase Ni–Fe–Cu alloy compositions have been tested as anodes in a low temperature KF-NaF-AlF_3-based electrolyte compositions with excess of AlF_3[42–46]. Some of these alloys have shown remarkable stability during electrolysis and produced aluminum with purity reaching 99.9 wt.%. These tests have been conducted in laboratory scale cells ranging from 1 to 700 A capacity, with durations spanning from 6 h to over 100 h. Following these research advancements, a 10 kA pilot cell has been under construction since 2022 in collaboration with the industrial partner Trimet Aluminium in Germany, and it became operational in November 2024[47].

It is noteworthy that inert anode technology is also being pursued in other parts of the world, such as China (Chinalco) and Russia (Rusal)[48]. However, due to the closed nature of research, limited details about their inert anode material and cell technology are available in the open literature.

2.2 Ni–Fe–Cu-based anode

Ni–Fe–Cu-based alloys are leading candidates for the development of oxygen evolving inert anode, primarily due to their ability to form a protective $NiFe_2O_4$ oxide scale. Furthermore, these alloys offer superior electrical conductivity and thermal shock resistance, providing significant advantages over the cermet anodes initially proposed by Alcoa[15]. As a result, Beck tested metallic anodes composed of Ni–Fe–Cu alloys, with compositions of 70–80 wt.% Cu, 10–15 wt.% Ni, and 10–15 wt.% Fe[26,27]. Testing in an alumina slurry cell demonstrated poor current efficiency (20–50%) and high contamination of copper (>0.1

wt.%) in the produced aluminum. This poor performance was attributed to back reactions involving direct contact between the molten aluminum placed above the oxygen evolving horizontal anode at the bottom of the cell.

Northwest Aluminum Company tested a single-phase homogenized Cu_{20}-Ni_{40}-Fe_{40} alloy, developed by Gallino et al., in 150 A cells for over 500 h at an 810 ^{o}C bath, achieving a current efficiency of 95% with anode contamination of less than 0.1 wt.%[29,32]. In contrast, the as-cast inhomogeneous alloy, containing a dual-phase structure, was found to be susceptible to corrosion, leading Gallino et al. to recommend the use of a single-phase homogenized alloy[32]. The main degradation mechanism of the inhomogeneous alloy was identified as tunneling and galvanic corrosion, leading to the formation of metal fluorides[32,33]. Ying et al. tested a Cu_{52}-Ni_{30}-Fe_{18} alloy in both as-cast and homogenized forms at an 850 ^{o}C bath[49]. Similar to Gallino et al. findings[32], the as-cast alloy showed instability, with fluorides and aluminates detected on the surface[49]. The homogenized alloy performed better, but both variants resulted in significant iron contamination (>0.6 wt.%) in the produced aluminum.

Jucken et al. tested homogenized Cu-rich (Cu_{65}-Ni_{20}-Fe_{15}) and Ni-rich (Ni_{65}-Fe_{25}-Cu_{10}) alloys at 700 ^{o}C[50]. They concluded that homogenization treatment significantly improved the performance of Cu-rich alloys in terms of cell voltage stability, but copper contamination in the produced aluminum remained between 0.26–0.32 wt.%. In contrast, Ni-rich anodes exhibited high susceptibility to fluoride formation, which led to elevated contamination levels of Ni and Fe in the produced aluminum, reaching 2.9 wt.% and 1.4 wt.%, respectively[50]. Furthermore, Helle et al. confirmed the poor performance of Ni-rich alloys, investigating a Ni_{71}-Fe_{15}-Cu_{14} alloy for 700 ^{o}C bath temperature, where they observed unstable cell voltage due to the formation of a thick NiO and $FeAl_2O_4$ scale[51]. On the other hand, when using Cu-rich alloys, both, Helle et al. and Gavrilova et al. demonstrated stable cell voltage for Cu_{55}-Ni_{25}-Fe_{20}, Cu_{65}-Ni_{20}-Fe_{15} and Cu_{70}-Ni_{15}-Fe_{15} compositions for electrolysis at 700 ^{o}C, attributed to the formation of a dense and conductive copper oxide layer along with $NiFe_2O_4$[51,52]. Nevertheless, Cu contamination in the produced aluminum exceeded 0.2 wt.%[51], which is unacceptable for the primary aluminum quality standards.

Interestingly, to pre-form a protective oxide scale, Gunnarsson et al. tested a single-phase homogenized Ni_{40}-Fe_{40}-Cu_{20} alloy by conducting a high temperature oxidation treatment at 800 ^{o}C[42]. This treatment led to improved anode stability and a stable cell voltage evolution during electrolysis at 800 ^{o}C, with anode related contamination below 0.14 wt.% in the produced aluminum.

In summary, numerous Ni–Fe–Cu alloy compositions have been investigated over the past decade, with a focus on improving their viability for inert anode applications. The results suggest that homogenizing these alloys generally enhances anode stability and performance during electrolysis. Ni-rich alloys, however, consistently show drawbacks, including susceptibility to fluoride formation and significant Ni and Fe contamination in the produced aluminum. On the other hand, Cu-rich alloys tend to provide better voltage stability but still introduce unacceptable levels of copper contamination. Despite these findings, there is still no consensus on the optimal Ni–Fe–Cu alloy composition for inert anode applications. In this study, a range of single-phase, homogenized Ni–Fe–Cu alloys have been evaluated for their potential use in inert anode applications for aluminum production.

2.3 TiB_2 ceramic cathode

Titanium diboride (TiB_2) is the best known ceramic material for wettable aluminum cathode for inert electrode technology[53]. This is because of its excellent chemical stability in molten fluoride bath, high wettability with liquid aluminum, and good electrical conductivity[54–56]. In light of these properties, this work utilizes a fine-grained (2-3 µm), high-purity TiB_2 cathode, produced by hot pressing.

2.4 Low temperature electrolyte

The development of inert anode using the conventional electrolyte of Hall–Héroult process has faced significant challenges due to two major reasons. Firstly, the high operating temperature of the bath (966 ^{o}C) significantly increases the corrosion rate of metallic anodes. Secondly, this high temperature also increases the solubility of oxides, particularly those protective oxides that form on the oxygen evolving anode surface[57]. To address both challenges—namely, reducing the corrosion rate of the anode alloy and minimizing the dissolution of protective oxides in the electrolyte— it is advantageous to use lower temperature electrolytes, specifically those with liquidus temperatures below 800 ^{o}C[58].

However, the choice of electrolytes is effectively limited to NaF-AlF_3 and KF-AlF_3, owing to their high alumina solubility, about 11 wt.% and 23 wt.% at 1000 ^{o}C, respectively, without addition of excess AlF_3 [59]. Lowering the liquidus temperature of these electrolytes can be achieved by decreasing the cryolite ratio (r = (NaF, KF)/AlF_3 in molar ratio), which involves adding an excess of AlF_3. However, increasing AlF_3 content has the downside of reducing alumina solubility in the electrolyte[60]. To address this limitation while maintaining the bath in a saturated state, Beck proposed the use of a slurry cell with excess alumina in a eutectic composition of NaF-AlF_3 (r = 1.17, Al_2O_3 solubility ~3 wt.%) at 750 ^{o}C[27]. Nevertheless, this approach resulted in low current efficiency and potential metal contamination from the excess suspended alumina, making it impractical for further development.

Interestingly, KF-AlF_3 electrolytes exhibit relatively higher alumina solubility at lower cryolite ratios compared to conventional NaF-AlF_3 electrolytes[58]. For instance, at a cryolite ratio of 1.22, alumina solubility reaches about 5 wt.% at 730 ^{o}C[58]. However, there are two main drawbacks related to the use of KF-AlF_3 electrolytes. Firstly, the electrical conductivity of the bath decreases significantly— at r = 1.22, the conductivity is 1.15 $\Omega^{-1}cm^{-1}$ at 800 ^{o}C, compared to 2 $\Omega^{-1}cm^{-1}$ for conventional electrolyte baths[58]. Secondly, there is a practical issue regarding the change in bath composition over time, largely due to sodium introduced from the Bayer process along with alumina feed. This results in a dramatic change in the cryolite ratio, ultimately affecting the alumina solubility in a low cryolite ratio KF-AlF_3-based bath.

To overcome these issues, a new electrolyte composition involving KF-AlF_3 with the addition of NaF was developed. The addition of NaF helps address the variability introduced by sodium from alumina feed, while also increasing the electrical conductivity of the KF-AlF_3 electrolyte[60,61]. Although the addition of NaF partially reduces alumina solubility. For example, the alumina solubility for a cryolite ratio (KF+NaF)/AlF_3 = 1.3 in molar ratio, with NaF additions of 7 wt.% and 26 wt.%, is about 5.7 wt.% and 4 wt.%, respectively[60]. However, decrease in electrical conductivity can be improved by compact cell design with reduced interpolar distance. Work in this thesis focuses on the use of a range of KF-NaF-AlF_3-based low temperature electrolyte at an 800 ^{0}C bath, balancing both alumina solubility and electrical conductivity.

References

[1] I. Galasiu, R. Galasiu, J. Thonstad, Inert Anodes for Aluminium Electrolysis, Beuth Verlag GmbH, 2011.
[2] M.H. Charles, Process of reducing aluminium from its fluoride salts by electrolysis, Patent US400664A, 1889.
[3] A.I. Belyaev, A.E. Studentsov, Electrolysis of alumina with non-combustable (metallic) anodes, Legkie Metally. 5 (1936) 15–24.
[4] A.I. Belyaev, A.E. Studentsov, Electrolysis of Alumina with Oxide Anodes, Legkic Metal. 6 (1937) 17–22.
[5] A.I. Belyaev, Electrolysis of Aluminum with Ferrite Anodes, Legkie Metal. 7 (1938) 7–20.
[6] J.W. Cuthbertson, J. Waddington, A study of the cryolite–alumina cell with particular reference to decomposition voltage, Transactions of the Faraday Society. 32 (1936) 745–760.
[7] J. Thonstad, Anodic overvoltage on platinum in cryolite-alumina melts, Electrochimica Acta. 13 (1968) 449–456.
[8] H. Klein, Process for the electrolytic production of aluminum, Patent US3718550A, 1973.
[9] H. Alder, Electrolysis of a molten charge using incomsumable electrodes, Patent US3960678A, 1976.
[10] H. Xiao, On the corrosion and the behavior of inert anodes in aluminium electrolysis, Norges Tekniske Hoegskole Trondheim, Norway, 1993.
[11] A.-M. Popescu, Current Efficiency Obtained with SnO2-based Inert Anodes in Laboratory Aluminium Cell, Zeitschrift Für Naturforschung A. 56 (2001) 735–738.
[12] A.-M. Popescu, S. Mihaiu, S. Zuca, Microstructure and Electrochemical Behaviour of some SnO2-based Inert Electrodes in Aluminium Electrolysis, Zeitschrift Für Naturforschung A. 57 (2002) 71–75.
[13] H. Wang, J. Thonstad, The behavior of inert anodes as a function of some operating parameters, in: Journal of Metals, The Minerals, Metals & Materials Society, 1988: pp. 101–101.
[14] Y.X. Liu, J. Thonstad, Oxygen overvoltage on SnO2-based anodes in NaF-AlF3-Al2O3 melts. Electrocatalytic effects of doping agents, Electrochimica Acta. 28 (1983) 113–116.

[15] J.D. Weyand, D.H. DeYoung, S.P. Ray, G.P. Tarcy, F.W. Baker, Inert anodes for aluminum smelting, Final Report, Alcoa, Aluminium Company of America, Alcoa Laboratories, Alcoa Center. (1986) 40158–20.

[16] T.R. Beck, R.J. Brooks, Method and apparatus for electrolytic reduction of alumina, US4592812A, 1986.

[17] T.R. Beck, R.J. Brooks, Electrolytic reduction of alumina, US4865701A, 1989.

[18] V.D. Nora, P.M. Spaziante, A. Nidola, Sintered electrodes with electrocatalytic coating, Patent US4146438A, 1979.

[19] T. Nguyen, A. Lazouni, K.S. Doan, Non-consumable anode for molten salt electrolysis, Patent US4956068A, 1990.

[20] V.D. Nora, T.T. Nguyen, Non-carbon anodes, Patent WO2005090643A2, 2005.

[21] S.P. Ray, Inert anodes for Hall cells, Light Metals 1986. 2 (1986) 287–298.

[22] F.W. Baker, R.L. Rolf, Hall cell operation with inert anodes, Light Metals 1986. 2 (1986) 275–286.

[23] G.P. Tarcy, Corrosion and Passivation of Cermet Inert Anodes in Cryolite-Type Electrolytes, in: Essential Readings in Light Metals: Volume 4 Electrode Technology for Aluminum Production, Springer, 2016: pp. 1082–1093.

[24] D.H. DeYoung, Solubilities of Oxides for Inert Anodes in Cryolite-Based Melts, in: A. Tomsett, J. Johnson (Eds.), Essential Readings in Light Metals: Volume 4 Electrode Technology for Aluminum Production, Springer International Publishing, Cham, 2016: pp. 1073–1081.

[25] J. Windisch C.F., D.M. Strachan, Inert Electrodes Program: Fiscal year 1990 annual report, United States, 1991.

[26] T.R. Beck, A Non-Consumable Metal Anode for Production of Aluminum with Low-Temperature Fluoride Melts, Essential Readings in Light Metals: Volume 4 Electrode Technology for Aluminum Production. 4 (2016) 1104–1109.

[27] T.R. Beck, Production of Aluminum with Low Temperature Fluoride Melts, in: G. Bearne, M. Dupuis, G. Tarcy (Eds.), Essential Readings in Light Metals: Volume 2 Aluminum Reduction Technology, Springer International Publishing, Cham, 2016: pp. 89–95.

[28] T.R. Beck, A New Energy-Efficient and Environmentally Friendly Process to Produce Aluminum, JOM. 65 (2013) 267–271.

[29] D.R. Bradford, Inert Anode Life in Low Temperature Reduction Process, Northwest Aluminum Technologies, The Dalles, Oregon, 2005.

[30] I. Gallino, Phase diagram, thermal stability, and high temperature oxidation of the ternary Cu-Ni-Fe system, PhD thesis, Oregon State University, 2004.

[31] I. Gallino, S. Curiotto, M. Baricco, M.E. Kassner, R. Busch, Homogenization of Highly Alloyed Cu-Fe-Ni: A Phase Diagram Study, J Phs Eqil and Diff. 29 (2008) 131–135.

[32] I. Gallino, M.E. Kassner, R. Busch, Oxidation and corrosion of highly alloyed Cu–Fe–Ni as inert anode material for aluminum electrowinning in as-cast and homogenized conditions, Corrosion Science. 63 (2012) 293–303.

[33] T.R. Beck, C.M. Macrae, N.C. Wilson, Metal Anode Performance in Low-Temperature Electrolytes for Aluminum Production, Metall Mater Trans B. 42 (2011) 807–813.

[34] T.M. Leeuwen, An Aluminum Revolution, Desk Notes. (2000).

[35] R. von Kaenel, Technical and economical evaluation of the de NORA inert metallic anode in aluminum reduction cells, Light Metals. (2006) 397–402.

[36] T. Nguyen, De Nora oxygen evolving inert metallic anode, Light Metals. 385 (2006).

[37] J. Antille, L. Klinger, R. von Kaenel, Modeling of a 25 kA de Nora inert metallic anode test cell, Light Metals. (2006) 391–396.

[38] ELYSIS progresses on the commercialization of its breakthrough technology by issuing its first smelter technology licence, (n.d.). https://www.elysis.com/en/issuing-first-smelter-technology-licence (accessed November 4, 2024).

[39] X. Liu, Electrode configurations for electrolytic cells and related methods, Patent US11585003B2, 2023.

[40] C. Barthelemy, S. Bouvet, A. Gabriel, V. Laurent, A. Marmottant, Materiau d'electrode et son utilisation pour la fabrication d'anode inerte, Patent CA2952263A1, 2015.

[41] T.R. Beck, Aluminum production cell, Patent US8480876B2, 2013.

[42] G. Gunnarsson, G. Óskarsdóttir, S. Frostason, J.H. Magnússon, Aluminum Electrolysis with Multiple Vertical Non-consumable Electrodes in a Low Temperature Electrolyte, Light Metals 2019. (2019) 803–810.

[43] C.M. Medino, Improving current efficiency in low-temperature aluminum electrolysis with vertical inert electrodes, MSc thesis, 2019.

[44] D. T. Gunnarsson, Optimization of operating parameters of a carbon free aluminum electrolysis cell with vertical Inert Cu/Ni/Fe anodes, MSc thesis, 2023.

[45] K. Singh, G. Gunnarsson, J.H. Magnusson, G.M. Haarberg, G. Saevarsdottir, Performance Evaluation of Low-Temperature KF-NaF-AlF3 Electrolytes for Aluminum Electrolysis Using Vertical Inert Cu–Ni–Fe Alloy Anodes, Journal of The Electrochemical Society. 170 (2023) 113507.

[46] K. Singh, G.M. Haarberg, A.R. Mallah, G. Gunnarsson, T.L. Jamieson, I. Gallino, G. Saevarsdottir, Overpotential on Oxygen-Evolving Platinum and Ni-Fe-Cu Anode for Low-Temperature Molten Fluoride Electrolytes, JOM. 76 (2024) 3284–3293.

[47] Production of inert metallic anodes, (n.d.). https://www.trimet.eu/en/trimet/sustainability/environmental-and-climate-protection/production-of-inert-metallic-anodes (accessed November 4, 2024).

[48] Press-releases RUSAL 20-Nov-2024, (n.d.). https://rusal.ru/en/press-center/press-releases/rusal-conducts-first-ever-preheating-and-start-up-of-aluminium-reduction-cell-using-inert-anodes/ (accessed November 25, 2024).

[49] L. Ying, C. Dengpeng, W. Wei, L. Dongsheng, W. Junwei, L. Yudong, S. Zhirong, Influences of heat treatment on the oxidation and corrosion behavior of Cu–Ni–Fe inert anodes for aluminium electrolysis, Journal of Alloys and Compounds. 832 (2020) 154848.

[50] S. Jucken, B. Tougas, B. Davis, D. Guay, L. Roué, Study of Cu-Ni-Fe Alloys as Inert Anodes for Al Production in Low-Temperature KF-AlF3 Electrolyte, Metall Mater Trans B. 50 (2019) 3103–3111.

[51] S. Helle, M. Pedron, B. Assouli, B. Davis, D. Guay, L. Roué, Structure and high-temperature oxidation behaviour of Cu–Ni–Fe alloys prepared by high-energy ball milling for application as inert anodes in aluminium electrolysis, Corrosion Science. 52 (2010) 3348–3355.

[52] E. Gavrilova, G. Goupil, B. Davis, D. Guay, L. Roué, On the key role of Cu on the oxidation behavior of Cu–Ni–Fe based anodes for Al electrolysis, Corrosion Science. 101 (2015) 105–113.

[53] C.E. Ransley, Refractory Carbides and Borides for Aluminum Reduction Cells, JOM. 14 (1962) 129–135.

[54] S.K. Padamata, K. Singh, G.M. Haarberg, G. Saevarsdottir, Wettable TiB2 Cathode for Aluminum Electrolysis: A Review, Journal of Sustainable Metallurgy. 8 (2022).

[55] D.A. Weirauch Jr, W.J. Krafick, G. Ackart, P.D. Ownby, The wettability of titanium diboride by molten aluminum drops, Journal of Materials Science. 40 (2005) 2301–2306.

[56] E. Kubiňáková, M. Benköová, P. Veteška, Ľ. Bača, J. Híveš, Surface characterisation and wettability of titanium diboride by aluminium at low temperature, Advances in Applied Ceramics. 119 (2020) 22–28.

[57] J. Thonstad, S. Rolseth, Alternative electrolyte compositions for aluminium electrolysis, Mineral Processing and Extractive Metallurgy. 114 (2005) 188–191.

[58] A. Redkin, A. Apisarov, A. Dedyukhin, V. Kovrov, Y. Zaikov, O. Tkacheva, J. Hryn, Recent Developments in Low-Temperature Electrolysis of Aluminum, ECS Trans. 50 (2013) 205.

[59] E. Robert, J.E. Olsen, V. Danek, E. Tixhon, T. Østvold, B. Gilbert, Structure and Thermodynamics of Alkali Fluoride−Aluminum Fluoride−Alumina Melts. Vapor Pressure, Solubility, and Raman Spectroscopic Studies, J. Phys. Chem. B. 101 (1997) 9447–9457.

[60] A. Apisarov, A. Dedyukhin, O. Tkacheva, E. Nikolaeva, Y. Zaikov, P. Tinghaev, Physical-chemical properties of the KF-NAF-ALF3 molten system with low cryolite ratio, TMS Annual Meeting. (2009) 401–403.

[61] A. Apisarov, A. Dedyukhin, E. Nikolaeva, P. Tinghaev, O. Tkacheva, Y. Zaikov, Liquidus Temperatures of Cryolite Melts With Low Cryolite Ratio, Metallurgical and Materials Transactions B. 42 (2010) 236–242.

This page is intentionally left blank.

Chapter 3

Performance Evaluation of Low-Temperature KF-NaF-AlF_3 Electrolytes for Aluminum Electrolysis Using Vertical Inert Cu-Ni-Fe Alloy Anodes

Kamaljeet Singh[1,2,*], Gudmundur Gunnarsson[3], Jon Hjaltalin Magnusson[4], Geir Martin Haarberg[2], Gudrun Saevarsdottir[1,2]

[1]Department of Engineering, Reykjavik University, 102 Reykjavik, Iceland
[2]Department of Materials Science and Engineering, NTNU, 7491 Trondheim, Norway
[3]Taeknisetur IceTec, Arleynir 8, 112 Reykjavik, Iceland
[4]Arctus Aluminium Limited, Arleynir 8, 112 Reykjavik, Iceland
*Corresponding author: kamaljeets@ru.is

3.1 Abstract

In this study, the performance of low-temperature electrolytes in a 40 A laboratory oxygen-evolving aluminum electrolysis cell with vertical inert electrodes for two compositions of NaF-KF-AlF_3-based electrolyte is investigated. Two compositions of Cu-Ni-Fe alloy, single-phase homogenized, 20Cu-42Ni-38Fe and 5Cu-48Ni-47Fe (in wt%), are evaluated as anodes. Titanium diboride (TiB_2) is used as a wetted cathode. The characteristics of a protective oxide layer, pre-formed on the anode through high-temperature air oxidation, are examined using X-ray diffraction (XRD) and scanning electron microscopy (SEM). It is found that a multilayered oxide morphology, revealing Fe_2O_3 and $NiFe_2O_4$ as major constituents, is dense and adherent to the base alloy. The effects of electrolyte compositions, anode alloys, and electrolysis conditions on cell voltage evolution, current efficiency, contamination levels in the electrolyte and produced aluminum, and anode wear rate are systematically studied. A protective oxide layer, formed through oxidation treatment on the 20Cu-42Ni-38Fe wt% alloy, not only remains compact post-electrolysis but also performs significantly better in a K-rich electrolyte in terms of wear rate and the purity of the aluminum obtained. Influences of electrolyte composition on anode degradation behavior are discussed.

3.2 Introduction

Although the first patent on oxygen-evolving inert anode for primary aluminum electrolysis was filed by the co-inventor of the conventional Hall-Héroult process about 133 years ago, an industrial process did not materialize, and this idea is still being researched globally in laboratories and pilot cells.[1–6] The main idea is to replace the consumable carbon anode with a non-consumable inert anode, thus producing O_2(g) as per reaction (1) rather than CO_2(g) as per reaction (2) at the anode. The Hall-Héroult process requires high energy and produces greenhouse gas emissions, mainly carbon dioxide and perfluorocarbon.[7] Using inert anode technology results in zero greenhouse gas emissions. Additionally, a new compact cell design that utilizes both sides of the anodes and cathodes, wettable cathodes, and low-temperature electrolyte, could potentially result in overall energy savings, as shown in Fig. 1.[2–6]

Inert anode, $$\tfrac{1}{2}\mathrm{Al_2O_{3(diss.)}} = \mathrm{Al_{(l)}} + \tfrac{3}{4}\mathrm{O_{2(g)}} \quad (1)$$

Hall-Héroult, $$\tfrac{1}{2}\mathrm{Al_2O_{3(diss.)}} + \tfrac{3}{4}\mathrm{C_{(s)}} = \mathrm{Al_{(l)}} + \tfrac{3}{4}\mathrm{CO_{2(g)}} \quad (2)$$

The International Aluminum Institute presented a scenario to limit global warming to 1.5 degrees by 2050 by reducing emissions from 16.1 to 0.5 CO_2-equivalent per tonne of aluminum.[8] These objectives can be realized through inert anode technology, renewable energy, thermal management, and efficient recycling.[8,9]

The search for an ideal inert anode material that focuses on high-temperature corrosion resistance, good conductivity, thermal stability, and being economically viable for commercial applications has not yet been successful.[6,7] The development of a Cu-Ni-Fe alloy-based inert anode has received considerable attention in recent years because of its protective $NiFe_2O_4$ oxide layer.[2–7,10–12] Beck[3] evaluated many compositions of Cu-Ni-Fe alloys and suggested an optimal range for reduced oxidation rate in a low-temperature eutectic NaF-AlF_3 electrolyte at 750 ^{0}C. In Cu-Ni-Fe alloy, the Ni to Fe ratio is essential for $NiFe_2O_4$ oxide formation during the anodic reaction with oxygen, while the role of Cu remains debated in the literature.[5,10–12] Helle et al.[11] and Gavrilova et al.[12] have demonstrated the critical role of a high concentration of Cu, ranging from 65-70 wt%, in mechanically alloyed Cu-Ni-Fe anodes for stable cell voltage during electrolysis using two-electrode cell configurations with a current rating of less than 5 A. In contrast, Gallino et al.[10] and Gunnarsson et al.[5] have shown stable cell voltage with a low Cu content ranging from 20-25 wt% in as-cast homogenized Cu-Ni-Fe anodes using three-electrode configurations with cell current ratings between 32 A and 150 A.

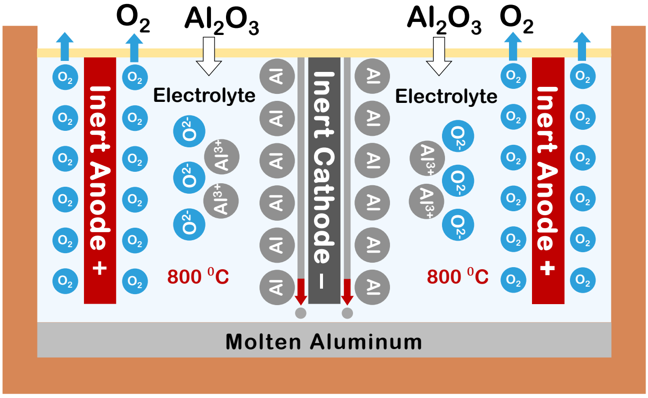

Fig. 1. Aluminum reduction process with vertical inert electrodes in low-temperature electrolyte at 800 ^{0}C (Copyright© Arctus 2023; printed with permission).

It has been established that homogenization heat treatment of Cu-Ni-Fe alloys results in a significant improvement in corrosion resistance compared to as-cast unhomogenized alloys.[5,10,13,14] According to Beck,[13] as-cast, two-phase alloy can develop corrosion tunnels as a result of selective corrosion of Fe and Ni, leading to the formation of their respective fluorides during electrolysis. To form a protective $NiFe_2O_4$ oxide, the surface of the alloy can be treated prior to electrolysis.[5,15,16] Recently, we have shown that a homogenized Cu-Ni-Fe alloy, pre-oxidized at 800 ^{0}C in air, performed better in terms of cell voltage stability and purity of produced aluminum than the non-oxidized anode.[5]

To reduce the high-temperature degradation of the oxygen-evolving metallic anode and the consequent contamination of the produced aluminum, low-temperature electrolytes are considered.[5,6,17] Using the eutectic composition of the NaF-AlF_3 electrolyte, 698 ^{0}C, results in decreased alumina (Al_2O_3) solubility of about 3 wt%.[7,17] To overcome this, partly replacing NaF with KF in the NaF-AlF_3 electrolyte increases alumina solubility and reduces the liquidus temperature, while K decreases the electrical conductivity. At 1000 ^{0}C, for example, the solubility of alumina in pure KF-AlF_3 is 2.6 times higher than in pure NaF-AlF_3.[18]

The current study focused on the examination of a Na-rich composition of NaF-KF-AlF_3 electrolyte, CR = (NaF+KF)/AlF_3 = 1.3 and KR = KF/(NaF+KF) = 0.3 (mole ratios), at a bath temperature of 800 ^{0}C and two anode compositions of Cu-Ni-Fe alloys in a laboratory cell with vertical electrodes. For comparison, a K-rich electrolyte with a CR = 1.3 and a KR = 0.8 was also tested. In the Na-rich electrolyte, part of the K in NaF-KF-AlF_3 has been replaced by Na, improving conductivity, reducing cell voltage, and energy use. Another advantage is that, in Na-cryolite, $NaAlF_4$ has a lower vapor pressure and is slightly less volatile than $KAlF_4$ in K-cryolite at the same temperature and cryolite ratio.[18] Additionally, Na salts are often less expensive than K salts. However, the solubility of alumina in the selected composition of Na-rich electrolyte is ~30% lower than in K-rich electrolyte;[19] see Table 1.

Two compositions of as-cast homogenized Cu-Ni-Fe alloy with low Cu wt%, 20Cu-42Ni-38Fe wt%, and 5Cu-48Ni-47Fe wt%, were evaluated as inert anodes. Both compositions lie outside the miscibility gap of the Cu-Ni-Fe ternary phase diagram, leading to a single-phase structure upon homogenization treatment.[20] Because of their suitability for mass manufacturing and industrialization, as-cast compositions are preferred. A protective $NiFe_2O_4$ oxide layer was pre-formed on the anode through a pre-oxidation treatment at 800 ^{0}C in air, and the composition of the oxide layer was studied. TiB_2 was selected as a cathode material due to its excellent aluminum wettability, superior high-temperature oxidation resistance, and stability in the bath.[7,21,22] A three-electrode configuration of anode-cathode-anode was used throughout these experiments with a constant anode-cathode distance (ACD) of 21 mm. Post-electrolysis, the current efficiency was calculated from the quantity of aluminum obtained, and the level of contamination by electrode constituents in the aluminum and electrolyte was measured in order to enable the estimation of anode wear rate. The used anodes were characterized with X-ray diffraction (XRD) and scanning electron microscopy (SEM) coupled with energy dispersive spectroscopy (EDS) to study the morphology and composition of the oxide layer.

Table 1. Physicochemical properties of selected Na-rich and K-rich electrolyte compositions.

	Na-rich electrolyte CR = 1.3, KR = 0.3	K-rich electrolyte CR = 1.3, KR = 0.8	References
Liquidus temperature (^{0}C)	704	737	[23]
Density at 800 ^{0}C (g mL^{-1})	1.83	1.78	[24]
Alumina solubility (wt%)	4.0	5.7	[19]
Electrical conductivity (S cm^{-1})	1.32	1.28	[19]

3.3 Experimental

Electrodes

Both compositions of Cu-Ni-Fe alloy were supplied by Arctus Aluminum, Iceland. The 20Cu-42Ni-38Fe wt% composition was a cast and homogenized alloy;[5] while the 5Cu-48Ni-47Fe wt% composition was a commercial-grade hot-rolled single-phase alloy. For homogenization treatment, the alloy was annealed at 1100 ^{o}C for 12 h, followed by water quenching.[20]

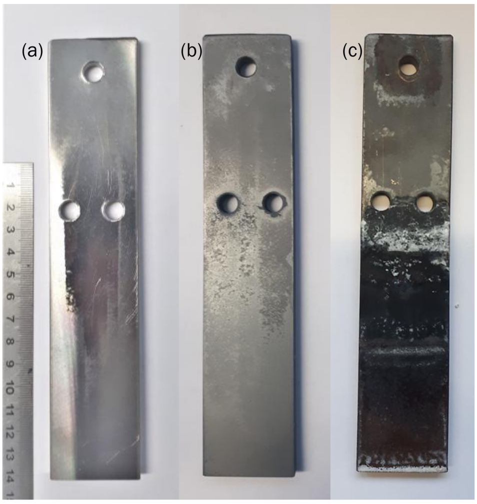

Fig. 2. Typical appearance of a Cu-Ni-Fe alloy anode, (a) before and (b) after pre-oxidation in air at 800 ^{o}C for 8 h, respectively, and (c) after electrolysis for 12 h at a bath temperature of 800 ^{o}C.

The anode for electrolysis, size 200 x 40 x 8 mm, was cut-off from a larger plate by water jet cutting and finished by milling with a surface roughness value (R_a) measuring about 0.2-0.4 µm. Following this, the anode was cleaned with ethanol and pre-oxidized in air at 800 ^{o}C for 8 h before being cooled to room temperature in the furnace; see Fig. 2. The anode pre-oxidation temperature of 800 ^{o}C was selected to be close to the operating temperature of the electrolysis bath and low enough to avoid phase instability of the selected Cu-Ni-Fe alloy.[5,20]

The study of the pre-oxidation of Cu-Ni-Fe alloys was performed on a small sample of size 20 x 10 x 6 mm, and the surface was finished using 320-grit size abrasive paper. Samples were degreased with ethanol and then cleaned ultrasonically in distilled water. Pre-oxidation at 800 ^{o}C in air was performed for both a nominal time of 8 h and a prolonged duration of 80 h, because the oxide scale developed after such a long period is thicker and easier to analyze. Triplicate tests were conducted for each alloy, and specific weight gains were recorded.

The cathode was produced by hot-pressing fine-grained, high-purity (99.7%) TiB_2 ceramic (Plansee GmbH), size 180 x 40 x 10 mm. The microstructure of the TiB_2 cathode, with a grain size of 2-3 µm, is presented in Fig. 3.

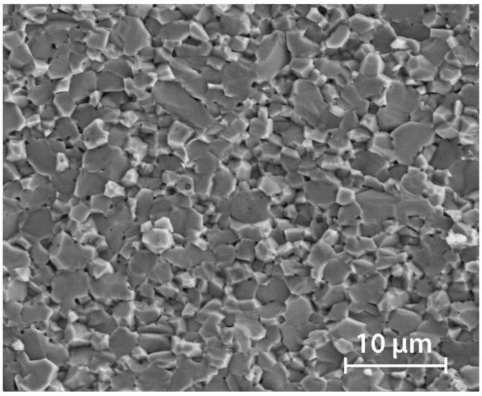

Fig. 3. The SEM image of the TiB_2 cathode shows fine grain microstructure.

Electrolyte

Na-rich electrolyte was composed of 26 wt% NaF (99.8% pure, VWR GmbH), 16 wt% KF (100% pure, VWR GmbH), and 58 wt% AlF_3 (97.6% pure, Alufluor AB Sweden) to give a CR of 1.3 and a KR = 0.3. K-rich electrolyte composition of CR = 1.3 and KR = 0.8 was composed of 7 wt% NaF, 39 wt% KF, and 54 wt% AlF_3. The initial amount of alumina (98.5% pure, Aluminum Oxid Stade GmbH) mixed with the electrolyte was about 70% of the solubility limit specified in Table 1. The compounds were dried at 200 ^{0}C for 24 h and weighed before mixing in a closed container. The total weight of the bath was about 1000 g.

Cell setup

Fig. 4 shows the schematic layout of the 40 A laboratory cell setup. The cell consists of an externally heated sintered alumina crucible, internal diameter 90 x depth 125 mm (Almath Crucibles, UK), placed inside a stainless-steel container. The crucible was closed with a commercial-grade ceramic lid and had multiple openings for electrodes, feeding, off-gas, and thermocouple tubes. The cathode was longer than the anode to keep the produced aluminum at cathode potential, with its end a few mm from the bottom. The ratio of the anode to cathode surface area was 0.75, assuming that the anode faces opposite the cathode faces carried all the current. A scheme of electrode connections has been shown elsewhere.[5]

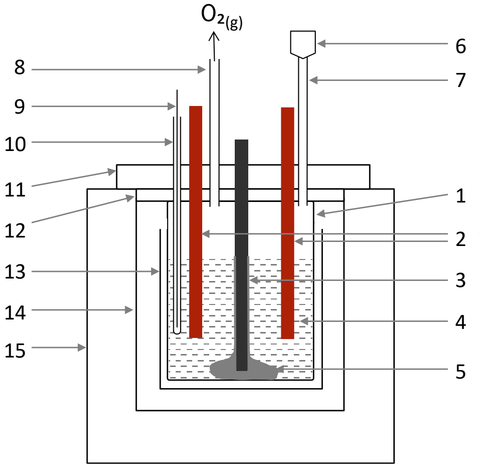

Fig. 4. Schematic diagram of the 40 A laboratory cell setup. 1- alumina crucible; 2- anodes 2x; 3- cathode 1x; 4- molten electrolyte; 5- produced aluminum; 6- alumina doser; 7- feeding tube; 8- off-gas tube; 9- thermocouple K-type; 10- thermocouple tube; 11- lid; 12- insulation; 13- stainless-steel container; 14- ceramic lining of furnace; 15- furnace.

Electrolysis

On start-up, the cell was heated to 300 ^{0}C for 5 h to remove any residual moisture content, then ramped up to 800 ^{0}C in steps. The lid containing the electrodes, pre-heated to 400 ^{0}C, was gradually introduced to the cell to reduce thermal shock. The electrolysis was started by switching on the direct current power supply (GEN1500W, TDK-Lambda UK). Electrolysis was performed with a nominal cathode current density of 0.51 A cm^{-2} and bath temperature of 800 ^{0}C. During electrolysis, cell parameters such as cell voltage, the temperature of the electrolyte and furnace were recorded every second using a data acquisition system (Agilent 34970A, USA), and the electrolyte was sampled before and after electrolysis using a 10 mL porcelain crucible.

For continuous feeding of alumina, automatic dosing equipment (Doser, Lambda Instruments GmbH) was used to supply 70-80% of the Al_2O_3 required for 100% current efficiency. The test duration, originally scheduled for 12 h, was limited in some cases to 6 to 10 h due to critical clogging in the alumina feeding channel, with no other technical challenges affecting the duration. Furthermore, using a crucible as an alternative for alumina feeding in this case posed a risk of leakage for an extended period of time. Alumina feeding could be improved by using a mechanical screw-type feeder.

The lid electrode assembly and crucible were removed from the furnace after electrolysis, cooled to room temperature, and aluminum was recovered from the frozen electrolyte by breaking the crucible. Any electrolyte deposits on the anodes above the bath level were removed using a chipping hammer. A typical appearance of the anode after electrolysis is shown in Fig. 2(c).

Sample characterization

Phases on the anode surface were investigated using XRD analysis (PANalytical Empyrean operating at 45 kV, Cu Kα 1.54060 Å, 2θ-scan with step size 0.026°). The anode was sectioned off using a low-speed diamond saw, molded in Bakelite hot mounting resin, and polished in successive stages, starting with a 200-grit size up to final 1 µm diamond paste. Microstructure analysis was performed using SEM (Carl Zeiss AG-Supra25) equipped with EDS (Oxford Instruments) for elemental analysis.

To estimate the wear rate of anode, the contamination from anode constituents (Cu, Ni, and Fe) in both the electrolyte and produced aluminum were measured by using inductively coupled plasma - optical emission spectrometry (ICP-OES) and spark - optical emission spectrometry (Spark-OES), respectively. The wear rate was determined using equation (3), where $\mathrm{m_e}$ and $\mathrm{m_{Al}}$ represent the mass of the electrolyte and produced aluminum, respectively (g), and $\mathrm{w_e}$ and $\mathrm{w_{Al}}$ represent the total amount of Cu, Ni, and Fe contaminates in the electrolyte and produced aluminum, respectively (wt%). ρ_a is the anode density (g cm^{-3}), A is the area of the anode (cm^2) immersed in the electrolyte, and t is the time of electrolysis (h). In equation (3), the initial level of contaminants (Cu, Ni, and Fe) present in electrolyte constituents and alumina must be compensated. Gibbs free energy (ΔG_r^0) data was obtained from HSC software.[25]

$$\text{Wear rate} = \frac{(\mathrm{m_e}\cdot\mathrm{w_e} + \mathrm{m_{Al}}\cdot\mathrm{w_{Al}}) \times 365 \times 24}{(\rho_a\cdot \mathrm{A}\cdot \mathrm{t})\times 10}, (\mathrm{mm\ year^{-1}}) \qquad (3)$$

3.4 Results and discussion

Influence of pre-oxidation treatment on oxide layer characteristics of Cu-Ni-Fe alloy

The outer surface of the oxide layer after pre-oxidation treatment was found to be adherent to the base alloy without any loose scale. The specific weight gain of each alloy is shown in Table 2. It is evident that the overall weight gain in the 20Cu-42Ni-38Fe wt% alloy is 28% (for 8 h) and 18% (for 80 h) more than in the 5Cu-48Ni-47Fe wt% alloy. Note that the Ni to Fe wt% ratio is nearly equal to unity in both alloys, while the Cu content varies considerably from 5 to 20 wt%. Clearly, the oxidation rate is greatly influenced by the Cu wt% in the alloy. Gallino et al.[10] showed that the parabolic rate constant K_p (oxidation at 800 °C, 1 atm O_2, 24 h) significantly decreases with decreasing Cu in the Cu-Ni-Fe alloy, i.e., from 2.12×10^{-9} to $4.17\ \times10^{-11}$ g^{2}cm^{-4}s^{-1} for 70Cu-15Ni-15Fe wt% and 40Cu-30Ni-30Fe wt%, respectively. Cheng et al.[26] determined the K_p value (oxidation at 750 °C, air, 24 h) to be $1.81\pm0.67 \times 10^{-11}$ g^{2}cm^{-4}s^{-1}, for 10Cu-79Ni-11Fe wt% composition.

Table 2. Specific weight gain of Cu-Ni-Fe alloy after pre-oxidation treatment in air for 8 h at 800 ^oC.

Alloy (wt%)	Specific weight gain (std. dev.) (mg cm^{-2})	
	8 h	80 h
20Cu-42Ni-38Fe	3.38 (0.61)	8.44 (0.42)
5Cu-48Ni-47Fe	2.43 (0.53)	6.93 (0.58)

The outer surface of the oxide layer of the alloy following pre-oxidation treatment was analyzed using XRD, which typically penetrates approximately ~5-10 µm underneath, thereby providing insight into the subsurface composition as well. Fig. 5 shows the XRD analysis results. For 8 h of oxidation time, two types of oxide compositions were observed:

i) Cu- and Fe-rich oxide: CuO, Fe_2O_3 and $NiFe_2O_4$ for alloy of 20Cu-42Ni-38Fe wt%, and
ii) Fe-rich oxide: Fe_2O_3 and $NiFe_2O_4$ for alloy of 5Cu-48Ni-47Fe wt% alloy.

Interestingly, after 80 h of oxidation, the intensity of XRD spectra of Cu-rich oxide increased relative to Fe-rich oxide for 20Cu-42Ni-38Fe wt%.

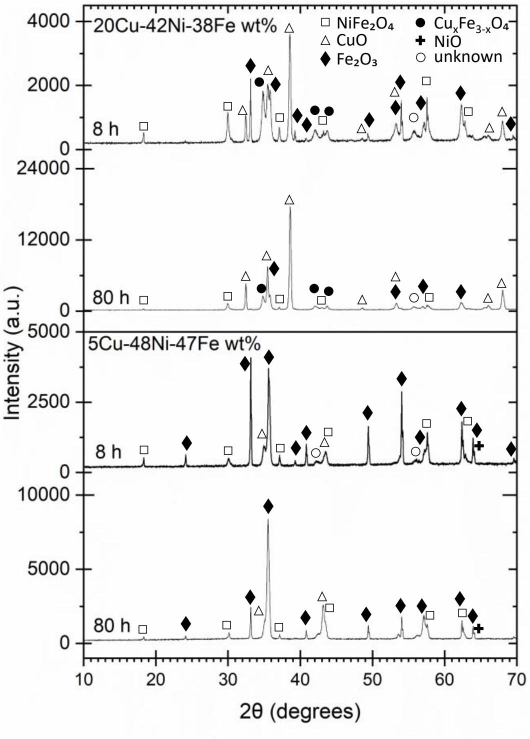

Fig. 5. XRD spectra of the surface of Cu-Ni-Fe alloy after pre-oxidation treatment in air for 8 h and 80 h at 800 ^oC.

The morphology and elemental composition of the cross-section of the oxide layer were examined by SEM and EDS line analysis, respectively. Fig. 6 shows the SEM image with an arrow indicating the position of line scan in the oxide layer with the head of the arrow pointing to the outer surface of oxide in contact with air. This study focused on the composition of the oxide layer. Hence, EDS line scans were only extended a few µm inside the depletion region- a dark grey islets region in base alloy formed by selective diffusion and oxidation. Furthermore, to provide a clearer representation of results, an attempt was made to simplify the depiction of various phases of the oxide layer.[27] The results are discussed with respect to each alloy composition hereafter.

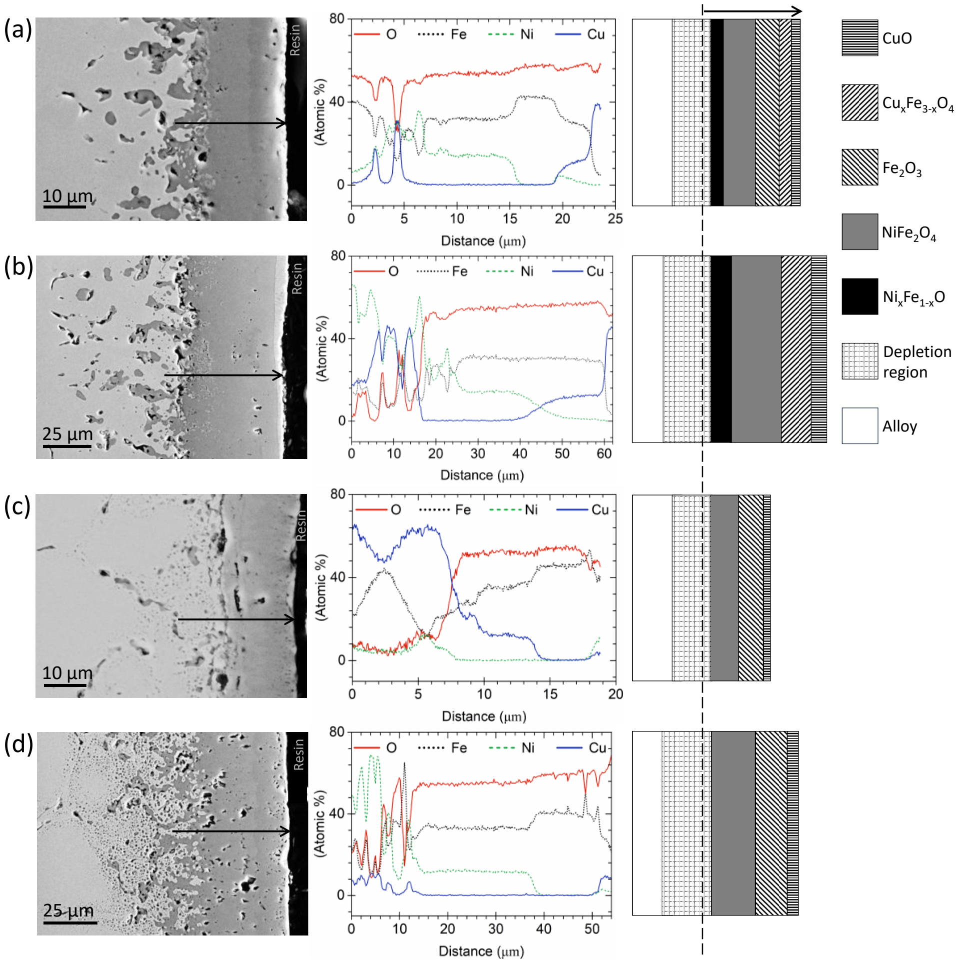

Fig. 6. SEM image of the cross-section of pre-oxidized sample of Cu-Ni-Fe alloy at 800 ^{0}C in air for 20Cu-42Ni-38Fe wt% alloy in (a) 8 h and (b) 80 h, and 5Cu-48Ni-47Fe wt% alloy in (c) 8 h and (d) 80 h. The arrow in SEM image indicates the position of line scan of the oxide

layer presented in the middle. The image on the right is a schematic representation of various phases in oxide layer.

In case of the 20Cu-42Ni-38Fe wt% alloy, the cross-section of the oxide layer showed a dense and adherent layer of oxide formation in Fig. 6. The average thickness of the oxide layer was observed to increase with oxidation time, ranging from 25 µm at 8 h to 46 µm at 80 h. For 8 h of oxidation, the multi-layered oxide was composed of Cu- and Fe-rich oxides; major constituents were CuO, $Cu_xFe_{3-x}O_4$, Fe_2O_3, and $NiFe_2O_4$. The strong outward diffusion of Cu resulted in an increased intensity of CuO phase for an extended oxidation time of 80 h. As a result, the average thickness of outer CuO layer was approximately 7 µm, close to XRD beam penetration depth.

The oxidation of the Cu-Ni-Fe alloy at 800 ^{0}C can be studied with the relative thermodynamic stability of various oxide formations with decreasing equilibrium partial pressure of oxygen (atm) due to inward diffusion of oxygen, which can be ranked in the following order: CuO (10^{-3}), Cu_2O (10^{-9}), Fe_2O_3 (10^{-10}), NiO (10^{-14}), Fe_3O_4 (10^{-18}), FeO (10^{-19}).[28] Cu-oxide features CuO (rather than Cu_2O), a stable phase at higher oxygen activity (10^{-3} atm at 800 ^{0}C). However, the presence of small amounts of Cu_2O cannot be disregarded. Underneath the oxide layer, a Cu depletion region enriched in mainly Fe slows down the diffusion of Cu, which inhibits the growth of the outer Cu-oxide layer.[28]

A spinel of $Cu_xFe_{3-x}O_4$ formation was detected in the XRD spectra. Furthermore, EDS line analysis provided insight into phase detection. The EDS spectra indicate a spinel of $Cu_xFe_{3-x}O_4$ formation, a solid solution of CuO and Fe_2O_3, with a gradient of decreasing Cu and increasing Fe concentrations as the distance from the outer CuO phase increases. Double-mixed oxide formations, $CuFeO_2$ and $CuFe_2O_4$, have been reported in the literature for Cu-Fe binary alloys.[29] For 8 h of oxidation, Fe_2O_3 oxide phase was detected by the XRD spectra. The EDS analysis clearly showed Fe_2O_3 oxide phase when Cu gradient falls to a minimum in $Cu_xFe_{3-x}O_4$ spinel moving inward in oxide towards alloy. Remarkably, for an extended oxidation time of 80 h, strong Cu outward diffusion resulted in the growth of $Cu_xFe_{3-x}O_4$ spinel over Fe_2O_3 phase.

$NiFe_2O_4$ oxide phase formation was strongly detected by the XRD for 8 h of oxidation, and spectra were relatively weak for an extended oxidation time due to the growth of outer oxide phases. However, the EDS line analysis clearly indicates the $NiFe_2O_4$ oxide phase. The formation of $NiFe_2O_4$ can be explained as Fe being preferentially oxidized to Fe_2O_3. Further diffusion of Fe from alloy is limited through the Ni-enriched zone. Meantime, the oxygen activity falls to a sufficiently low level to form NiO, which immediately combines with Fe_2O_3 at 800 ^{0}C (negative ΔG_r^0, -22.89 kJ mol^{-1})[25] to form a thermodynamically stable and protective layer of $NiFe_2O_4$ oxide.

The $NiFe_2O_4$ layer serves as a barrier, limiting the inward diffusion of oxygen and outward diffusion of anode constituents, thus slowing the oxidation rate.[28] Interestingly, the formation of the $NiFe_2O_4$ layer develops a chemical gradient where Fe is consumed at a faster rate from the alloy than Ni. As a result, Ni was enriched at the oxide/alloy interface and might form $Ni_xFe_{1-x}O$ spinel at reduced oxygen activity, thus forming a semicontinuous layer of $Ni_xFe_{1-x}O$ spinel. Although not detected by XRD, the EDS line analysis shows a $Ni_xFe_{1-x}O$ spinel formation at oxide layer and depletion region interface. Additionally, the $Ni_xFe_{1-x}O$ spinel blocks the outward diffusion of Cu. It is evident in the EDS line analysis, where Cu is enriched below the semicontinuous layer of $Ni_xFe_{1-x}O$ spinel.

In case of the 5Cu-48Ni-47Fe wt% alloy, it developed a markedly distinct layered morphology of oxide layer, as shown in Fig. 6. The SEM image of the cross-section of oxide layer featured a relatively high-volume fraction of pores and oxidation defects within and at the oxide/alloy interface. As expected, the average thickness of oxide layer was found to increase with extended oxidation time from, 14 µm (8 h) to 40 µm (80 h).

According to the XRD results in Fig. 5 and the EDS line analysis in Fig. 6, the major constituents of the oxide layer are identified as Fe_2O_3 and $NiFe_2O_4$. The phase distribution in the oxide layer follows the same trend with varying times of oxidation. With reference to lower average values of weight gain in Table 2 and oxide thickness, Cu wt% variation notably influences the kinetics of oxide growth in Cu-Ni-Fe alloys. In contrast to 20Cu-42Ni-38Fe wt% alloy, the 5 wt% Cu concentration reduces the activity and rate of Cu outward diffusion. As a result, the gradient of Cu element and XRD spectra in Fig. 5 on outer oxide was relatively small compared to the alloy with 20wt% Cu. Thus, the outer layer of oxide was essentially thin CuO. This also explains the disappearance of intermediate $Cu_xFe_{3-x}O_4$ spinel, which was observed for 20Cu-42Ni-38Fe wt% alloy.

The strong preferential oxidation of Fe to Fe_2O_3 was detected in both the XRD and EDS line analyses. It was followed by protective $NiFe_2O_4$ oxide formation. Despite the enrichment of Ni observed at oxide/alloy interface, it differs significantly from $Ni_xFe_{1-x}O$ spinel formation seen earlier in case of the 20Cu-42Ni-38Fe wt% alloy, where O gradient remained unchanged while Ni at% increased. Haugsrud et al.[28] emphasized the critical role of Ni-oxide at the oxide/alloy interface in effectively slowing the rate of oxidation. Chapman et al.[16] observed the development of Ni-rich non-stoichiometric spinel at oxide/alloy interface as a solid solution of NiO and FeO in a binary alloy of 80Ni-20Fe wt%.

Apparently, the high-temperature oxidation kinetics of Cu-Ni-Fe-O system is a complex process affected by variables such as temperature, time, interdiffusion rate, and oxide stability. Earlier studies have shown that pre-oxidation treatment can improve the stability and performance of the anode alloy in molten cryolite.[5,16,30,31] Due to the complications of the aforementioned variables, determining a standard treatment method has proven difficult. The present study confirmed the development of a dense and adherent oxide layer, thanks to the protective $NiFe_2O_4$ layer, through experimental pre-oxidation treatment. However, a multi-layered structure of oxide growth in the repetitive sequence was not observed, as reported by many researchers, under the present experimental conditions.[10,12,16,26,28,30,31]

Effect of aluminum electrolysis conditions and cell voltage evolution

Table 3 presents a summary of six electrolysis experiments. Experiments 1, 2, and 3 utilized a Na-rich electrolyte composition with a 20Cu-42Ni-38Fe wt% alloy anode. The influence of cathode current density, ranging from 0.40 to 0.59 A cm^{-2}, on electrolysis was examined in these experiments. Experiment 4 used a Na-rich electrolyte composition with a 5Cu-48Ni-47Fe wt% alloy anode. Experiment 5 involved a comparison of the electrolysis performance using a K-rich electrolyte composition. Finally, experiment 6 evaluated the cell's behavior in a dynamic scenario by abruptly changing the bath temperature and cathode current density from their nominal values of 800 ^{0}C and 0.51 A cm^{-2}, respectively, during electrolysis.

Fig. 7 shows the voltage of the cell as a function of time during the electrolysis. The reported cell voltage in experiments 1 to 3, which includes the ohmic drop, increased with an increase in cathode current density; see Fig. 7. In experiment 4, the auto-tuning cycle of the furnace's proportional-integral-derivative (PID) control parameters caused the cell voltage to follow the temperature profile during the first hour. Following this, between 2 h and 8 h of electrolysis, the cell voltage gradually increased from 3.32 to 3.57 V. This phenomenon might be caused by the poor conductivity of the developing oxide layer on the anode surface, which may need a higher overpotential.

In experiment 6, the temperature of the bath and current density were varied across different segments labeled from 1 to 15. The temperature ranged from 800 ^{0}C to 810 ^{0}C, followed by 820 ^{0}C, and then decreased to lower temperatures of 790 ^{0}C, 783 ^{0}C, and 794 ^{0}C. The cathode current density was regulated at 0.40, 0.51, and 0.59 A cm^{-2} in different segments. For each segment, electrolysis was conducted for a minimum duration of 0.4 h. The results of each segment are detailed in Table 4 and Fig. 7. For instance, in segments 1, 2, and 3, the bath temperature was set to 800 ^{0}C with corresponding cathode current densities of 0.51, 0.59, and 0.40 A cm^{-2}, respectively.

The results of experiment 6 demonstrated that an increase in bath temperature or a decrease in cathode current density led to a decrease in cell voltage, as expected. For example, in segment 9, the cell voltage was 3.16 V at 820 ^{0}C with a low cathode current density of 0.40 A cm^{-2}. Fig. 7 revealed that the cell voltage remained stable even as the bath temperature and cathode current density changed between segments. The results indicate that the electrolysis cell responds steadily to rapid changes in cell amperage or bath temperature, suggesting its potential suitability for smart grid technology.

LECO analysis of electrolyte samples collected before and after electrolysis (not shown) revealed saturated alumina bath conditions in all experiments, assuming that O is only present in alumina. The cell voltage evolution is a critical evaluation parameter in electrolysis and was observed to be stable during the experiments.

Table 3. Electrolysis parameters and results.

Experiment	Units	1	2	3	4	5	6
CR = $(NaF+KF)/AlF_3$	(Mole ratios)	1.3	1.3	1.3	1.3	1.3	1.3
KR = KF/(NaF+KF)	(Mole ratios)	0.3	0.3	0.3	0.3	0.8	0.3
Cu-Ni-Fe alloy anode	(wt%)	20-42-38	20-42-38	20-42-38	5-48-47	20-42-38	20-42-38
Cathode	-	TiB_2	TiB_2	TiB_2	TiB_2	TiB_2	TiB_2
Bath temperature	(^oC)	800	800	800	800	800	783 to 820
Current	(A)	22	30	33	32	31	22, 28, 33
Cathode current density	(A cm-2)	0.40	0.51	0.59	0.51	0.51	0.40, 0.51, 0.59
Avg. cell voltage (std. dev.)	(V)	3.16 (0.02)	3.32 (0.12)	3.47 (0.02)	3.46 (0.09)	3.49 (0.02)	3.16 to 3.57 (-)
Time	(h)	12	6	12	8	10	10
Aluminum produced	(g)	69	52	107	76	74	73
Current efficiency	(%)	78	85	81	87	77	81

Table 4. Details of changes in electrolysis parameters in each segment of experiment 6.

Segment	Units	1	2	3	4	5	6	7	8	9	10	11	12	13	14	15
Time on x-axis	-	0-1.7	1.7-2.6	2.6-3.1	3.1-4	4-4.5	4.5-5	5-6	6-6.5	6.5-7	7-7.4	7.4-7.9	7.9-8.4	8.4-8.9	8.4-9.3	9.3-9.8
Time	(h)	1.7	0.9	0.5	0.9	0.5	0.5	1.0	0.5	0.5	0.4	0.5	0.5	0.5	0.4	0.5
Bath temperature	(^oC)	799	800	800	807	810	810	818	820	820	-	789	790	790	783	794
Cathode current density	(A cm^{-2})	0.51	0.59	0.40	0.51	0.59	0.40	0.51	0.59	0.40	-	0.51	0.59	0.40	0.51	0.51
Current	(A)	28.4	33	22.1	28.4	33	22.1	28.4	33	22.1	-	28.4	33	22.1	28.4	28.4
Avg. cell voltage	(V)	3.41	3.54	3.20	3.37	3.48	3.17	3.34	3.47	3.16	-	3.41	3.57	3.23	3.42	3.38

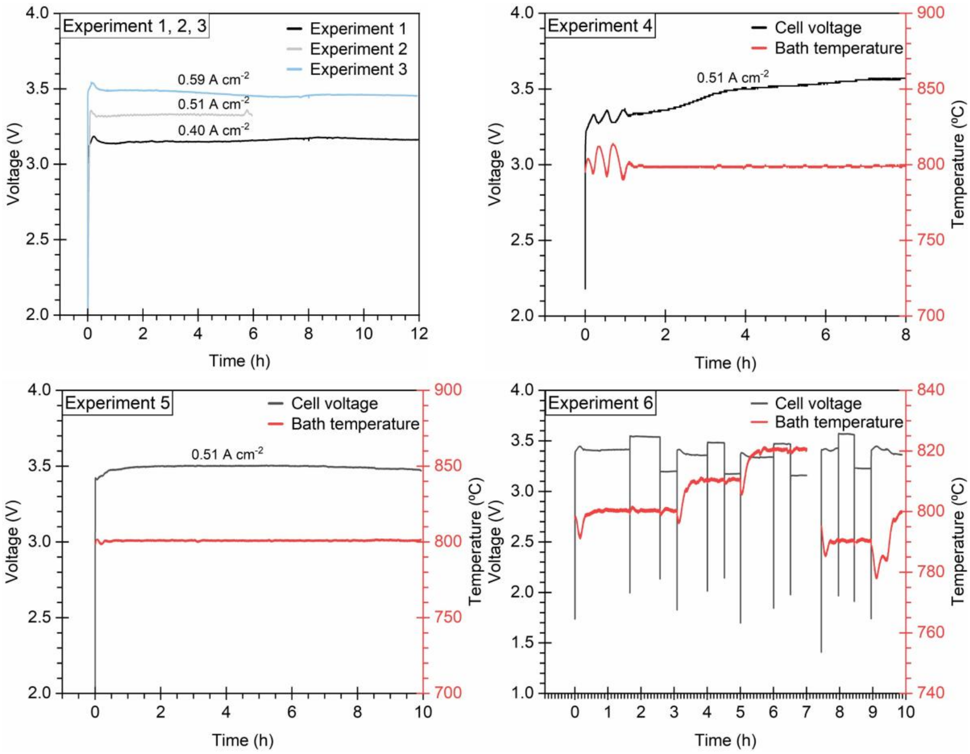

Fig. 7. Cell voltage profile plotted against electrolysis time for experiments 1 to 6 with specified cathode current density. ACD = 21 mm, bath temperature = 800 °C (except experiment 6, ranging from 783 to 820 °C).

Influence of cathode current density on current efficiency

As shown in Table 3, the overall current efficiency was in the range of 78–87%. The immersed length of TiB_2 cathode was found to be sufficiently wetted with a layer of aluminum deposit after removal at the end of electrolysis.

In the Hall-Héroult process, it is generally accepted that the cathode boundary layer establishes a concentration gradient.[7] Within this boundary layer, NaF is enriched while AlF_3 is depleted due to diffusion and migration processes. According to the equilibrium reactions (4) and (5), both NaF and KF diffuse into the cathode boundary layer in the NaF-KF-AlF_3-Al_2O_3 electrolyte. In the latter case, it is expected to contain more Na^+ ions than K^+ since the former is the primary charge carrier. However, it was shown by Cui et al.[32] that higher current densities increase the concentration of K^+ ions in the metal pad, which can lead to an increase in cathodic overvoltage. This effect was observed in the comparison between the cell voltage evolution of Na-rich and K-rich electrolytes. For examples, the cell voltage increased by 5%, from 3.32 V in experiment 2 to 3.49 V in experiment 5, when operating under similar electrolysis settings, as listed in Table 3. Although 3% lower conductivity of the K-rich electrolyte compared to the Na-rich electrolyte may also be a contributing factor here.[19]

$$\mathrm{Al} + 3\mathrm{KF} = 3\mathrm{K} + \mathrm{AlF_3} \qquad (4)$$

$$\mathrm{Al} + 3\mathrm{NaF} = 3\mathrm{Na} + \mathrm{AlF_3} \qquad (5)$$

Experiments 1, 2, and 3 examined the effect of cathode current density on current efficiency and found a maximum of 85% at 0.51 A cm^{-2} in experiment 2. This value closely aligns with the optimal current density suggested by recent studies.[33,34] However, with limited experimental data, it is difficult to draw firm conclusions about the relationship between current density and current efficiency. The selection of an appropriate cathode current density and optimal cell design parameters is crucial for smooth cell operation and high current efficiency.[5,32–34]

Anode wear rate and oxide layer characteristics post-electrolysis

Cu-Ni-Fe alloy, during oxygen evolution in aluminum electrolysis, can undergo a complex degradation mechanism. The oxidation as per reaction (6) is most desirable in inert anode technology as the oxide surface protects the alloy. While anodic dissolution, as per reaction (7) would degrade the alloy. The wear rate and lifespan of anode can be estimated based on the level of contamination in the electrolyte and produced aluminum.

$$\mathrm{xM} + \tfrac{\mathrm{y}}{2}\mathrm{O_2} = \mathrm{M_xO_y} \qquad (6)$$

$$\tfrac{1}{\mathrm{y}}\mathrm{M_xO_y} + \tfrac{2}{3}\mathrm{AlF_3} = \tfrac{\mathrm{x}}{\mathrm{y}}\mathrm{MF}_{2\frac{\mathrm{y}}{\mathrm{x}}} + \tfrac{1}{3}\mathrm{Al_2O_3} \qquad (7)$$

where M = Cu, Ni, Fe.

Post-electrolysis, the surface appearance of the anode was generally rough and partly corroded, but no loose flakes were observed, as seen in Fig. 2(c).

Table 5 shows the results of the chemical analysis of contamination in the electrolyte and the produced aluminum in terms of anode constituents (Cu, Ni, and Fe) for three experiments (3, 4, and 5) conducted under nearly identical conditions. The variations included varying electrolysis duration (8 to 12 h) due to alumina feeding issues and a higher cathode current density in experiment 3 (0.59 A cm^{-2}). We believe that it is more appropriate to compare anodes from experiments with longer electrolysis durations and slightly higher current densities rather than vice versa.

It was found that Fe contamination in the electrolyte was significantly higher than that of Ni and Cu. One explanation is the higher solubility of Fe-oxide in cryolite melts.[35] Similarly, in the case of produced aluminum, Fe was the major contamination, but Cu and Ni orders were specific to alloy composition, i.e., Fe>Cu>Ni for 20Cu-42Ni-38Fe wt% and Fe>Ni>Cu for 5Cu-48Ni-47Fe wt% alloy, respectively. This trend could be indicative of the mass transfer coefficient of anode species to the cathode. The level of Ti and B contamination from the TiB_2 cathode in the produced aluminum ranged from 0.02–0.04 wt% and 0.002–0.015 wt%, respectively.

Comparing the performance of alloys, the wear rate of the 20Cu-42Ni-38Fe wt% alloy, 7 mm year^{-1} in experiment 3, was relatively better than the 5Cu-48Ni-47Fe wt% alloy, 9 mm year^{-1} in experiment 4, possibly due to high anodic dissolution for the latter. The K-rich electrolyte showed better compatibility due to lower contamination compared to Na-rich electrolyte. The wear rate of the 20Cu-42Ni-38Fe wt% alloy was reduced by 2.33 times when tested in K-rich electrolyte (experiment 5) compared to Na-rich electrolyte (experiment 3). Consequently, the highest purity of produced aluminum was 99.7 wt% in experiment 5 with K-rich electrolyte, followed by 99.3 and 99.2 wt% in experiments 3 and 4, respectively. According to the literature, electrolysis tests for several days can significantly reduce the level of contamination after attaining steady-state conditions.[3,36,37]

Table 5. Level of contamination (wt%) in terms of anode constituents (Cu, Ni, and Fe) in the electrolyte and produced aluminum measured by ICP-OES and Spark-OES, respectively. The wear rate of anode is calculated according to equation (3).

	Contamination in electrolyte (wt%)				Contamination in produced aluminum (wt%)				Wear rate (mm year^{-1})
	Cu	Ni	Fe	Total	Cu	Ni	Fe	Total	
Experiment 3	0.001	0.001	0.006	0.008	0.035	0.016	0.63	0.68	7
Experiment 4	0.002	0.001	0.017	0.020	0.015	0.021	0.78	0.82	9
Experiment 5	0.001	0.001	0.006	0.008	0.013	0.004	0.28	0.30	3

The morphology and composition of the oxide layer of the used anodes in experiments 3, 4, and 5 are discussed based on the thermodynamic stability of compounds in the following sections. The SEM images of the cross-section of anode from the active side are shown in Fig. 8. The SEM image shows three distinct regions, marked as i) oxide layer, ii) depletion region, and iii) base alloy. Following that, EDS point analysis is shown for selected zones (zone 1 to 6) marked in the SEM image. Additionally, EDS mapping of the SEM image displays the distribution of O, Fe, Ni, Cu, Na, F, Al, and K elements. The XRD analysis of anode surface is shown in Fig. 9.

In experiment 3, the SEM image in Fig. 8 of the 20Cu-42Ni-38Fe wt% alloy anode shows a dense oxide layer adhered to the base alloy, with some electrolyte deposits on its surface. This morphology of the oxide layer helps explain the stable cell voltage observed during electrolysis in experiment 3, as shown above in Fig. 7. The average thicknesses of the oxide layer and depletion region were measured to be 20 µm and 88 µm, respectively. Further, the EDS point analysis and mapping revealed a complex structure within the oxide layer.

The EDS point analysis in Fig. 8(b) shows that outer layer (zone 1) is composed mainly of Fe_2O_3. Next, in zone 2, a mixture of Fe_2O_3 and NiO phases with an atomic ratio Ni:Fe:O = 1:2:4, combines to form a protective $NiFe_2O_4$ phase as per reaction (8).[28] The XRD analysis, shown in Fig. 9, further complemented this observation, confirming that $NiFe_2O_4$

and Fe_2O_3 are the major constituents of the oxide layer. Surprisingly, the outermost layer of oxide in contact with the bath was depleted in Cu, leaving behind a porous morphology. It is worth noting that during pre-oxidation treatment, the outer layer of the oxide was rich in CuO, as seen in Fig. 6. The depletion of CuO may be due to its high solubility in the electrolyte,[10,35] or it may have dissolved through fluoridation reactions, forming CuF_2 with a low melting point (836 ^oC).[25]

Interestingly, the XRD spectra revealed the presence of the $CuFe_2O_4$ phase, which is consistent with the $Cu_xFe_{3-x}O_4$ spinel layer observed during the pre-oxidation treatment of the alloy. Small peaks of nickel-aluminate ($NiAl_2O_4$) phase were also detected, which is a stable phase as per reaction (9) (negative ΔG_r^0) in the presence of high alumina activity.[38] However, iron-aluminate ($FeAl_2O_4$) was not detected in XRD analysis, which could form as per reaction (10). It is because Fe^{3+} is a more stable phase than Fe^{2+} in the presence of oxygen.[35] Therefore, $FeAl_2O_4$ could oxidize further to form Fe_2O_3 as per reaction (11) with a more negative ΔG_r^0.

$$\mathrm{NiO_{(s)} + Fe_2O_{3(s)} = NiFe_2O_{4(s)}} \quad ; \Delta G^\circ_{\mathrm{r,800℃}} = -22.89 \text{ kJ mol}^{-1} \tag{8}$$

$$\mathrm{NiO_{(s)} + Al_2O_{3\,(diss.)} = NiAl_2O_{4(s)}} \; ; \Delta G^\circ_{\mathrm{r,800℃}} = -16.47 \text{ kJ mol}^{-1} \tag{9}$$

$$\mathrm{FeO_{(s)} + Al_2O_{3\,(diss.)} = FeAl_2O_{4\,(s)}} \; ; \Delta G^\circ_{\mathrm{r,800℃}} = -14.51 \text{ kJ mol}^{-1} \tag{10}$$

$$\mathrm{FeAl_2O_{4(s)}} + \tfrac{1}{4}\mathrm{O_{2(g)}} = \tfrac{1}{2}\mathrm{Fe_2O_{3(s)}} + \mathrm{Al_2O_{3}}_{\,(s)} \; ; \Delta G^\circ_{\mathrm{r,800℃}} = -62.54 \text{ kJ mol}^{-1} \tag{11}$$

In the depletion region (zone 3 and 4), faster outward diffusion of Fe to form $NiFe_2O_4$ and blocking of Cu and Ni by the oxide barrier of $NiFe_2O_4$ resulted in Ni and Cu enrichment.[28] Zone 5 featured the formation of iron fluorides, which might be FeF_2 and FeF_3 according to possible anodic reactions (12) and (13), respectively. Notably, the presence of F element scattered spots deep inside the alloy, about 50 to 100 µm from the outer layer, illustrates the substantial activity of fluoride species in low-temperature electrolytes. For example, in an industrial bath with r = NaF/AlF_3 = 2.3 (mole ratios) at 960 ^oC, AlF_3 activity is about 2.9×10^{-3}, whereas for r = 1.3 at 800 ^oC, it is 1.4×10^{-1}.[39]

$$\mathrm{Fe + 2AlF_5^{2-} = FeF_2 + 2AlF_4^- + 2e^-} \tag{12}$$

$$\mathrm{Fe + 3AlF_5^{2-} = FeF_3 + 3AlF_4^- + 3e^-} \tag{13}$$

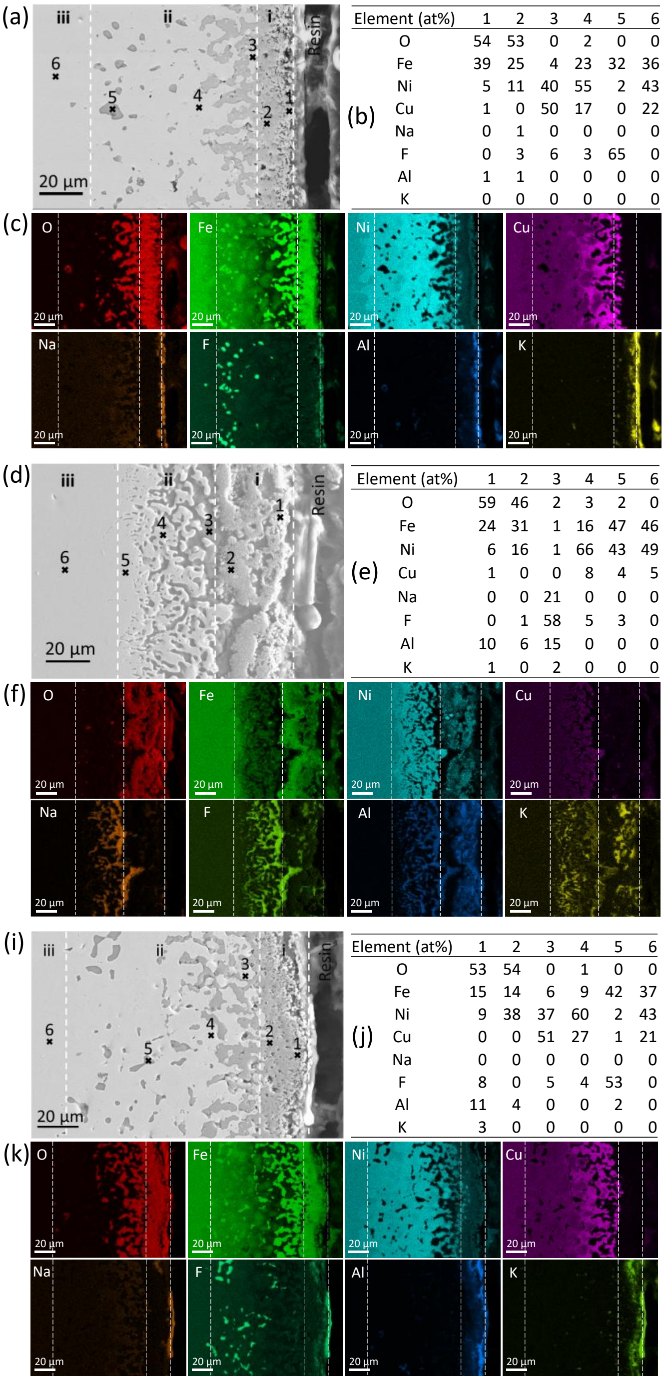

(b)

Element (at%)	1	2	3	4	5	6
O	54	53	0	2	0	0
Fe	39	25	4	23	32	36
Ni	5	11	40	55	2	43
Cu	1	0	50	17	0	22
Na	0	1	0	0	0	0
F	0	3	6	3	65	0
Al	1	1	0	0	0	0
K	0	0	0	0	0	0

(e)

Element (at%)	1	2	3	4	5	6
O	59	46	2	3	2	0
Fe	24	31	1	16	47	46
Ni	6	16	1	66	43	49
Cu	1	0	0	8	4	5
Na	0	0	21	0	0	0
F	0	1	58	5	3	0
Al	10	6	15	0	0	0
K	1	0	2	0	0	0

(j)

Element (at%)	1	2	3	4	5	6
O	53	54	0	1	0	0
Fe	15	14	6	9	42	37
Ni	9	38	37	60	2	43
Cu	0	0	51	27	1	21
Na	0	0	0	0	0	0
F	8	0	5	4	53	0
Al	11	4	0	0	2	0
K	3	0	0	0	0	0

Fig. 8. SEM and EDS analysis of the cross-section of Cu-Ni-Fe alloy anode from experiments 3 (a-c), 4 (d-f), and 5 (i-k), after electrolysis at 800 ^{o}C. The SEM images in (a), (d), and (i) show three distinct regions, namely i) oxide layer, ii) depletion region, and iii) base alloy. EDS point analyses for the designated zones (zone 1 to 6) within these SEM images are presented in (b), (e), and (j). EDS mapping of the SEM image, showing the distribution of O, Fe, Ni, Cu, Na, F, Al, and K elements, is presented in (c), (f), and (k).

In experiment 4, the SEM image of the oxide layer of the 5Cu-48Ni-47Fe wt% alloy anode revealed a porous, fractured, and delaminated morphology throughout the specimen, see Fig. 8. Due to the open form, the thickness measurements of the oxide layer and depletion region were approximate, i.e., 35-50 µm and 40-70 µm, respectively.

According to XRD results in Fig. 9, the oxide layer was most likely represented by Fe_2O_3 and $NiFe_2O_4$. EDS analysis in zone 1 and 2 confirmed the presence of a mixture of Fe_2O_3 and $NiFe_2O_4$, see Fig. 8(e). In particular, $NiFe_2O_4$ was found to be strongly detected in zone 2. However, EDS mapping (Na, F, Al, K) in Fig. 8 (f) clearly shows the electrolyte penetration across the oxide layer. During the pre-oxidation study of the alloy shown in Fig. 6, it was noted that the oxide layer formed after 8 h was relatively thin. A low percentage of Cu (5 wt%) in Cu-Ni-Fe alloy may affect the oxidation kinetics during electrolysis, potentially forming a discontinuous layer of $NiFe_2O_4$ oxide. According to Gavrilova,[12] $NiFe_2O_4$ spinel formation is critically affected by Cu wt% in the alloy.

Beneath the oxide layer (zone 3), the electrolyte was infiltrated due to porous oxide layer morphology. It might have accelerated the metal loss by fluoridization, as per reaction (7), and increased corrosion rate, leading to high contamination, as reported in Table 5. This also explains the rise in cell voltage observed after 2 h of electrolysis at a rate of 0.04 V h^{-1}, as seen in Fig. 7. Multiple authors have reported the presence of a layer of metallic fluorides (MF_x) beneath the oxide layer.[10,13,14,16] However, EDS and XRD analysis did not detect the presence of MF_x. This suggests that these fluorides might have formed but subsequently dissolved in the electrolyte or converted to more stable aluminates, especially in the absence of a protective oxide layer like $NiFe_2O_4$.

Additionally, some traces of copper-aluminate ($CuAl_2O_4$) were detected on the surface by XRD analysis. The formation of $CuAl_2O_4$ is thermodynamically favorable (negative ΔG_r^0) under high alumina activity but is, unfortunately, an insulator. The literature value of ΔG_r^0 for copper oxides and aluminates was subjected to discrepancies due to their complex nature.[35] Lorentsen[35] calculated the Gibbs free energy for $CuAl_2O_4$ formation experimentally and suggested a regression equation for reaction (14), which gives $\Delta G_r^0 = -64.31$ kJ mol^{-1} at 800 ^{0}C. Zone 4 of the depletion region was found to be enriched in Ni and Cu due to preferential depletion and oxidation of Fe element.

$$\mathrm{Cu}_{(s)} + \tfrac{1}{2}\mathrm{O}_{2\,(g)} + \mathrm{Al}_2\mathrm{O}_{3\,(diss.)} = \mathrm{CuAl}_2\mathrm{O}_{4\,(s)} \qquad (14)$$

In experiment 5, the 20Cu-42Ni-38Fe wt% alloy anode displayed similar oxide layer composition and phase distribution behavior as stated above in experiment 3. In Fig. 8(i), a dense and coherent oxide layer, measuring 23 µm in average thickness, was formed on the anode surface. The average thickness of the depletion region was about 85 µm. XRD and EDS analyses confirmed that the oxide layer primarily consists of Fe_2O_3 and $NiFe_2O_4$ as the major constituents. Remarkably, within the oxide/alloy interface (zone 2), an enrichment of Ni was detected. This observation suggests the presence of a semicontinuous layer of $Ni_xFe_{1-x}O$ spinel, as observed during the pre-oxidation of the alloy in Fig. 6.

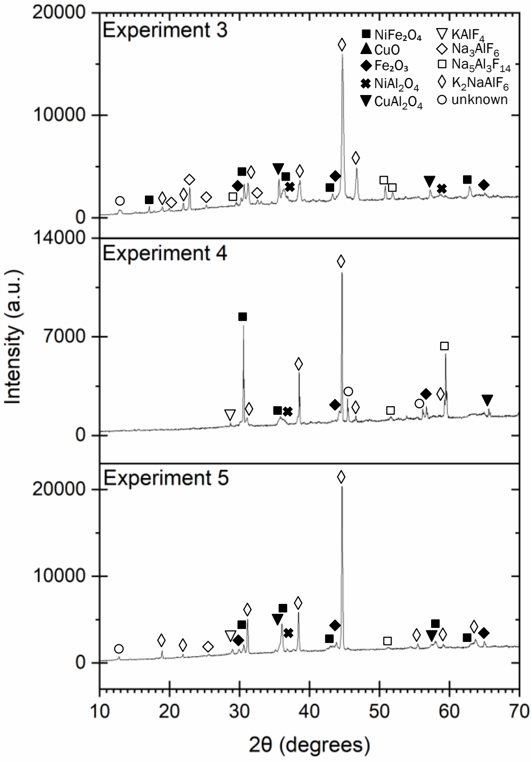

Fig. 9. XRD spectra of the active surface of the anode post-electrolysis: alloy 20Cu-42Ni-38Fe wt% in experiment 3; alloy 5Cu-48Ni-47Fe wt% in experiment 4; and alloy 20Cu-42Ni-38Fe wt% in experiment 5.

Influence of electrolyte composition on anode degradation behavior

There were significant differences between the morphology and phases of the oxide layer and the depletion region, as seen in Fig. 8. The oxide layer of 20Cu-42Ni-38Fe wt% alloy was relatively dense and coherent as compared to the oxide layer of the 5Cu-48Ni-47Fe wt% alloy. The major constituents of the protective oxide layer were Fe_2O_3 and $NiFe_2O_4$. The test results indicate that the 20Cu-42Ni-38Fe wt% alloy exhibited a relatively lower anode wear rate (see Table 5) and stable cell voltage evolution in the K-rich electrolyte (experiment 5) compared to Na-rich electrolyte (experiment 3).

Structures of ionic species and equilibrium reactions could explain why a Na-rich electrolyte is more corrosive for metallic anodes. In AF-AlF_3 (A = Na, K) melts, AlF_4^- and $AlF_5^{2-}$are dominating anions in low cryolite ratio AF/AlF_3 < 2 (mole ratios), and possible oxide complexes are according to reactions (15) and (16).[18] Alkali cations with smaller ionic radii exhibit a stronger ionic potential in A^+–F^- bond. This causes Na^+ cations to interact more strongly with F^- anions, including AlF_4^- and AlF_5^{2-}, than K^+. Thereby, replacing K^+ with

Na^+ will shift the equilibrium of reactions (15) and (16) to the left, leading to lower solubility of alumina in the Na-rich compared to the K-rich electrolyte.

$$\mathrm{Al_2O_3} + 4\mathrm{AlF_5^{2-}} = 3\mathrm{Al_2OF_6^{2-}} + 2\mathrm{F^-} \quad (15)$$

$$\mathrm{Al_2O_3} + \mathrm{AlF_5^{2-}} + \mathrm{F^-} = \frac{3}{2}\mathrm{Al_2O_2F_4^{2-}} \quad (16)$$

The reduced solubility of alumina in the electrolyte has the potential to accelerate the corrosion of metallic anodes due to several factors. Firstly, the driving force for alumina dissolution from the surface of the bath to the bulk is reduced; hence, it is challenging to operate near saturated alumina conditions. Secondly, an unsaturated bath accelerates the solubility of oxides and the rate of anodic dissolution.[35] Thirdly, the local depletion of alumina at the anode further lowers the alumina activity more significantly in Na-rich than in K-rich electrolytes. Consequently, the equilibrium of the oxide reaction (6) shifts towards the fluoride reaction (7), leading to an increased corrosion rate.

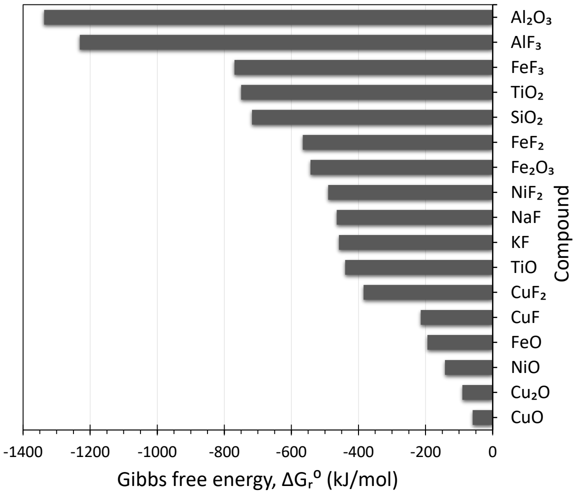

Fig. 10. Gibbs free energy of possible oxides and fluorides of Cu-Ni-Fe alloy anode and TiB_2 cathode in molten NaF-KF-AlF_3-Al_2O_3 electrolyte at 800 °C.

A list of possible oxide and fluoride compound formations in a molten electrolyte of NaF-KF-AlF_3-Al_2O_3 operating with a Cu-Ni-Fe anode and a TiB_2 cathode at 800 °C is presented in Fig. 10. Notably, ΔG_r^0 of formation is negative, and it shows a sequence of relative thermodynamic stability among compounds. Fluorides of anode constituents (Cu, Ni, and Fe) are more stable products compared to the corresponding oxides. Hence, it is vital to maintain a saturated bath condition with alumina, as this helps suppress the fluoridation reaction.

3.5 Conclusion

In this study, aluminum electrolysis with a Na-rich electrolyte composition, CR = 1.3 and KR = 0.3, was operated at 800 ^{0}C under stable 40 A laboratory cell conditions with one vertical cathode of TiB_2 in between two vertical single-phase anodes of homogenized Cu-Ni-Fe alloy of compositions 20Cu-42Ni-38Fe wt% and 5Cu-48Ni-47Fe wt%. A K-rich electrolyte composition with CR = 1.3 and KR = 0.8 was also evaluated for comparison.

This study investigated in detail the composition of the oxide layer on the Cu-Ni-Fe alloy, formed through pre-oxidation at 800 ^{0}C in air. The assessment primarily focused on examining the impact of the alloy composition, specifically the Cu wt%, on the morphology of the oxide scale. It was found that 20Cu-42Ni-38Fe wt% alloy developed multi-layered Cu and Fe-rich oxide phases containing CuO, Fe_2O_3, and $NiFe_2O_4$ as major constituents. Conversely, 5Cu-48Ni-47Fe wt% alloy produced Fe-rich oxide phases. The alloy with a higher Cu wt% displayed the formation of dense, defect-free, multi-layered oxide, along with increased Cu outward diffusion and the presence of distinctive intermediate oxide layers ($Cu_xFe_{3-x}O_4$ and $Ni_xFe_{1-x}O$). The successful formation of a protective $NiFe_2O_4$ oxide layer through the pre-oxidation treatment confirms the effectiveness of the treatment in meeting the requirement for an inert anode alloy.

The evaluation of Cu-Ni-Fe alloys in aluminum electrolysis experiments yielded low and stable cell voltages. The combination of a low-temperature electrolyte and an inert anode alloy is anticipated to result in improved alumina solubility of the bath, a reduced wear rate of anode, and the formation of a compact $NiFe_2O_4$ oxide on the surface via anodic reactions. Based on these criteria, the use of a K-rich electrolyte and the 20Cu-42Ni-38Fe wt% alloy shows significant potential. Post-electrolysis analysis revealed that the 20Cu-42Ni-38Fe wt% anode was protected by a denser and coherent multi-layered oxide formation compared to the 5Cu-48Ni-47Fe wt%. Moreover, it was found that an electrolyte composition with low alumina solubility (high activity of AlF_3) could potentially be more corrosive for metallic anodes.

The electrolysis experiment, with abrupt changes in bath temperature and current density within defined limits, showed remarkable stability. This suggests the potential use of a full-size cell (100 kA or more) for smart grid technology. These findings could be encouraging, but they need to be further investigated in long-term electrolysis.

Acknowledgments

This work is supported by the Icelandic Research Fund (project 207242051), and the Landsvirkjun Energy Research Fund (project NYR-11-2021). Support for chemical analysis of electrolyte and produced aluminum samples by Trimet Aluminium in Germany is gratefully acknowledged.

References

[1] C.M. Hall, Process of reducing aluminium by electrolysis, Patent US400766A, 1889.

[2] T.R. Beck, Production of Aluminum with Low Temperature Fluoride Melts, in: G. Bearne, M. Dupuis, G. Tarcy (Eds.), Essential Readings in Light Metals: Volume 2 Aluminum Reduction Technology, Springer International Publishing, Cham, 2016: pp. 89–95.

[3] T.R. Beck, A Non-Consumable Metal Anode for Production of Aluminum with Low-Temperature Fluoride Melts, Essential Readings in Light Metals: Volume 4 Electrode Technology for Aluminum Production. 4 (2016) 1104–1109.

[4] T.R. Beck, Aluminum production cell, Patent US8480876B2, 2013.

[5] G. Gunnarsson, G. Óskarsdóttir, S. Frostason, J.H. Magnússon, Aluminum Electrolysis with Multiple Vertical Non-consumable Electrodes in a Low Temperature Electrolyte, Light Metals 2019. (2019) 803–810.

[6] S.K. Padamata, K. Singh, G.M. Haarberg, G. Saevarsdottir, Review—Primary Production of Aluminium with Oxygen Evolving Anodes, J. Electrochem. Soc. 170 (2023) 073501.

[7] J. Thonstad, P. Fellner, G.M. Haarberg, J. Hives, H. Kvande, A. Sterten, Aluminium Electrolysis: Fundamentals of the Hall-Héroult Process, Beuth Verlag GmbH, 2011.

[8] International Aluminium Institute UK, 1.5 Degrees Scenario: A Model To Drive Emissions Reduction, (n.d.). https://international-aluminium.org/resource/1-5-degrees-scenario-a-model-to-drive-emissions-reduction/ (accessed May 10, 2022).

[9] G. Saevarsdottir, H. Kvande, B.J. Welch, Aluminum Production in the Times of Climate Change: The Global Challenge to Reduce the Carbon Footprint and Prevent Carbon Leakage, JOM. 72 (2020) 1422–1422.

[10] I. Gallino, M.E. Kassner, R. Busch, Oxidation and corrosion of highly alloyed Cu–Fe–Ni as inert anode material for aluminum electrowinning in as-cast and homogenized conditions, Corrosion Science. 63 (2012) 293–303.

[11] S. Helle, M. Pedron, B. Assouli, B. Davis, D. Guay, L. Roué, Structure and high-temperature oxidation behaviour of Cu–Ni–Fe alloys prepared by high-energy ball milling for application as inert anodes in aluminium electrolysis, Corrosion Science. 52 (2010) 3348–3355.

[12] E. Gavrilova, G. Goupil, B. Davis, D. Guay, L. Roué, On the key role of Cu on the oxidation behavior of Cu–Ni–Fe based anodes for Al electrolysis, Corrosion Science. 101 (2015) 105–113.

[13] T.R. Beck, C.M. Macrae, N.C. Wilson, Metal Anode Performance in Low-Temperature Electrolytes for Aluminum Production, Metall Mater Trans B. 42 (2011) 807–813.

[14] L. Ying, C. Dengpeng, W. Wei, L. Dongsheng, W. Junwei, L. Yudong, S. Zhirong, Influences of heat treatment on the oxidation and corrosion behavior of Cu–Ni–Fe inert anodes for aluminium electrolysis, Journal of Alloys and Compounds. 832 (2020) 154848.

[15] T.T. Nguyen, Metallic oxygen evolving anode operating at high current density for aluminium reduction cells, Patent EP2324142B1, 2012.

[16] V. Chapman, B.J. Welch, M. Skyllas-Kazacos, Anodic behaviour of oxidised Ni–Fe alloys in cryolite–alumina melts, Electrochimica Acta. 56 (2011) 1227–1238.

[17] J. Thonstad, S. Rolseth, Alternative electrolyte compositions for aluminium electrolysis, Mineral Processing and Extractive Metallurgy. 114 (2005) 188–191.

[18] E. Robert, J.E. Olsen, V. Danek, E. Tixhon, T. Østvold, B. Gilbert, Structure and Thermodynamics of Alkali Fluoride−Aluminum Fluoride−Alumina Melts. Vapor Pressure, Solubility, and Raman Spectroscopic Studies, J. Phys. Chem. B. 101 (1997) 9447–9457.

[19] A. Apisarov, A. Dedyukhin, O. Tkacheva, E. Nikolaeva, Y. Zaikov, P. Tinghaev, Physical-chemical properties of the KF-NAF-ALF3 molten system with low cryolite ratio, TMS Annual Meeting. (2009) 401–403.

[20] I. Gallino, Phase diagram, thermal stability, and high temperature oxidation of the ternary Cu-Ni-Fe system, PhD thesis, Oregon State University, 2004.

[21] D.A. Weirauch Jr, W.J. Krafick, G. Ackart, P.D. Ownby, The wettability of titanium diboride by molten aluminum drops, Journal of Materials Science. 40 (2005) 2301–2306.

[22] E. Kubiňáková, M. Benköová, P. Veteška, Ľ. Bača, J. Híveš, Surface characterisation and wettability of titanium diboride by aluminium at low temperature, Advances in Applied Ceramics. 119 (2020) 22–28.

[23] A. Apisarov, A. Dedyukhin, E. Nikolaeva, P. Tinghaev, O. Tkacheva, Y. Zaikov, Liquidus Temperatures of Cryolite Melts With Low Cryolite Ratio, Metallurgical and Materials Transactions B. 42 (2010) 236–242.

[24] A. Dedyukhin, A. Kataev, Density and molar volume of KF-NaF-AlF3 Melts with Al2O3 and CaF2 additions, ECS Transactions. 64 (2014).

[25] A. Roine, HSC Chemistry Software, Version 9.9.2.3, Metso Outotec, Pori, Finland, (2017). www.mogroup.com/hsc.

[26] X. Cheng, L. Fan, H. Yin, L. Liu, K. Du, D. Wang, High-temperature oxidation behavior of Ni-11Fe-10Cu alloy: Growth of a protective oxide scale, Corrosion Science. 112 (2016) 54–62.

[27] V. Chapman, B.J. Welch, M. Skyllas-Kazacos, High temperature oxidation behaviour of Ni–Fe–Co anodes for aluminium electrolysis, Corrosion Science. 53 (2011) 2815–2825.

[28] R. Haugsrud, T. Norby, P. Kofstad, High-temperature oxidation of Cu–30 wt.% Ni–15 wt.% Fe, Corrosion Science. 43 (2001) 283–299.

[29] F. Gesmundo, Y. Niu, D. Oquab, C. Roos, B. Pieraggi, F. Viani, The Air Oxidation of Two-Phase Fe-Cu Alloys at 600-800°C, Oxidation of Metals. 49 (1998) 115–146.

[30] G. Goupil, E. Gavrilova, B. Davis, D. Guay, L. Roué, Evaluation of a Pre-Oxidation Treatment for Limiting Electrolyte Penetration in Cu-Ni-Fe Anode during Al Electrolysis, in: TMS Light Metals, 2014: pp. 1305–1307.

[31] M. Alzamani, K. Jafarzadeh, The Effect of Pre-oxidation Treatment on Corrosion Behavior of Ni–Cu–Fe–Al Anode in Molten CaCl2 Salt, Oxid Met. 89 (2018) 623–640.

[32] P. Cui, A. Solheim, G.M. Haarberg, The Performance of Aluminium Electrolysis in a Low Temperature Electrolyte System, in: E. Williams (Ed.), Light Metals 2016, Springer International Publishing, Cham, 2016: pp. 383–387.

[33] S. Bao, D. Chai, Z. Shi, J. Wang, G. Liang, Y. Zhang, Effects of Current Density on Current Efficiency in Low Temperature Electrolysis with Vertical Electrode Structure, Light Metals 2018. (2018) 611–619.

[34] A.V. Suzdaltsev, A.Y. Nikolaev, Y.P. Zaikov, Towards the Stability of Low-Temperature Aluminum Electrolysis, Journal of the Electrochemical Society. 168 (2021) 46521-.

[35] O.-A. Lorentsen, Behaviour of nickel, iron and copper by application of inert anodes in aluminium production, PhD thesis, Norwegian University of Science and Technology, 2000.

[36] E. Olsen, J. Thonstad, The Behaviour of Nickel Ferrite Cermet Materials as Inert Anodes, in: A. Tomsett, J. Johnson (Eds.), Essential Readings in Light Metals: Volume 4 Electrode Technology for Aluminum Production, Springer International Publishing, Cham, 2016: pp. 1110–1118.

[37] A. Apisarov, J. Barreiro, A. Dedyukhin, L. Galán, A. Redkin, O. Tkacheva, Y. Zaikov, Reduction of the Operating Temperature of Aluminium Electrolysis: Low-Temperature Electrolyte, Light Metals 2012. (2012) 783–786.

[38] T. Jentoftsen, O.-A. Lorentsen, E. Dewing, G.M. Haarberg, J. Thonstad, Solubility of some transition metal oxides in cryolite-alumina melts: Part I. Solubility of FeO, FeAl2O4, NiO, and NiAl2O4, Metallurgical and Materials Transactions B. 33 (2002) 901–908.

[39] A. Solheim, A. Sterten, Activity of Alumina in the System NaF-AlF3-Al2O3 at NaF/AlF3 Molar Ratios Ranging from 1.4 to 3, Light Metals 1999. (1999) 445–452.

Chapter 4

Overpotential on Oxygen Evolving Platinum and Ni–Fe–Cu Anode for Low Temperature Molten Fluoride Electrolytes

Kamaljeet Singh[1,2,*], Geir Martin Haarberg[2], Abdul Rahman Mallah[1], Gudmundur Gunnarsson[3], Thomas Luke Jamieson[4], Isabella Gallino[4,5], Gudrun Saevarsdottir[1,2]

[1]Department of Engineering, Reykjavik University, 102 Reykjavik, Iceland
[2]Department of Materials Science and Engineering, NTNU, 7491 Trondheim, Norway
[3]Taeknisetur IceTec, Arleynir 8, 112 Reykjavik, Iceland
[4]Chair of Metallic Materials, Saarland University, 66123 Saarbrucken, Germany
[5]Department of Materials Science and Engineering, TU-Berlin, 10587 Berlin, Germany
*Corresponding author: kamaljeets@ru.is

4.1 Abstract

To eliminate climate gas emissions from aluminum electrolysis, modifying the cryolite-based electrolyte by partly replacing Na with K reduces liquidus, allowing a process temperature of 800 ^{0}C. This enables the use of various metallic alloys for oxygen evolving inert anode technology. This alternative process requires higher energy efficiency to compensate for the increased reaction voltage, which highlights the importance of evaluating kinetics and overpotential on the oxygen evolving anode. This study evaluates anodic overpotentials using steady state polarization on platinum and three Ni–Fe–Cu-based alloy compositions in $\mathrm{KF-NaF-AlF_3-Al_2O_{3(sat.)}}$ electrolyte at 800 ^{0}C. The polarization curve on the platinum anode reveals two linear Tafel regions, while Ni–Fe–Cu anodes exhibit a single Tafel region. Notably, Ni–Fe–Cu anodes treated with high temperature air oxidation to develop a pre-formed oxide layer exhibit better electrocatalytic activity than untreated anodes of the corresponding composition.

The kinetic equations, based on a theoretical model for the proposed mechanism of the oxygen evolution reaction, are derived and utilized to simulate overpotential and current, taking into account surface coverage. This model accurately predicts the experimentally observed two Tafel regions on the platinum anode, indicating a charge transfer mechanism controlled by either a single-step or two-step process. We illustrate that multiple Tafel slopes can be attributed to the potential dependent surface coverage of the adsorbate and can be correlated with a particular rate-determining step.

4.2 Introduction

Harnessing a greater proportion of renewable energy to power primary metal production is necessary to tackle the climate crisis of the 21st century.[1–3] In this regard, high temperature molten salt electrolysis processes significantly contribute to modern society through efficient electrometallurgy and energy conversion with favorable reaction kinetics.[1,4] The Hall-Héroult (H-H) process is currently the only industrial method for primary aluminum production. It is based on the electrodeposition in a molten cryolite-based electrolyte according to Eq. (1); and aluminum is a crucial material (67 million tonnes production in 2021[5]) in the modern engineering industry, encompassing construction, aerospace, automobile, and packaging sectors.[1,4] However, the H-H process emits an average of 15.8 kg $\mathrm{CO_{2e}}$ and demands 14.2 kWh of energy per kilogram of aluminum.[5]

$$\frac{1}{2}\mathrm{Al_2O_{3(diss.)}}+\frac{3}{4}\mathrm{C_{(s)}}\xrightarrow[\mathrm{NaF\cdot AlF_{3(l)}}]{\mathrm{E^{rev}\ at\ 966^0C=1.19V}}\mathrm{Al_{(l)}}+\frac{3}{4}\mathrm{CO_{2(g)}} \qquad (1)$$

To mitigate direct $\mathrm{CO_{2(g)}}$ emissions in addition to intermittent perfluorocarbons release during the ‘anode effect’ from the H-H process, inert anode technology (IAT) can offer a sustainable solution for future primary aluminum production with $\mathrm{O_{2(g)}}$ as an anode product, according to Eq. (2).[1,2,4] However, the necessary criteria for a suitable inert anode material include maintaining both chemical and electrochemical stability against oxidation from anodic reactions and fluoridation in a molten fluoride bath, a condition not yet met on an industrial scale.[2,6]

$$\frac{1}{2}\mathrm{Al_2O_{3(diss.)}} \xrightarrow[\mathrm{KF{\cdot}NaF{\cdot}AlF_{3(l)}}]{\mathrm{E^{rev}at\ 800^0C=2.31V}} \mathrm{Al_{(l)}} + \frac{3}{4}\mathrm{O_{2(g)}} \quad (2)$$

In terms of energy usage, using IAT indicates higher energy consumption due to the absence of the chemical energy of carbon and the increased Gibbs free energy when operating at a lower bath temperature (800 ^{0}C) to reduce corrosion of metal electrodes. For example, there is an increase of 1.12 V in the reversible potential ($\mathrm{E^{rev}}$) of Eq. (2) at 800 ^{0}C compared to Eq. (1) at 966 ^{0}C.[7] Despite this, the idea of IAT remains attractive owing to the ever increasing electricity generated from renewable energy sources.[1,3]

The anode reaction of aluminum electrolysis in the H-H process is associated with a notable overpotential, typically about 0.76 V[8] at a normal current density ($\mathrm{I_n}$) of 0.8 A cm^{-2}, primarily attributable to the complex kinetically sluggish $4\mathrm{e^-}$ transfer process as per Eq. (3).[4]

$$\mathrm{C_{(s)}} + 2\mathrm{O^{2-}} \rightarrow \mathrm{CO_{2(g)}} + 4\mathrm{e^-} \quad (3)$$

Using an inert metallic anode, as suggested by Beck [9], may yield faster kinetics and reduced anodic overpotentials as per Eq. (4) compared to carbon anode in the H-H process, potentially offsetting the increased $\mathrm{E^{rev}}$ in IAT.

$$\mathrm{M_{(s)}} + 2\mathrm{O^{2-}} \rightarrow \mathrm{M_{(s)}} + \mathrm{O_{2(g)}} + 4\mathrm{e^-} \quad (4)$$

where M represents an inert metallic anode.

If the metallic anode (M) is inert, $\mathrm{O_{2(g)}}$ evolution as per Eq. (4) occurs independently without M. Otherwise, the metal undergoes oxidation at the anode surface, as per Eq. (5). This consideration leads to the strategic use of economically viable transition metal alloys of Fe, Ni, and Cu to form protective oxides through Eq. (5), with $NiFe_2O_4$ being particularly desirable due to its low solubility in the cryolite bath and reasonable electrical conductivity.[6] Moreover, a pre-formed oxide layer of $NiFe_2O_4$, through surface treatment, tends to improve the alloy stability.[10–12]

$$\mathrm{M_{(s)}} + \mathrm{O^{2-}} \rightarrow \mathrm{MO_{(s)}} + 2\mathrm{e^-} \quad (5)$$

The existing literature extensively covers the kinetics of anodic reactions and overpotential studies, particularly on carbon and graphite anodes.[4] This emphasis is expected, given their significant importance in the conventional H-H process. However, the published data on metallic anodes, notably platinum and Ni–Fe–Cu-based alloys, in low temperature $\mathrm{KF - NaF - AlF_3}$ electrolyte is scarce, considering it is a new system.

The kinetic mechanism of oxygen evolution reaction (OER) in molten salts was established long ago through the foundational work of numerous authors cited in the references[13–16] and many others.[4,17,18] Particularly for cryolite melts, the OER mechanism was proposed by Thonstad[15] based on the framework of Vetter.[14] According to this model, the identification of the rate determining step (RDS) is based on the Butler-Volmer theory, relying on simplified assumptions regarding the exchange current density and the surface coverage for the adsorbed intermediate being set at either 0 or 1.[14,15] This approach effectively handles complex rate expressions and elucidates the experimentally observed two Tafel regions. However, the limitation emerges when simplifying rate expressions.

Recent developments in electrocatalysts for $\mathrm{H_{2(g)}}$ and $\mathrm{O_{2(g)}}$ evolution reactions in water electrolysis, like hydrogen production and electrolysis, lead to a thoughtful consideration of the suitability of the Butler-Volmer theory for predicting the RDS. [19–22] Two main reasons contribute to this uncertainty: (i) it does not account for surface coverage (θ) whereas Tafel slopes are coverage dependent, and (ii) it is derived for simple reaction ($\mathrm{O} + \mathrm{e}^- \rightleftarrows \mathrm{R}$), overlooking the complexities of multi-step, multiple-electron transfer reactions with intermediate adsorption. [19–22]

Considering these advancements, we have re-examined the OER mechanism in molten fluoride electrolytes, focusing on the three main objectives outlined in this report. Firstly, systematically measuring anodic overpotentials by steady state polarization on platinum and Ni–Fe–Cu-based alloys in $\mathrm{KF-NaF-AlF_3-Al_2O_{3(sat.)}}$ electrolyte at 800 $^{\mathrm{o}}$C. Secondly, developing a theoretical model based on kinetic equations for the proposed OER mechanism, incorporating surface coverage (θ). Thirdly, confirming the model's accuracy in identifying the specific RDS by comparing experimental results from this study in addition to several literature examples in conventional cryolite-based electrolytes.

For the choice of Ni–Fe–Cu alloys, three compositions, single-phase (γ-fcc) and homogenized, were evaluated. These alloys were selected because they maintain a single-phase outside the miscibility gap at an operating temperature of 800 $^{\mathrm{o}}$C.[23,24] The selected low temperature ternary electrolyte composition of $\mathrm{KF-NaF-AlF_3}$ electrolyte, $\mathrm{CR} = (\mathrm{KF}+\mathrm{NaF})/(\mathrm{AlF_3}) = 1.3$ and $\mathrm{KR} = (\mathrm{KF})/(\mathrm{KF}+\mathrm{NaF}) = 0.3$ (in mole ratios), is advantageous for its physicochemical properties compared with binary KF-$\mathrm{AlF_3}$ based electrolyte. For example, better electrical conductivity and low melting point [25–27]- but poses challenges in terms of lower alumina solubility (about 4.0 wt.%) and increased anode wear rate.[25,12] The Na content also facilitates the adoption of industrial electrolysis, addressing Na impurities introduced from the alumina feed, gradually transitioning the $\mathrm{KF-AlF_3}$ system to $\mathrm{KF-NaF-AlF_3}$ over time.

4.3 Experimental

Platinum and Ni–Fe–Cu anode

Platinum wire of purity 99.99 wt.% (Goodfellow UK) with a diameter of 0.5 to 1 mm was used as anode.

Three compositions of Ni–Fe–Cu alloy as anode were evaluated. The alloys Ni60-Fe30-Cu10 and Ni42-Fe38-Cu20 (in wt.%) were cast and homogenized to a single-phase. They were annealed at 1100 $^{\mathrm{o}}$C for 12 h in a vacuum furnace.[23] The third composition, Ni48-Fe47-Cu5 (in wt.%), is a commercial, hot-rolled, single-phase alloy.

The Ni42-Fe38-Cu20 and Ni48-Fe47-Cu5 alloys were provided as 12 mm thick plates, from which diameter 5 mm rods of length 40 mm were machined. In contrast, the Ni60-Fe30-Cu10 alloy was directly casted from pure metals (purity >99.97 wt.%) to a diameter of 5 mm rod. Next, the diameter of rods was machined down to 2 mm at one end for a length of 15 mm, and then the surface was polished using 500-grit abrasive paper. Subsequently, the rods were degreased in ethanol, cleaned ultrasonically in distilled water, and dried prior to usage.

To pre-form a surface oxide layer on Ni–Fe–Cu-based alloy, the oxidation treatment was carried out in a muffle furnace at 800 ^{o}C in air for 8 h. For electrical connection, the alloy anode was connected to a stainless-steel connector rod of 3 mm diameter, shielded inside an alumina tube, using a threaded joint. The anode was placed at a depth of 5-10 mm into the bath, with the exact depth confirmed post-run. To minimize the degradation of the anode in the fluoride melt, it was lowered into the bath under anodic polarization. This practice was found to be essential for ensuring anode stability during electrochemical measurements.

Cell setup

A graphite crucible (inner diameter 76 mm and depth 110 mm, Schunk SE Sweden) containing about 350 g of $\mathrm{KF:NaF:AlF_3}$ mixture in wt.% ratio 15.7:26.3:58 was used as molten fluoride electrolyte, which gave CR = 1.3 and KR = 0.3. About 6 wt.% of alumina was included in the initial mixture, and a 5 mm thick alumina side lining was added to the crucible to ensure bath saturation. The crucible was placed in an externally heated vertical tube furnace (Entech AB Sweden) in an inert $\mathrm{N_{2(g)}}$ (purity >99.999 vol.%) atmosphere, controlled programmatically to ensure uniform heating, with water-cooled upper and bottom flanges. The cell was operated at a bath temperature (T) of 800 ^{o}C. To eliminate impurities, pre-electrolysis was conducted with diameter 8 mm graphite electrodes at a constant potential of 1.8 V for 2 h.

The salts used, including KF (purity 99.99 wt.%), NaF (purity 99.9 wt.%), and Al_2O_3 (purity 99.5 wt.%), were supplied by Carl Roth Germany, while AlF_3 (sublimed) was synthesized by sublimation at SINTEF Norway. All compounds were dried at 300 ^{o}C for a minimum of 24 h, weighed to required quantity, and mixed in a close lid container.

The reference electrode was molten aluminum (0.8 g, purity >99.998 wt.%) in a close end alumina tube, with an outer diameter of 8.5 mm, filled with 1 g of aforementioned $\mathrm{KF-NaF-AlF_3-Al_2O_3}$ mixture, featuring a small opening to contact with the bath. The molten aluminum was in contact with a 1 mm diameter tungsten wire shielded inside an alumina tube. The counter electrode was the graphite crucible itself.

Overpotential test

The overpotential was measured by steady state polarization using a potentiostat (Ivium XP40 Netherlands). The potential steps were 10–15 mV for lower overpotentials and ranged between 30–100 mV for higher overpotentials, with each step lasting 15–20 s. Potentials were applied in descending order, from higher to lower values. AC impedance spectroscopy was conducted to determine the ohmic drop (iR). Measurements were taken over a frequency range of 100 Hz to 100 kHz, using an AC amplitude of 15 mV.

4.4 Results

Platinum anode

The open circuit potential was not stable for both platinum and Ni–Fe–Cu anodes. Therefore, lower overpotential measurements were restricted to an anode current density up to 0.02 A cm^{-2} for platinum and 0.02–0.04 A cm^{-2} for Ni–Fe–Cu anodes. The anodic overpotential (η) according to Eq. (6) was computed from the difference in anode potential ($\mathrm{E_{anode}}$) and reversible potential ($\mathrm{E_{anode}^{rev}}$= 2.31 V at 800 ^{o}C [7]), and corrected for ohmic drop (iR) as determined by AC impedance spectroscopy. The Tafel plots of the overpotential and the semi-logarithmic current density were obtained for a minimum of three independent experiments, as shown in Fig. 1. The accuracy of the overpotential measurement is about ±5 mV at lower potentials, and ±10 mV at higher overpotentials where $\mathrm{O_{2(g)}}$ bubbles induced fluctuations are apparently significant.

$$\eta = \mathrm{E_{anode}} - \mathrm{E_{anode}^{rev}} \qquad (6)$$

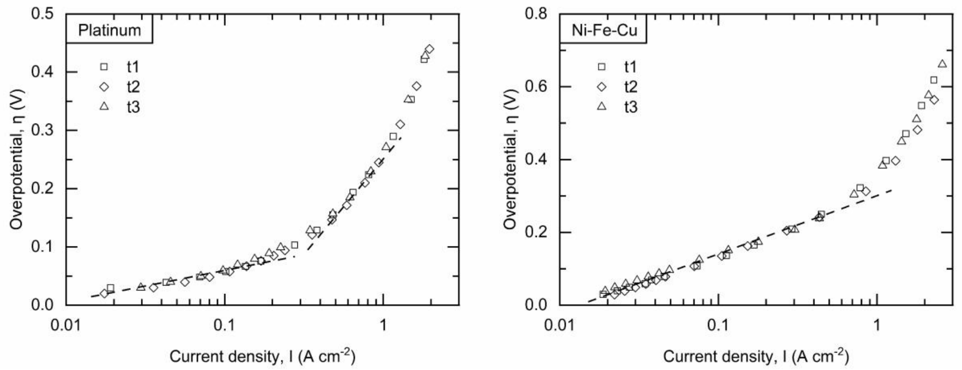

Fig. 1. Steady state polarization curve for three independent tests run t1, t2, and t3 on platinum and Ni42-Fe38-Cu20 anode (oxidized, polarized 0h); $\mathrm{KF-NaF-AlF_3-Al_2O_{3(sat.)}}$ electrolyte, CR = 1.3 and KR = 0.3; T = 800 ^{o}C. The dotted line shows the linear regression analysis.

As shown in Fig. 1, two distinct linear regions of the curve appear and are expressed as the Tafel equation: $\eta = \mathrm{a} + \mathrm{b}\log(\mathrm{I})$, where a is the intercept (V), b is the slope (V dec^{-1}), and I is the current density (A cm^{-2}). The average value of slope for linear regression analysis in the lower segment of current density (0.02–0.28 A cm^{-2}) ranged from 0.07 to 0.09 V dec^{-1}, as indicated by Eq. (7). Similarly, for the higher segment (0.40–0.90 A cm^{-2}) the slope was found to be between 0.25 and 0.27 V dec^{-1}, as represented by Eq. (8).

$$\eta = 0.12 + 0.07\log(\mathrm{I}) \quad (7)$$

$$\eta = 0.23 + 0.26\log(\mathrm{I}) \quad (8)$$

Ni–Fe–Cu anode

Steady state polarization curves were obtained for two surface modifications of the Ni–Fe–Cu anode: (i) oxidized (treated to have a pre-formed oxide layer), and (ii) untreated (without surface treatment). Within each category, measurements were conducted under two electrochemical conditions: (i) polarization 0 h (with no prior electrolysis), and (ii) polarization 1 h (under electrolysis conditions at I = 0.8 A cm^{-2} for 1 h before testing).

Repeated measurements for a minimum of three times showed good reproducibility for oxidized Ni–Fe–Cu anode of about ±10 mV at lower potentials and ±25 mV at higher overpotentials, as shown in Fig. 1. However, data for untreated Ni–Fe–Cu anode was scattered, and the accuracy of measurement was about ±35 mV or even larger in some cases. Potential sources of variations could arise from changes in coverage and resistance conditions at the electrode/melt interface.

The typical Tafel curves obtained are presented in Fig. 2, and the Tafel coefficients obtained through regression analysis are computed in Table 1. As illustrated in Fig. 2, the Tafel curve showed a single linear region followed by a marked upward trend at higher overpotentials. The bending of the Tafel line indicates a diffusion limitation. Thonstad et al. observed a similar phenomenon, where the bending of the Tafel curve disappeared when the melt was stirred, facilitating the easier transport of oxygen species.[28]

For the purpose of comparing the behavior of oxidized and untreated anodes, it is interesting to analyze the change in cell voltage evolution during electrolysis (polarization 1 h) in Fig. 2 (inset plots). Typically for untreated anodes, the cell voltage was not steady and found to increase with electrolysis time, except for Ni-rich anode composition of Ni60-Fe30-Cu10, which followed the reverse trend. Perhaps this non-steady behavior might indicate that the oxide growth rate exceeds the dissolution rate, resulting in a thicker layer and a gradual increase in voltage.

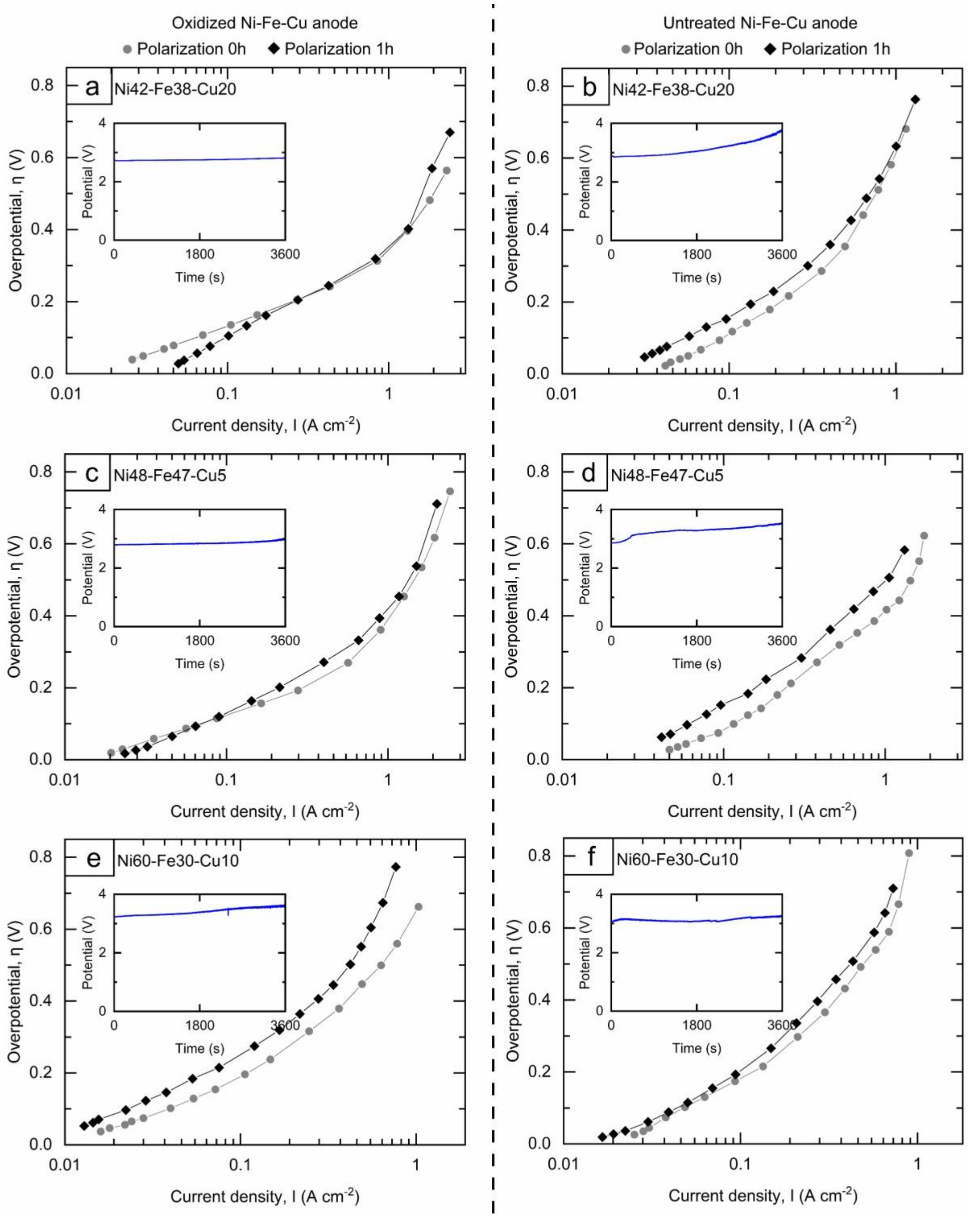

Fig. 2. Typical steady state anodic polarization curves for Ni–Fe–Cu-based anodes as a function of composition (in wt.%); $\mathrm{KF}-\mathrm{NaF}-\mathrm{AlF}_3-\mathrm{Al}_2\mathrm{O}_{3(\mathrm{sat.})}$ electrolyte, CR = 1.3 and KR = 0.3; T = 800 $^{\mathrm{o}}$C; potential *versus* aluminum reference electrode. Left plots (a, c, and e) represent oxidized anodes, and right plots (b, d, and f) correspond to untreated anodes. Polarization 0 h indicates no electrolysis prior to testing, whereas polarization 1 h means electrolysis at I = 0.8 A cm^{-2} for 1 h (inset plot) before testing.

Table 1. Tafel slope (b) and intercept (a) obtained from Tafel plots of Ni–Fe–Cu anodes in Fig. 2; $KF - NaF - AlF_3 - Al_2O_{3(sat.)}$ electrolyte, CR = 1.3 and KR = 0.3; T = 800 ^oC.

Ni–Fe–Cu anode (wt.%)	Anode surface treatment (—)	Electrochemical condition (—)	Tafel slope, $\mathbf{b}$ (V dec^{-1})	Tafel intercept, $\mathbf{a}$ (V)	Linear region (A cm^{-2})	R^2 value (—)
Ni42-Fe38-Cu20	Oxidized	Polarization 0 h	0.17	0.31	0.03–0.85	0.99
		Polarization 1 h	0.23	0.33	0.04–0.83	0.98
	Untreated	Polarization 0 h	0.30	0.42	0.04–0.64	0.97
		Polarization 1 h	0.31	0.49	0.03–0.67	0.97
Ni48-Fe47-Cu5	Oxidized	Polarization 0 h	0.18	0.33	0.02–0.90	0.97
		Polarization 1 h	0.25	0.39	0.02–0.89	0.98
	Untreated	Polarization 0 h	0.27	0.38	0.02–0.69	0.98
		Polarization 1 h	0.30	0.46	0.04–0.74	0.98
Ni60-Fe30-Cu10	Oxidized	Polarization 0 h	0.31	0.53	0.02–0.63	0.97
		Polarization 1 h	0.30	0.59	0.04–0.55	0.96
	Untreated	Polarization 0 h	0.39	0.62	0.02–0.78	0.97
		Polarization 1 h	0.35	0.60	0.02–0.65	0.96

4.5 Discussion

Theoretical analysis

According to the literature, the mechanism for oxygen evolution in molten salts can be described by four elementary steps organized into two proposed mechanisms: Mechanism-I involves Eqs. (9), (10), and (11), and Mechanism-II involves Eqs. (9) and (12).[14–16]

Step (i) $$M + O^{2-} \rightleftharpoons M - O_{(ad)} + 2e^- \quad (9)$$

Step (ii) $$M - O_{(ad)} + O^{2-} \rightleftharpoons M - O_{2(ad)} + 2e^- \quad (10)$$

Step (iii) $$M - O_{2(ad)} \rightleftharpoons M + O_{2(g)} \quad (11)$$

Step (iv) $$2(M - O_{(ad)}) \rightleftharpoons 2M + O_{2(g)} \quad (12)$$

Theoretical treatments for each step have been established through a mathematical model (refer to supplementary material), exploring the possibility of each step in Eqs. (9) to (12) as the RDS, and resulting in the derivation of four distinct current expressions given in Eqs.(13) to (16), respectively.[29]

$$i = nFA\, k_1^+ \, a_{O^{2-}} \exp\{2(1-\alpha_1)f\eta_1\} \quad (13)$$

$$i = nFA \frac{K_1\, k_2^+\, a_{O^{2-}}^2 \exp(2f\eta_1) \exp\{2(1-\alpha_2)f\eta_2\}}{1 + K_1\, a_{O^{2-}} \exp(2f\eta_1)} \quad (14)$$

$$i = nFA\,\overrightarrow{K_3^+}\;\frac{K_1\,K_2\,a_{O^{2-}}^2\,\exp\{2f(\eta_1+\eta_2)\}}{1 + K_1 a_{O^{2-}}\,\exp(2f\eta_1) + K_1\,K_2\,a_{O^{2-}}^2 \exp\{2f(\eta_1+\eta_2)\}} \tag{15}$$

$$i = nFA\,\overrightarrow{K_4^+}\;\left\{\frac{K_1\,a_{O^{2-}}\,\exp(2f\eta_1)}{1 + K_1\,a_{O^{2-}}\,\exp(2f\eta_1)}\right\}^2 \tag{16}$$

where i represents the current, n is the total number of electron transfers, A the area of the electrode, α_i the symmetry coefficient, η_i the overpotential, the terms k_i and K_i (defined as $\frac{k_i^+}{k_i^-}$) correspond to the standard rate constant and the ratio of standard rate constants, respectively, for i^{th} equation, f is defined as F/RT, where F, R, and T take their usual meanings, while θ_0, θ_1 and θ_2 represent the surface coverage of vacant site M, M-$O_{(ad)}$ and M-$O_{2(ad)}$, respectively.

Simulated Tafel plots

Based on Eqs. (13), (14), (15) and (16), Tafel plot simulations can be attempted for overpotential (η) *versus* semi-logarithmic current density (I), in conjunction with surface coverage (θ). The rate constants can be assigned arbitrary numerical values (see supplementary data file), and the resulting simulation plots for a bath temperature of 800 ^{o}C (α = 0.5) are shown in Fig. 3. Notably, Eqs. (13) and (14) illustrate that different elementary steps with diverse surface coverages can yield the same Tafel slope, see Fig. 3 (a) and (b), respectively. Thus, these plots clearly illustrate the surface coverage dependence of Tafel slopes.

If step (i) is the RDS, the surface coverage of the vacant site (θ_0) remains constant at unity throughout, resulting in a consistent single Tafel slope of 0.21 V dec^{-1}, see Fig. 3 (a). For step (ii) as the RDS, the Tafel slope transition can be divided into the following three distinct phases, see Fig. 3 (b):

(a) Initially, in a lower overpotential region, the surface coverage of θ_1 is nearly zero. Consequently, both rate constant $(\overrightarrow{K_2^+})$ and surface coverage (θ_1) exhibit exponential dependence on the applied potential (see supplementary Eqs. S-9 and S-14, respectively). This dual dependency leads to a rapid rise in the reaction rate, resulting in a Tafel slope as low as 0.07 V dec^{-1}.

(b) As θ_1 increases about 0.4–0.6, constrained by overall reaction site limitations, the initially exponential rate growth of θ_1 diminishes, resulting in a slight rise in the Tafel slope, as shown in the dotted circle.

(c) Lastly, within a defined potential range, θ_1 reaches saturation, leaving only $\overrightarrow{K_2^+}$ with exponential dependence on applied potential (see supplementary Eq. S-9) and yielding a higher Tafel slope of 0.21 V dec^{-1}.

If either chemical step (iii) or (iv) determines the rate, the current and potential dependence arises indirectly from coverage, and the rate constant remains unaffected by the applied potential, see Eqs. (15) and (16) and supplementary Eqs. S-16 and S-24.

The Tafel slopes for charge transfer controlled steps obtained for the low temperature electrolyte at 800 ^{0}C are reported to be 0.07 and 0.21 V dec^{-1}. To assess the validity of this theoretical model-based rate expressions, Tafel slopes were also simulated (not shown) for a conventional cryolite bath temperature of 1000 ^{0}C, yielding widely accepted values of 0.07 and 0.25 V dec^{-1} for charge transfer controlled steps.[15,18]

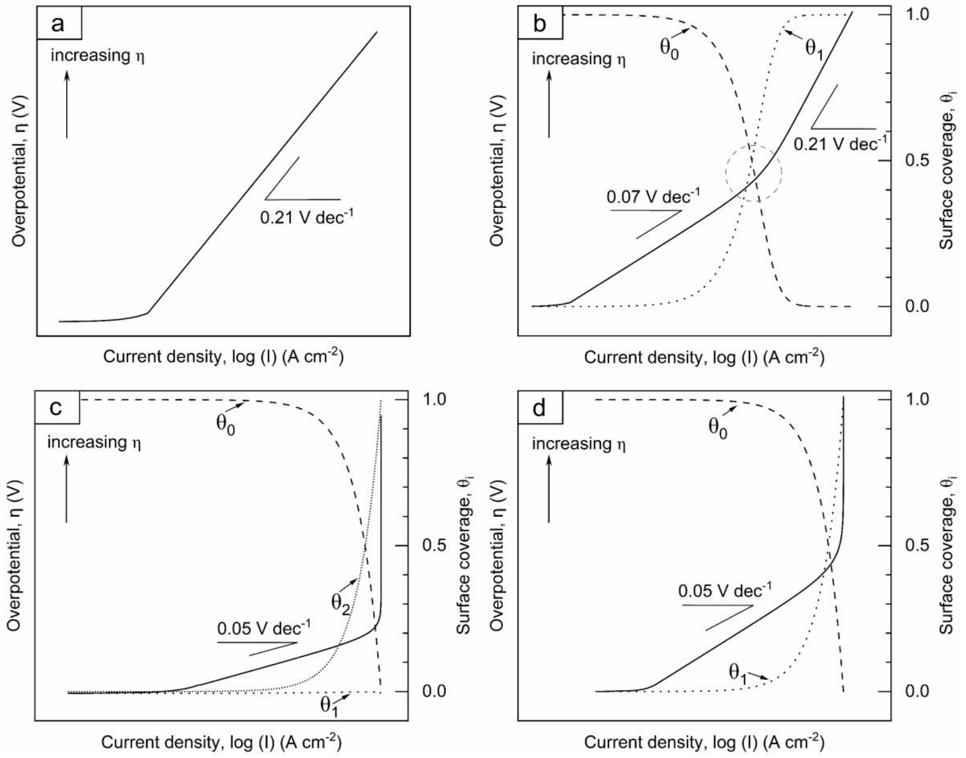

Fig. 3. Simulated Tafel plots for OER at a bath temperature of 800 ^{0}C, considering the RDS for (a) Eq. (13), (b) Eq.(14), (c) Eq.(15) and (d) Eq.(16).

OER kinetics on platinum anode

The observed two linear Tafel regions in Fig. 1 for OER on the platinum anode, represented by Eqs. (7) and (8), indicate a charge transfer controlled mechanism. Therefore, it appears to follow the proposed Mechanism-I, as illustrated in the simulation in Fig. 3. In the low overpotential region, the predicted slope is 0.07 V dec^{-1} at T= 800 ^{0}C assuming step (ii) as the rate determining, aligning precisely with experimental results. However, in higher overpotential region, a moderate deviation is observed with an experimental value of 0.26 V dec^{-1} compared to the theoretical prediction of 0.21 V dec^{-1}. This deviation may be attributed to changes in coverage or surface conditions. Interestingly, the RDS at higher overpotential region could be either step (i) or step (ii), as both yield the same theoretical Tafel slope.

In the literature study, various Tafel slopes are reported for the platinum anode in cryolite melts.[15,17,18] For cryolite at 1000 ^{0}C, the Tafel slopes of 0.08 and 0.25 V dec^{-1} were reported.[15,18] At 970 ^{0}C, a Tafel slope of 0.063–0.075 V dec^{-1} at lower overpotentials and 0.11–0.15 V dec^{-1} at higher overpotentials were reported.[17] Although these differences could be assigned to different cryolite ratios and temperatures in reported studies, notably the range of potential required to determine the Tafel slope was different. Lower Tafel slopes were reported at lower overpotentials, while higher values were observed in the higher region of overpotentials. This potential dependent behavior is evident and consistent with the simulated Tafel slopes, which are inherently influenced by both potential and surface coverage.

Apparently, the simulated Tafel slopes agree with previously proposed reaction mechanism steps of OER in cryolite melts[15], with differences in the RDS and the origin of the slope being discussed. According to these plots, for step (ii) as the RDS, a two-step Tafel slope was observed in Fig. 3 (b). A Tafel slope of 0.07 V dec^{-1} is achieved with a high coverage of the vacant site (θ_0), while a value of 0.21 V dec^{-1} is attained when the surface coverage (θ_1) of M-O$_{(ad)}$ becomes significant >0.6. This suggests that a slope of 0.21 V dec^{-1} is not attributable to step (i) as the RDS; rather, it must arise from either step (i) or step (ii) as the RDS with increased adsorbed oxygen coverage. Therefore, higher Tafel slopes, initially attributed to step (i)[15], can also arise form step (ii) as the RDS. In conclusion, current experimental evidence remains insufficient to definitively identify the RDS. While earlier OER mechanisms proposed a two-step charge transfer[15], our simulation results suggest that a single-step mechanism is also possible.

OER kinetics and the influence of surface treatment on Ni–Fe–Cu anode

The Tafel slopes observed in Fig. 2, for Ni–Fe–Cu anodes exhibit a single linear Tafel region and show diffusion limitation at higher overpotentials. Notably, the linear region at lower overpotentials was absent for the Ni–Fe–Cu anode compared to platinum, as seen in Fig. 1. Moreover, the obtained values were higher than both the lowest and highest values in the simulated theoretical Tafel slopes (0.07 and 0.21 V dec^{-1}) for charge transfer controlled RDS. For instance, the Tafel slope for oxidized and untreated anodes corresponds to a range of 0.17–0.30 V dec^{-1} and 0.27–0.39 V dec^{-1}, respectively, as shown in Table 1.

Additionally, it is evident that oxidized anodes have marked electrocatalytic activity with marginally lower Tafel slopes for OER as compared to untreated anodes. Most likely due to conductive $NiFe_2O_4$ oxide layer on oxidized anode as a result of surface treatment reported in a recent study.[12] Resultantly, at I_n= 0.8 A cm^{-2}, the oxidized anodes Ni42-Fe38-Cu20 and Ni48-Fe47-Cu5 exhibit lower overpotentials (0.31 and 0.37 V) after polarization compared to their untreated counterparts (0.46 and 0.43 V), respectively, as calculated using the Tafel equation and coefficients from Table 1. In contrast, the Ni-rich anode, Ni60-Fe30-Cu10, demonstrates significantly higher overpotentials, ranging from 0.56 V (oxidized) to 0.57 V (untreated). This could be attributed to the formation of a substantial non-conductive oxide layer. According to studies[10,30], Ni-rich alloys are not a good choice as inert anodes due to their susceptibility to fluoridation reactions. Finally, when comparing overpotentials at $\mathrm{I_n}$= 0.8 A cm^{-2}, the overpotential for the Ni–Fe–Cu anodes is 40–75% than that for the $CO_{2(g)}$ evolving carbon anodes used in the H-H process.[8]

In the literature study, various Tafel slopes are reported for candidate inert anode materials, both ceramic (SnO_2, $NiFe_2O_4$) and metal (Ni–Fe–Cu) anodes for OER in cryolite melts.[17,28,31,32] For example, SnO_2 showed a Tafel slope of 0.07 V dec^{-1} at 1000 ^{o}C in cryolite, $\mathrm{r} = \mathrm{NaF/AlF_3} = 2.7$ (mole ratios); SnO_2 doped with Mn/Fe/Ru exhibited two Tafel slopes of 0.04–0.07 V dec^{-1} at lower overpotentials, which increased to 0.09–0.13 V dec^{-1} at higher overpotentials.[31] Similarly, SnO_2 doped with Cu/Sb, in cryolite bath r = 2.1 at 970 ^{o}C, exhibited two Tafel slopes of 0.06 V dec^{-1} and 0.13 V dec^{-1}.[17] A 40Cu-30Ni-30Fe anode, in cryolite melt with r = 1.2 at 750 ^{o}C, showed a Tafel slope of 0.23 V dec^{-1}.[28] Meanwhile, a 20Cu-42Ni-38Fe alloy, in cryolite with CR = 1.3, KR = 0.3 at 825 ^{o}C, showed a Tafel slope of 0.51 V dec^{-1} for an untreated surface.[32] In certain cases, though not explicitly outlined, two Tafel slopes have also been observed.[18,33,34] As shown, the one- and two-step Tafel slopes have been frequently reported in the literature. These examples, as predicted by the theoretical model, highlight the importance of considering coverage dependent Tafel slope to identify the RDS.

The noticed variation in experimental Tafel slopes for Ni–Fe–Cu alloys in Fig. 2 from the theoretical model can be elucidated as follows. According to the plots in Fig. 3 (a, b), a high Tafel slope of 0.21 V dec^{-1} is observed when the reaction rate is governed by either the first discharge step (i) or a significantly high coverage of θ_1 in step (ii). Interestingly, in step (ii), a lower Tafel slope is also expected when the surface coverage (θ_1) by the adsorbate M-$O_{(ad)}$ is below a certain fraction. In other words, if the absorbate is formed in the initial phase of the OER remains predominant, this rationale of surface coverage could favor a lower Tafel slope and vice versa. In addition to this, at lower overpotentials, direct observation using see-through cell suggests that the surface coverage (θ) increases steadily, as observed by many authors.[35–37] However, at higher overpotentials, the electrode/melt interface presents an incredibly intricate hydrodynamic situation due to the gas evolving electrode, which can significantly influence the experimental Tafel slope.

In summary, the presence of a single linear Tafel region and the bending of the curve in Ni–Fe–Cu anodes raise uncertainty about whether these anodes adhere to a mechanism for OER similar to that of platinum. However, an extensive discussion of the OER mechanism on Ni–Fe–Cu anodes is a rather complex exercise and beyond the scope of this study. For a comprehensive understanding, long-term electrolysis of the anode is suggested to observe changes in surface oxide growth. The expectation is that surface oxide growth may influence the OER mechanism and, consequently, the overpotentials. Ideally, the formation of a compact and conductive oxide layer is essentially desired in IAT to yield a stable overpotential.

4.6 Conclusions

Steady state anodic polarization curves are obtained on platinum and a series of Ni–Fe–Cu-based anodes, respectively, in $\mathrm{KF - NaF - AlF_3 - Al_2O_{3(sat.)}}$ electrolyte at 800 ^{o}C.

Based on the proposed reaction mechanisms, a theoretical model of the oxygen evolution on a metallic anode for overpotential and current in conjunction with surface coverage is derived. The model successfully interprets the two linear Tafel regions, with one slope close to 0.07 V dec^{-1} in the low overpotential region and the other close to 0.21 V dec^{-1} in the higher potential region.

The polarization curve on the platinum anode exhibits two linear regions with Tafel slopes of 0.07 V dec^{-1} and 0.26 V dec^{-1} in the lower and higher overpotential regions, respectively, showing relatively good consistency with the theoretical model.

The polarization curve on Ni–Fe–Cu anodes, both in oxidized and untreated conditions, however, exhibits a single Tafel region. The slope of the single line was found to increase after electrolysis. Oxidized anodes exhibit better electrocatalytic activity compared to untreated anodes of same composition with lower Tafel slopes, primarily due to the pre-formed protective oxide layer. Consequently, at a normal current density of 0.8 A cm^{-2}, the oxidized anodes Ni42-Fe38-Cu20 and Ni48-Fe47-Cu5 showed lower overpotentials (0.31 and 0.37 V) after electrolysis compared to their corresponding untreated counterparts (0.46 and 0.43 V), respectively. Whereas, the Ni-rich anode, Ni60-Fe30-Cu10, exhibited significantly higher overpotentials, with values reaching 0.56 V (oxidized) to 0.57 V (untreated).

Contrary to existing literature[15] attributing the Tafel slope at higher overpotential to the first discharge step (i), our theoretical model indicates that this slope is also observed with step (ii), governing the rate with significant surface coverage of adsorbed oxygen. This observation strongly suggests the importance of identifying the rate determining step by analyzing the theoretical Tafel slope dependence on coverage.

Acknowledgements

This research has received support from the Icelandic Research Fund under project number 207242051, as well as support from the PROGRESS.NRW Germany - Innovation Fund under project ‘CO_2-free Al production’. The authors extend their gratitude to Jon Hjaltalin Magnusson of Arctus Aluminium Limited in Iceland for providing some of the alloy materials.

References

[1] G. Saevarsdottir, H. Kvande, B.J. Welch, Aluminum Production in the Times of Climate Change: The Global Challenge to Reduce the Carbon Footprint and Prevent Carbon Leakage, JOM. 72 (2020) 1422–1422.
[2] D.R. Sadoway, Inert anodes for the Hall-Héroult cell: The ultimate materials challenge, JOM. 53 (2001) 34–35.
[3] K. Hund, D. La Porta, T.P. Fabregas, T. Laing, J. Drexhage, Minerals for Climate Action: The Mineral Intensity of the Clean Energy Transition, (2023).

[4] J. Thonstad, P. Fellner, G.M. Haarberg, J. Hives, H. Kvande, A. Sterten, Aluminium Electrolysis: Fundamentals of the Hall-Héroult Process, Beuth Verlag GmbH, 2011.

[5] Primary Aluminium Production - International Aluminium Institute, (2021). https://international-aluminium.org/statistics/primary-aluminium-production/ (accessed November 26, 2023).

[6] I. Galasiu, R. Galasiu, J. Thonstad, Inert Anodes for Aluminium Electrolysis, Beuth Verlag GmbH, 2011.

[7] A. Roine, HSC Chemistry Software, Version 9.9.2.3, Metso Outotec, Pori, Finland, (2017). www.mogroup.com/hsc.

[8] H. Gudbrandsen, N. Richards, S. Rolseth, J. Thonstad, Field Study of the Anodic Overvoltage in Prebaked Anode Cells, in: Essential Readings in Light Metals, John Wiley & Sons, Ltd, 2013: pp. 166–171.

[9] T.R. Beck, A Non-Consumable Metal Anode for Production of Aluminum with Low-Temperature Fluoride Melts, Essential Readings in Light Metals: Volume 4 Electrode Technology for Aluminum Production. 4 (2016) 1104–1109.

[10] V. Chapman, B.J. Welch, M. Skyllas-Kazacos, Anodic behaviour of oxidised Ni–Fe alloys in cryolite–alumina melts, Electrochimica Acta. 56 (2011) 1227–1238.

[11] G. Gunnarsson, G. Óskarsdóttir, S. Frostason, J.H. Magnússon, Aluminum Electrolysis with Multiple Vertical Non-consumable Electrodes in a Low Temperature Electrolyte, Light Metals 2019. (2019) 803–810.

[12] K. Singh, G. Gunnarsson, J.H. Magnusson, G.M. Haarberg, G. Saevarsdottir, Performance Evaluation of Low-Temperature KF-NaF-AlF3 Electrolytes for Aluminum Electrolysis Using Vertical Inert Cu–Ni–Fe Alloy Anodes, Journal of The Electrochemical Society. 170 (2023) 113507.

[13] H. Flood, T. Førland, Some investigations on the oxygen—overpotential in molten salts, Discuss. Faraday Soc. 1 (1947) 302.

[14] K.J. Vetter, Electrochemical Kinetics: Theoretical Aspects, Elsevier, 2013.

[15] J. Thonstad, Anodic overvoltage on platinum in cryolite-alumina melts, Electrochimica Acta. 13 (1968) 449–456.

[16] G.J. Janz, F. Saegusa, Anodic Polarization Curves in Molten Carbonate Electrolysis, J. Electrochem. Soc. 108 (1961) 663.

[17] P.G. Russell, Oxygen Evolution at Platinum and Ceramic Oxide Anodes in Cryolite-Alumina Melts, Proc. Vol. 1984–2 (1984) 430.

[18] A.D. McLeod, J.S. Haggerty, D.R. Sadoway, Inert anode materials for Hall cells, Light Metals 1986. 2 (1986) 269–273.

[19] A.E. Bolzán, A.J. Arvia, Changes in the kinetics of the oxygen evolution reaction induced by oxide films at platinum electrodes, Journal of Electroanalytical Chemistry. 375 (1994) 157–162.

[20] J.-M. Hu, J.-Q. Zhang, C.-N. Cao, Oxygen evolution reaction on IrO2-based DSA® type electrodes: kinetics analysis of Tafel lines and EIS, International Journal of Hydrogen Energy. 29 (2004) 791–797.

[21] T. Shinagawa, A.T. Garcia-Esparza, K. Takanabe, Insight on Tafel slopes from a microkinetic analysis of aqueous electrocatalysis for energy conversion, Sci Rep. 5 (2015) 13801.

[22] Z.W. Seh, J. Kibsgaard, C.F. Dickens, I. Chorkendorff, J.K. Nørskov, T.F. Jaramillo, Combining theory and experiment in electrocatalysis: Insights into materials design, Science. 355 (2017) eaad4998.

[23] I. Gallino, Phase diagram, thermal stability, and high temperature oxidation of the ternary Cu-Ni-Fe system, PhD thesis, Oregon State University, 2004.

[24] I. Gallino, M.E. Kassner, R. Busch, Oxidation and corrosion of highly alloyed Cu–Fe–Ni as inert anode material for aluminum electrowinning in as-cast and homogenized conditions, Corrosion Science. 63 (2012) 293–303.

[25] A. Apisarov, A. Dedyukhin, O. Tkacheva, E. Nikolaeva, Y. Zaikov, P. Tinghaev, Physical-chemical properties of the KF-NAF-ALF3 molten system with low cryolite ratio, TMS Annual Meeting. (2009) 401–403.

[26] A. Apisarov, A. Dedyukhin, E. Nikolaeva, P. Tinghaev, O. Tkacheva, Y. Zaikov, Liquidus Temperatures of Cryolite Melts With Low Cryolite Ratio, Metallurgical and Materials Transactions B. 42 (2010) 236–242.

[27] A. Dedyukhin, A. Kataev, Density and molar volume of KF-NaF-AlF3 Melts with Al2O3 and CaF2 additions, ECS Transactions. 64 (2014).

[28] J. Thonstad, A. Kisza, J. Hives, Anode overvoltage on metallic inert anodes in low-melting bath, Light Metals. 2006 (2006) 373–377.

[29] A.J. Bard, L.R. Faulkner, H.S. White, Electrochemical Methods: Fundamentals and Applications, 3rd Edition, John Wiley & Sons, 2022.

[30] D.A. Simakov, E.V. Antipov, M.I. Borzenko, S.Y. Vassiliev, Y.A. Velikodny, V.M. Denisov, V.V. Ivanov, S.M. Kazakov, Z.V. Kuzminova, A.Y. Filatov, Nickel and nickel alloys electrochemistry in cryolite-alumina melts, TMS, Warrendale, USA. 2007 (2007) 489–493.

[31] Y.X. Liu, J. Thonstad, Oxygen overvoltage on SnO2-based anodes in NaF-AlF3-Al2O3 melts. Electrocatalytic effects of doping agents, Electrochimica Acta. 28 (1983) 113–116.

[32] G. Saevarsdottir, G.M. Haarberg, M. Bourmaud, K. Singh, S.K. Padamata, Anodic Behaviour of Ni42Fe38Cu20 Electrode in Molten Fluoride Salts, J. Electrochem. Soc. 170 (2023) 072508.

[33] A.-M. Popescu, Oxygen-evolving SnO2-based ceramic anodes in aluminium electrolysis, Chem. Res. Chin. Univ. 30 (2014) 800–805.

[34] J. Du, B. Wang, Y. Liu, G. Yao, Z. Fang, P. Hu, Study on the Bubble Behavior and Anodic Overvoltage of NiFe2O4 Ceramic Based Inert Anodes, in: M. Hyland (Ed.), Light Metals 2015, Springer International Publishing, Cham, 2016: pp. 1193–1197.

[35] H. Vogt, The actual current density of gas-evolving electrodes—Notes on the bubble coverage, Electrochimica Acta. 78 (2012) 183–187.

[36] B. Chmielowiec, T. Fujimura, T. Otani, K. Aoyama, T. Nohira, T. Homma, Y. Fukunaka, A. Allanore, Experimental Measurement of Overpotential Sources during Anodic Gas Evolution in Aqueous and Molten Salt Systems, J. Electrochem. Soc. 166 (2019) E323.

[37] N. Stanic, I. Jevremovic, A.M. Martinez, E. Sandnes, Bubble Evolution on Different Carbon Anode Designs in Cryolite Melt, Metall Mater Trans B. 51 (2020) 1243–1253.

Supplementary Material For:

Chapter 4

Overpotential on Oxygen Evolving Platinum and Ni–Fe–Cu Anode for Low Temperature Molten Fluoride Electrolytes

Kamaljeet Singh[1,2,*], Geir Martin Haarberg[2], Abdul Rahman Mallah[1], Gudmundur Gunnarsson[3], Thomas Luke Jamieson[4], Isabella Gallino[4,5], Gudrun Saevarsdottir[1,2]

[1]Department of Engineering, Reykjavik University, 102 Reykjavik, Iceland
[2]Department of Materials Science and Engineering, NTNU, 7491 Trondheim, Norway
[3]Taeknisetur IceTec, Arleynir 8, 112 Reykjavik, Iceland
[4]Chair of Metallic Materials, Saarland University, 66123 Saarbrucken, Germany
[5]Department of Materials Science and Engineering, TU-Berlin, 10587 Berlin, Germany
*Corresponding author: kamaljeets@ru.is

S4.1 Theoretical treatment of OER

Based upon the literature, the mechanism of oxygen evolution reaction (OER) in molten salts on a metal anode can be divided into four elementary steps as follows [1–5].

(i) $\mathrm{M} + \mathrm{O}^{2-} \rightleftharpoons \mathrm{M}-\mathrm{O}_{(\mathrm{ad})} + 2\mathrm{e}^-$ (S-1)
(ii) $\mathrm{M}-\mathrm{O}_{(\mathrm{ad})} + \mathrm{O}^{2-} \rightleftharpoons \mathrm{M}-\mathrm{O}_{2(\mathrm{ad})} + 2\mathrm{e}^-$ (S-2)
(iii) $\mathrm{M}-\mathrm{O}_{2(\mathrm{ad})} \rightleftharpoons \mathrm{M} + \mathrm{O}_{2(\mathrm{g})}$ (S-3)
(iv) $2(\mathrm{M}-\mathrm{O}_{(\mathrm{ad})}) \rightleftharpoons 2\mathrm{M} + \mathrm{O}_{2(\mathrm{g})}$ (S-4)

Theoretical kinetics for each step are discussed, examining the possibility of each step being the rate-determining one, resulting in the derivation of three different current expressions. Regarding the surface coverage, θ_0, θ_1 and θ_2 denote the coverage of vacant site M, $\mathrm{M}-\mathrm{O}_{(\mathrm{ad})}$ and $\mathrm{M}-\mathrm{O}_{2(\mathrm{ad})}$, respectively.

Case (i)

When Eq. (S-1) determines the overall rate of reaction, the rate expressions can be written as:

$$r_1^+ = \overrightarrow{K_1^+}\,\theta_0\, a_{O^{2-}} = k_1^+\,\theta_0\, a_{O^{2-}} \exp\{2(1-\alpha_1)f\eta_1\} \qquad \text{(S-5)}$$

$$r_1^- = \overleftarrow{K_1^-}\,\theta_1 = k_1^-\,\theta_1 \exp(-2\alpha_1 f\eta_1) \qquad \text{(S-6)}$$

where r_i, $\overline{K_i}$ and k_i are reaction rate, rate constant and standard rate constant, respectively. α_i is the symmetry coefficient, $f = F/RT$ (where F, R, and T take their usual meanings), and η_i defines the overpotential (difference between anode potential and reversible potential, $\eta = E_{anode} - E^{rev}$), for i^{th} equation.

The current is correlated to the reaction rate by the following expression:

$$i = nFAr \qquad \text{(S-7)}$$

where i is the current, n is the number of total electron transfers and A denotes the area of electrode. Assuming the coverage of the empty site (θ_0) is close to unity ≈1 when the forward rate constant $\overrightarrow{K_1^+}$ is very small ≈0 for the rate determining step (RDS). Eqs. (S-5) and (S-7) lead to the following expression for the forward current of the rate determining Eq. (S-1):

$$i = nFA\, k_1^+\, a_{O^{2-}} \exp\{2(1-\alpha_1)f\eta_1\} \qquad \text{(S-8)}$$

Case (ii)

Eq. (S-2) is the RDS. The forward and backward rates of Eq. (S-2) can be written as:

$$r_2^+ = \overrightarrow{K_2^+}\,\theta_1\, a_{O^{2-}} = k_2^+\,\theta_1\, a_{O^{2-}} \exp\{2(1-\alpha_2)f\eta_2\} \qquad \text{(S-9)}$$

$$r_2^- = \overleftarrow{K_2^-}\,\theta_2 = k_2^-\,\theta_2 \exp(-2\alpha_2 f\eta_2) \qquad \text{(S-10)}$$

The reaction rate must be expressed in terms of activity of the reactants, and thus the forward and reverse reactions of Eq. (S-1) are pre-equilibrated.

$$r_1^+ = r_1^- \qquad \text{(S-11)}$$

The surface coverage is expressed as:

$$\theta_0 + \theta_1 = 1 \qquad \text{(S-12)}$$

Combining Eqs. (S-11) and (S-12) leads to the following surface coverage expression:

$$\theta_0 = \frac{\theta_1}{K_1\, a_{O^{2-}} \exp(2f\eta_1)} \qquad \text{(S-13)}$$

$$\theta_1 = \frac{K_1\, a_{O^{2-}} \exp(2f\eta_1)}{1 + K_1\, a_{O^{2-}} \exp(2f\eta_1)} \qquad \text{(S-14)}$$

where $K_i = \frac{k_i^+}{k_i^-}$ is the ratio of rate constant for i^{th} equation.

Finally, using Eqs. (S-7), (S-9), (S-13) and (S-14), the current expression for the forward reaction of Eq. (S-2) can be written as:

$$i = nFA\frac{K_1\, k_2^+\, a_{O^{2-}}^2 \exp(2f\eta_1)\exp\{2(1-\alpha_2)f\eta_2\}}{1 + K_1\, a_{O^{2-}} \exp(2f\eta_1)} \qquad \text{(S-15)}$$

Case (iii)

When Eq. (S-3) determines the rate of the reaction, the reaction rates can be written as:

$$r_3^+ = \overrightarrow{K_3^+}\,\theta_2 \qquad \text{(S-16)}$$

$$r_3^- = \overleftarrow{K_3^-}\,\theta_0 P_{O_2} \qquad \text{(S-17)}$$

The surface coverage can be defined as:

$$\theta_0 + \theta_1 + \theta_2 = 1 \qquad \text{(S-18)}$$

Now, the reaction rate of Eqs. (S-1) and (S-2) are pre-equilibrated, which correspond to Eqs. (S-11) and (S-19), respectively.

$$r_2^+ = r_2^- \qquad \text{(S-19)}$$

Combining Eqs. (S-5), (S-6), (S-9), (S-10), (S-11), (S-18) and (S-19) leads to the following expression for the surface coverage:

$$\theta_0 = \frac{1}{1 + K_1 a_{O^{2-}} \exp(2f\eta_1) + K_1\, K_2 a_{O^{2-}}^2 \exp\{2f(\eta_1+\eta_2)\}} \qquad \text{(S-20)}$$

$$\theta_1 = K_1\, \theta_0\, a_{O^{2-}} \exp(2f\eta_1) \qquad \text{(S-21)}$$

$$\theta_2 = \frac{K_1\, K_2\, a_{O^{2-}}^2 \exp\{2f(\eta_1+\eta_2)\}}{1 + K_1 a_{O^{2-}} \exp(2f\eta_1) + K_1\, K_2\, a_{O^{2-}}^2 \exp(2f\eta_1)\exp(2f\eta_2)} \qquad \text{(S-22)}$$

Finally, using Eqs. (S-7), (S-16) and (S-22), the current expression for the forward reaction of Eq. (S-3) can be written as:

$$i = nFA\overrightarrow{K_3^+}\ \frac{K_1\, K_2\, a_{O^{2-}}^2 \exp\{2f(\eta_1+\eta_2)\}}{1 + K_1 a_{O^{2-}} \exp(2f\eta_1) + K_1\, K_2\, a_{O^{2-}}^2 \exp\{2f(\eta_1+\eta_2)\}} \qquad \text{(S-23)}$$

Case (iv)

When Eq. (S-4) is the rate determining step, the reaction rate will be:

$$r_4^+ = \overrightarrow{K_4^+}\ \theta_1^2 \qquad \text{(S-24)}$$

$$r_4^- = \overleftarrow{K_4^-}\ \theta_1^2\, P_{O_2} \qquad \text{(S-25)}$$

The reactant for this step is provided by Eq. (S-1), so Eq. (S-1) can be pre-equilibrated according to Eq. (S-11), which means that Eqs. (S-13) and (S-14) are valid here.

Therefore, the current expression for the forward reaction of Eq. (S-4) can be written as:

$$\mathrm{i} = \mathrm{nFA}\,\overrightarrow{\mathrm{K}_4^{+}}\left\{\frac{\mathrm{K}_1\,\mathrm{a}_{\mathrm{O}^{2-}}\exp(2\mathrm{f}\eta_1)}{1+\mathrm{K}_1\,\mathrm{a}_{\mathrm{O}^{2-}}\exp(2\mathrm{f}\eta_1)}\right\}^2 \qquad \text{(S-26)}$$

Note that Eqs. (S-3) and (S-4) are not e^{-} transfer reactions, however, the potential dependence of the current originates from the surface coverage (θ) relationship.

Based on Eqs. (S-8), (S-15), (S-23) and (S-26), Tafel plot simulations can be attempted for overpotential (η) versus the semi-logarithmic of current density, $\log(\mathrm{I})$, in conjunction with surface coverage (θ). The rate constants can be assigned arbitrary numerical values. The values used are $\mathrm{k}_1' / \mathrm{k}_2' / \mathrm{k}_3' / \mathrm{k}_4' / \mathrm{k}_5' = 10^{-4} / 10^{-4} / 1 / 10^{-5} / 10^{-5}$, $\mathrm{a}_{\mathrm{O}^{2-}} = 1$, T = 800 ^{o}C and α = 0.5, and the resulting simulation plots are shown in Fig. 3.

All simulation plots utilized the MATLAB analysis toolbox. The corresponding codes and source files will be provided upon request.

References

[1] J. Thonstad, Anodic overvoltage on platinum in cryolite-alumina melts, Electrochimica Acta. 13 (1968) 449–456.
[2] K.J. Vetter, Electrochemical Kinetics: Theoretical Aspects, Elsevier, 2013.
[3] G.J. Janz, F. Saegusa, Anodic Polarization Curves in Molten Carbonate Electrolysis, J. Electrochem. Soc. 108 (1961) 663.
[4] J. Thonstad, P. Fellner, G.M. Haarberg, J. Hives, H. Kvande, A. Sterten, Aluminium Electrolysis: Fundamentals of the Hall-Héroult Process, Beuth Verlag GmbH, 2011.
[5] A.J. Bard, L.R. Faulkner, H.S. White, Electrochemical Methods: Fundamentals and Applications, 3rd Edition, John Wiley & Sons, 2022.

Chapter 5

Ni–Fe-based Alloy as Oxygen Evolving Anode for Sustainable Aluminum Production

Kamaljeet Singh[1,2,*], Thomas Luke Jamieson[3,4], Gudmundur Gunnarsson[5], Geir Martin Haarberg[2], Isabella Gallino[3,4], Ralf Busch[4], Jon Hjaltalin Magnusson[6], Gudrun Saevarsdottir[1,2]

[1]Department of Engineering, Reykjavik University, 102 Reykjavik, Iceland
[2]Department of Materials Science and Engineering, NTNU, 7491 Trondheim, Norway
[3]Chair of Metallic Materials, Technical University of Berlin, Berlin 10587, Germany
[4]Chair of Metallic Materials, Saarland University, Campus, Saarbrücken 66123, Germany
[5]Taeknisetur IceTec, Arleynir 8, 112 Reykjavik, Iceland
[6]Arctus Aluminium Limited, Arleynir 8, 112 Reykjavik, Iceland
*Corresponding author: kamaljeets@ru.is

This page is intentionally left blank.

Chapter 6

Conclusions

In the present study, a detailed investigation of the various Ni–Fe–Cu-based alloys for oxygen evolving anode (OEA) in a range of low temperature KF-NaF-AlF_3-$Al_2O_{3(sat.)}$-based electrolytes for aluminum electrolysis at 800 ^oC was conducted. In Chapter 1, three main goals of the thesis were outlined as:

i. To evaluate the optimal compositions of electrolytes and anode alloys.
ii. To study the anodic overpotential to assess energy efficiency.
iii. To understand the influence of Ni/Fe ratio on oxide growth mechanisms in alloys.

The key experimental findings are summarized from Chapters 3 to 5 with respect to these goals.

6.1 Performance evaluation of low temperature electrolyte

- Two electrolyte compositions, K-rich (CR = 1.3, KR = 0.8) and Na-rich (CR = 1.3, KR = 0.3), investigated with Ni–Fe–Cu-based OEA with a view to identify optimal compositions and conditions for aluminum electrolysis in a 40 A laboratory cell.
- The best electrolysis performance was obtained for the K-rich electrolyte combined with $Ni_{42}Fe_{38}Cu_{20}$ alloy, yielding stable cell voltage (3.49 ± 0.02 V) under constant current electrolysis conditions and a low alloy wear rate (3 $mmyear^{-1}$). This performance was attributed to the better alumina solubility of the K-rich electrolyte and development of a compact and adherent scale (~23 µm) with protective $NiFe_2O_4$ layer on $Ni_{42}Fe_{38}$ Cu_{20} anode.
- In contrast, Na-rich electrolyte composition exhibited higher alloy wear rates under similar electrolysis conditions i.e., of $Ni_{42}Fe_{38}Cu_{20}$ (7 $mmyear^{-1}$) and $Ni_{48}Fe_{47}Cu_5$ (9 $mmyear^{-1}$). It was found that an electrolyte composition with low alumina solubility, such as Na-rich, could potentially be more corrosive for metallic anodes, mainly due to non-saturated local alumina conditions in such baths.
- Prior to electrolysis, Ni–Fe–Cu anodes were subjected to air oxidation treatment at 800 ^oC, to develop a protective oxide scale on the surface. It was found that $Ni_{42}Fe_{38}Cu_{20}$ alloy developed a multi-layered scale of Cu- and Fe-rich oxide phases. Conversely, $Ni_{48}Fe_{47}Cu_5$ alloy produced mainly Fe-rich oxide phases. The Cu content of the alloy appeared to have a substantial impact on oxide scale morphology. The alloy with a higher Cu content displayed the formation of a dense, defect-free, multi-layered oxide scale. An interesting fresh insight from this study is the absence of the repetitive multi-layered oxide growth pattern commonly reported in the literature for oxidation studies of Ni–Fe–Cu alloys. It was shown that a protective $NiFe_2O_4$ oxide

developed on Ni–Fe–Cu alloys, irrespective of alloy composition, confirming the effectiveness of this oxidation treatment in meeting the requirements for an inert anode.

- Additionally, the stability of the aluminum electrolysis process in the 40 A cell, fitted with two vertical Ni–Fe–Cu anodes and a TiB_2 cathode at the center, was assessed by applying rapid changes in current density and bath temperature within set limits. The electrolysis cell responded steadily to these rapid changes, suggesting its potential compatibility with grid load balancing in smart grid technology.

6.2 Overpotential on oxygen evolving Pt and Ni–Fe–Cu anodes

- In this work, the anodic overpotential was evaluated using steady-state polarization on pure platinum and three compositions of Ni–Fe–Cu alloys. The electrolyte composition used was $KF\text{-}NaF\text{-}AlF_3$ with a CR of 1.3 and a KR of 0.3 at 800 ^{o}C.
- Based on the proposed reaction mechanisms, a theoretical model of oxygen evolution on a metallic anode for overpotential and current in conjunction with surface coverage is derived. The model successfully interprets the two linear Tafel regions, with one slope close to 0.07 $Vdec^{-1}$ in the low overpotential region and the other close to 0.21 $Vdec^{-1}$ in the higher potential region. Similarly, the polarization curve on the platinum anode exhibits two linear regions with Tafel slopes of 0.07 $Vdec^{-1}$ and 0.26 $Vdec^{-1}$ in the lower and higher overpotential regions, respectively, showing relatively good consistency with the theoretical model.
- However, the proposed theoretical model could not explain the single linear Tafel region, and the bending of polarization curve observed on Ni–Fe–Cu anodes, highlighting the complexity of the oxygen evolution reaction mechanism.
- The polarization curve on Ni–Fe–Cu anodes showed that oxidized alloys exhibit better electrocatalytic activity compared to untreated anodes of same composition with lower Tafel slopes, primarily due to the conductive oxide formation. For instance, at a normal current density of 0.8 Acm^{-2}, the oxidized anodes $Ni_{42}Fe_{38}Cu_{20}$ and $Ni_{48}Fe_{47}Cu_5$ showed lower overpotentials (0.31 and 0.37 V) after electrolysis compared to their corresponding untreated compositions (0.46 and 0.43 V), respectively.
- Notably, the observed overpotential values (0.31 to 0.43) at normal current density of 0.8 Acm^{-2} with Ni–Fe–Cu anodes are about 40% to 57% less than that for $CO_{2(g)}$ evolving carbon anode (typically ~0.76 V at 0.8 Acm^{-2}). This reduction in overpotential could partly offset the increased energy demand resulting from the higher reaction voltage of an $O_{2(g)}$ evolving anode compared to the conventional Hall-Héroult process.
- The simulation of theoretical model illustrates that Tafel slopes can change due to their dependence on potential driven surface coverage of adsorbate. Contrary to existing literature attributing the Tafel slope at higher overpotential to the first discharge step, our theoretical model indicates that this slope is also observed with the second discharge step, governing the rate with significant surface coverage of adsorbed oxygen. This observation strongly suggests the importance of identifying the rate determining step by analyzing the theoretical Tafel slope dependence on the coverage of adsorbate.

6.3 Influence of Ni/Fe ratio on oxide growth mechanism

- A series of $Ni_{90-x}Fe_xCu_{10}$ alloys, with x (in wt.%) ranging from 10 to 60 in increments of 10, or a Ni/Fe ratio (wt.%) varying from 8 to 0.5, were evaluated for aluminum production to determine the optimal Ni/Fe ratio. The electrolyte composition used was KF-NaF-AlF_3 with a CR of 1.3 and a KR of 0.64 at a bath temperature of 800 ^oC.
- The thermodynamic analysis of the Ni–Fe–Cu system was conducted by evaluating the dissociation potential of their oxides as a function of alumina activity. It was found that Cu-based anodes exhibit the highest dissociation potential, followed by Fe- and Ni-based anodes. Notably, the analysis revealed that Ni-based anodes have a greater tendency to form insulating $NiAl_2O_4$ under saturated alumina bath conditions.
- The oxidation rate of $Ni_{90-x}Fe_xCu_{10}$ alloys series at 800 ^oC in pure oxygen was found to be reasonably slow, following a parabolic trend except for $Ni_{30}Fe_{60}Cu_{10}$ alloy. Notably, the oxidation kinetics of $Ni_{30}Fe_{60}Cu_{10}$ alloy transitioned from a parabolic to a slower cubic regime. This behavior was attributed to the formation of well adherent and sufficiently thick oxide scale composed of mainly Fe_2O_3 and $NiFe_2O_4$ oxides, which significantly inhibits the inward diffusion of oxygen. A decrease in the level of scale adhesion and an increase in porosity defects were observed for alloys with an increasing Ni/Fe ratio. This change was accompanied by a reduction in the fraction of the $NiFe_2O_4$ layer within the scale and a corresponding increase in the NiO layer fraction.
- During the 24 h electrolysis performance test, Ni/Fe ratio of $Ni_{90-x}Fe_xCu_{10}$ alloys proves to be a critical factor influencing stability and performance of the anode. A decrease in the Ni/Fe ratio from 8 to 0.5 shows a positive impact. Alloys with a Ni/Fe ratio between 8 and 1.25 are deemed unsuitable for OEA applications due to their high wear rate up to 16 $mmyear^{-1}$. In contrast, an optimal Ni/Fe ratio between 0.8 and 0.5 demonstrates the ability to form protective and conductive oxide scale with an anode wear rate of less than 5 $mmyear^{-1}$ and metal purity reaching up to 99.9 wt.%. The Faradaic current efficiency during these tests was found to increase with anode stability, ranging from 71% to 90%.
- The development of oxide scale on anode during electrolysis revealed a complex oxide growth mechanism. For alloys with a Ni/Fe ratio from 8 to 1.25, it was found that having a continuous NiO layer could result in poor performance of anode due to two reasons. First, the excessive oxidation of NiO during electrolysis increases scale thickness with poor adhesion to the alloy. Second, there is a tendency for it to convert to insulating $NiAl_2O_4$ under saturated alumina bath conditions, as revealed by thermodynamic analysis. Consequently, these conditions increase the scale resistance, raising the anode potential beyond the oxide dissociation potential limit. This, in turn, accelerates alloy corrosion through the formation of NiF_2. Whereas for a Ni/Fe ratio from 0.8 to 0.5, alloys form a kinetically slow-growing, and self-regenerating scale of dual-layered structure. This structure consists of an outer $NiFe_2O_4$ layer at the oxide/electrolyte interface and an inner, non-stoichiometric $Ni_xFe_{3-x}O_4$ layer rich in Fe at the oxide/alloy interface, which enhances the performance of the anode.

This page is intentionally left blank.

Chapter 7

Future work

Future research could take two directions, the first being to validate the small-scale laboratory experiments carried out in this study. The best reported compositions, both the anode alloy and the low temperature electrolyte, must be verified in a pilot cell (1 to 10 kA) for a longer duration.

The second direction involves expanding on this thesis by exploring the following areas:

- Optimization of anode composition: This includes further optimizing the Ni-Fe-Cu ratio and adding other alloying elements that can enhance the stability of the oxide scale and form conductive oxides. We showed that the depletion region beneath the oxide scale in the anodes is inherently inhomogeneous and accumulates bath components, largely fluoride, over the electrolysis duration. This suggests that methods to re-homogenize the depletion region after pre-oxidation treatment are necessary. Potential strategies include post-oxidation heat treatments to restore uniformity in the depletion region and improve anode alloy stability. Another approach involves applying Ni-Fe-O coatings to form a protective oxide layer on the surface while preserving a homogeneous composition beneath.
- Alloy design for target oxides scales: It is essential to gain a deeper understanding of the complex transport processes occurring at both the alloy/oxide interface and the oxide/electrolyte interface during electrolysis. This is particularly important to understand the diffusion of cations and anions (F^- and O^{2-}) at these interfaces. Computational methods, such as Density Function Theory, could be used to study the transport properties of complex oxide phases. Designing alloys to form target oxide phases with high ion diffusion barriers would be particularly beneficial.
- Overpotential study: The mechanism of oxygen evolution on metallic anodes in fluoride melt is complex. The present study on overpotential was performed in an unstirred melt which includes some bubble resistance. Therefore, it would be interesting to conduct these studies in a stirred melt and propose a revised reaction mechanism scheme based on the findings.
- Producing direct aluminum alloys: Ni–Fe–Cu-based anodes tested in this study exhibited a finite wear rate, ranging from 2 to 16 mmyear^{-1}. Therefore, instead of classifying them as ‘inert anodes,’ they are more accurately described as ‘slow-consuming anodes.’ Some interesting compositions exhibited stable cell voltage, low corrosion rates, and high-purity aluminum production. However, a few anode compositions produced metal with high impurities (Fe > 0.1 wt.%), falling short of primary aluminum standards. This limitation presents an opportunity: such anodes could be used to directly produce aluminum alloys during electrolysis, where higher impurity levels are acceptable, thereby eliminating the need for downstream alloying in the cast house.

NTNU:
ISBN 978-82-326-9084-8 (printed ver.)
ISBN 978-82-326-9083-1 (electronic ver.)
ISSN 1503-8181 (printed ver.)
ISSN 2703-8084 (online ver.)

Reykjavik University:
ISBN 978-9935-539-70-0 (printed ver.)
ISBN 978-9935-539-71-7 (electronic ver.)

NTNU
Norwegian University of
Science and Technology